

1 LEVERAGING MULTI-MESSENGER ASTROPHYSICS FOR DARK MATTER SEARCHES

By

Daniel Nicholas Salazar-Gallegos

A DISSERTATION

Submitted to  
Michigan State University  
in partial fulfillment of the requirements  
for the degree of

Physics—Doctor of Philosophy  
Computational Mathematics in Science and Engineering—Dual Major

Today

**ABSTRACT**

3 I did Dark Matter with HAWC and IceCube. I also used Graph Neural Networks

<sup>4</sup> Copyright by

<sup>5</sup> DANIEL NICHOLAS SALAZAR-GALLEGOS

<sup>6</sup> Today

## ACKNOWLEDGMENTS

8 I love my friends. Thanks to everyone that helped me figure this out. Amazing thanks to the people  
9 at LANL who supported me. Eames, etc Dinner Parties Jenny and her child Kaydince Kirsten, Pat,  
10 Andrea Family. You're so far but so critical to my formation. Unconditional love. Roommate

## TABLE OF CONTENTS

12	LIST OF TABLES . . . . .	vii
13	LIST OF FIGURES . . . . .	viii
14	LIST OF ABBREVIATIONS . . . . .	xvi
15	CHAPTER 1 INTRODUCTION . . . . .	1
16	CHAPTER 2 DARK MATTER IN THE COSMOS . . . . .	2
17	2.1 Introduction . . . . .	2
18	2.2 Dark Matter Basics . . . . .	3
19	2.3 Evidence for Dark Matter . . . . .	4
20	2.4 Searching for Dark Matter: Particle DM . . . . .	11
21	2.5 Sources for Indirect Dark Matter Searches . . . . .	16
22	2.6 Multi-Messenger Dark Matter . . . . .	18
23	CHAPTER 3 HIGH ALTITUDE WATER CHERENKOV (HAWC) OBSERVATORY . . . . .	21
24	3.1 The Detector . . . . .	21
25	3.2 Events Reconstruction and Data Acquisition . . . . .	21
26	3.3 Remote Monitoring . . . . .	21
27	CHAPTER 4 ICECUBE NEUTRINO OBSERVATORY . . . . .	22
28	4.1 The Detector . . . . .	22
29	4.2 Events Reconstruction and Data Acquisition . . . . .	22
30	4.3 Northern Test Site . . . . .	22
31	CHAPTER 5 GLORY DUCK: MULTI-WAVELENGTH SEARCH FOR DARK MATTER ANNIHILATION TOWARDS DWARF SPHEROIDAL GALAXIES . . . . .	23
32	5.1 Introduction . . . . .	23
33	5.2 Dataset and Background . . . . .	25
34	5.3 Analysis . . . . .	26
35	5.4 Likelihood Methods . . . . .	31
36	5.5 HAWC Results . . . . .	37
37	5.6 Glory Duck Combined Results . . . . .	40
38	5.7 HAWC Systematics . . . . .	45
39	5.8 $J$ -factor distributions . . . . .	46
40	5.9 Discussion and Conclusions . . . . .	52
43	CHAPTER 6 MULTITHREADING HAWC ANALYSES FOR DARK MATTER SEARCHES . . . . .	56
44	6.1 Introduction . . . . .	56
45	6.2 Dataset and Background . . . . .	56
46	6.3 Analysis . . . . .	58

48	6.4	Likelihood Methods . . . . .	61
49	6.5	Computational Methods: Multithreading . . . . .	62
50	6.6	Analysis Results . . . . .	68
51	6.7	Systematics . . . . .	73
52	6.8	Conclusion and Discussion . . . . .	73
53	<b>CHAPTER 7</b>	<b>HEAVY DARK MATTER ANNIHILATION SEARCH WITH ICE-CUBE'S NORTH SKY TRACK DATA</b>	75
54	7.1	Introduction . . . . .	75
55	7.2	Dataset and Background . . . . .	76
56	7.3	Analysis . . . . .	77
57	7.4	Likelihood Methods . . . . .	85
58	7.5	Background Simulation . . . . .	86
59	<b>CHAPTER 8</b>	<b>NU DUCK</b> . . . . .	93
60	<b>APPENDIX A</b>	<b>MULTI-EXPERIMENT SUPPLEMENTARY FIGURES</b> . . . . .	94
61	<b>APPENDIX B</b>	<b>MULTITHREADING DARK MATTER ANALYSES SUPPLEMENTARY MATERIAL</b> . . . . .	95
62	B.1	Remaining Spectral Models . . . . .	95
63	B.2	<code>mpu_analysis.py</code> . . . . .	96
64	B.3	Comparison with Glory Duck . . . . .	105
65	<b>APPENDIX C</b>	<b>ICECUBE HEAVY DARK MATTER ANALYSIS SUPPLEMENTARY MATERIAL</b> . . . . .	108
66	C.1	Docker Image for Oscillating Neutrino Spectra . . . . .	108
67	C.2	Spline Fitting Statuses . . . . .	111
68	<b>BIBLIOGRAPHY</b> . . . . .		112

## LIST OF TABLES

<p>73    Table 5.1    Summary of the relevant properties of the dSphs used in the present work. Column 1 lists the dSphs. Columns 2 and 3 present their heliocentric distance and galactic coordinates, respectively. Columns 4 and 5 report the <math>J</math>-factors of each source given from the <math>\mathcal{GS}</math> and <math>\mathcal{B}</math> independent studies and their estimated <math>\pm 1\sigma</math> uncertainties. The values <math>\log_{10} J</math> (<math>\mathcal{GS}</math> set) [45] correspond to the mean <math>J</math>-factor values for a source extension truncated at the outermost observed star. The values <math>\log_{10} J</math> (<math>\mathcal{B}</math> set) [47] are provided for a source extension at the tidal radius of each dSph. <b>Bolded sources are within HAWC's field of view and provided to the Glory Duck analysis.</b> . . . . .</p> <p>82    Table 5.2    Summary of dSph observations by each experiment used in this work. A ‘-’ indicates the experiment did not observe the dSph for this study. For Fermi-LAT, the exposure at 1 GeV is given. For HAWC, <math> \Delta\theta </math> is the absolute difference between the source declination and HAWC latitude. HAWC is more sensitive to sources with smaller <math> \Delta\theta </math>. For IACTs, we show the zenith angle range, the total exposure, the energy range, the angular radius <math>\theta</math> of the signal or ON region, the ratio of exposures between the background-control (OFF) and signal (ON) regions (<math>\tau</math>), and the significance of gamma-ray excess in standard deviations, <math>\sigma</math>. . . . .</p> <p>91    Table 6.1    Summary of the relevant properties of the dSphs used in the present work. Column 1 lists the dSphs. Columns 2 and 3 present their heliocentric distance and galactic coordinates, respectively. Column 4 reports the <math>J</math>-factors of each source given from the <math>\mathcal{LS}</math> studies and estimated <math>\pm 1\sigma</math> uncertainties. The values <math>\log_{10} J</math> (<math>\mathcal{LS}</math> set) [65] correspond to the mean <math>J</math>-factor values for a source extension truncated at <math>0.5^\circ</math>. . . . .</p> <p>97    Table 6.2    Timing summaries for analyses for serial and multithreaded processes. <math>M</math> tasks is the number of functional-parallel tasks ran for the computation. <math>T_{p,c}</math> is a single run time in hours:minutes:seconds for runs utilizing <math>p</math> nodes and <math>c</math> threads. Runs are run interactively on the same computer to maximize consistency. Empty entries are indicated with ‘-’. (.) entries are estimated entries extrapolated from data earlier in the column. . . . .</p> <p>103    Table 6.3    Speed up summaries for analyses for serial and multithreaded processes. <math>M</math> tasks is the number of functional-parallel tasks ran for the computation. <math>S_{p,c}</math> is a single speedup comparison for runs utilizing <math>p</math> nodes and <math>c</math> threads. <math>[\cdot]</math> are the estimated speedups calculated from Tab. 6.2, Eq. (6.10), and Eq. (6.5). Empty entries are indicated with ‘-’. . . . .</p> <p>108    Table 7.1    <b>TODO: fill me daddy</b> . . . . .</p> <p>109              Proof I know how to include</p>	<p>31</p> <p>32</p> <p>62</p> <p>66</p> <p>68</p> <p>83</p>
--	---

## LIST OF FIGURES

111	Figure 2.1	Rotation curve fit to NGC 6503 from [7]. Dashed line is the contribution 112 from visible matter. Dotted curves are from gas. Dash-dot curves are from 113 dark matter (DM). Solid line is the composite contribution from all matter 114 and DM sources. Data are indicated with bold dots with error bars. Data 115 agree strongly with a matter + DM composite prediction. . . . .	5
116	Figure 2.2	Light from distant galaxy is bent in unique ways depending on the distribution 117 of mass between the galaxy and Earth. Yellow dashed lines indicate where 118 the light would have gone if the matter were not present [8]. . . . .	7
119	Figure 2.3	(left) Optical image of galactic cluster 1E0657-558. (right) X-ray image of the 120 cluster with redder meaning hotter and higher baryon density. (both) Green 121 contours are reconstruction of gravity contours from weak lensing. White 122 rings are the best fit mass maxima at 68.3%, 95.5%, and 99.7% confidence. 123 The matter maxima of the clusters are clearly separated from x-ray maxima. [9]	8
124	Figure 2.4	Plank CMB sky. Sky map features small variations in temperature in primor- 125 dial light. These anisotropies are used to make inferences about the universe's 126 energy budget and developmental history. [10] . . . . .	9
127	Figure 2.5	Observed Cosmic Microwave Background power spectrum as a function of 128 multipole moment from Plank [10]. Blue line is best fit model from $\Lambda$ CDM. 129 Red points and lines are data and error, respectively. . . . .	10
130	Figure 2.6	Predicted power spectra of CMB for different $\Omega_m h^2$ values for fixed baryon 131 density from [11]. (left) Low $\Omega_m h^2$ increases the prominence of first and 132 second peaks. (middle) $\Omega_m h^2$ is most similar to the observed power spectrum. 133 The second and third peaks are similar in height. (right) $\Omega_m h^2$ is large which 134 suppresses the first peak and raises the prominence of the third peak. . . . .	10
135	Figure 2.7	The Standard Model (SM) of particle physics. Figure taken from <a href="http://www.quantumdiaries.org/2014/03/14/the-standard-model-a-beautiful-but-flawed-theory/">http://www.quantumdiaries.org/2014/03/14/the-standard-model-a-beautiful-but-flawed-theory/</a> . . . . .	12
138	Figure 2.8	Simplified Feynman diagram demonstrating with different ways DM can 139 interact with SM particles. The 'X's refer to the DM particles whereas the 140 SM refer to fundamental particles in the SM. The large circle in the center 141 indicates the vertex of interaction and is purposely left vague. The colored 142 arrows refer to different directions of time as well as their respective labels. 143 The arrows indicate the initial and final state of the DM -SM interaction in time.	13

144	Figure 2.9 A single jet event in ATLAS detector from 2017 [16]. Jet momentum was 145 observed to be 1.9 TeV. Missing transverse momentum was observed to be 146 1.9 TeV compared to the initial transverse momentum of the event was 0. 147 Implied MET is traced by a red dashed line in event display. . . . .	14
148	Figure 2.10 More detailed pseudo-Feynman diagram of particle cascade from dark matter 149 annihilation into 2 quarks. The quarks hadronize and down to stable particles 150 like $\gamma$ or the anti-proton ( $p^-$ ). Diagram pulled from ICRC 2021 presentation 151 on DM annihilation search [17]. . . . .	15
152	Figure 2.11 Dark Matter (DM) decay spectrum for $b\bar{b}$ initial state and $\gamma$ final state. Redder 153 spectra are for larger DM masses. Bluer spectra are light DM masses. $x$ is a 154 unitless factor defined as the ratio of the mass of DM, $m_\chi$ , and the final state 155 particle energy $E_\gamma$ . Figure from [19]. . . . .	17
156	Figure 2.12 Different dark matter density profiles compared. Some models produce ex- 157 ceptionally large densities at small r [20]. . . . .	18
158	Figure 2.13 The Milky Way Galaxy in photons ( $\gamma$ ) and neutrinos ( $\nu$ ) [22]. The Galactic 159 center is at $l=0^\circ$ and is the brightest region in all panels. (top) An Optical 160 color image of the Milky Way galaxy seen from Earth. Clouds of gas and dust 161 obscure some light from stars. (2nd down) Integrated flux of $\gamma$ -rays observed 162 by the Fermi-LAT telescope [23]. (middle) Expected neutrino emission 163 that corresponds with Fermi-LAT observations. (2nd up) Expected neutrino 164 emission profile after considering detector systematics of IceCube. (bottom) 165 Observed neutrino emission from region of the galactic plane. Substantial 166 neutrino emission was detected. . . . .	19
167	Figure 2.14 Dark Matter annihilation spectra for different final state particle and standard 168 model annihilation channels [24]. Photons (red), $e^\pm$ (green), $\bar{p}$ (blue), $\nu$ (black). . . . .	20
169	Figure 5.1 Sensitivities of five gamma-ray experiments compared to percentages of the 170 Crab nebula's emission and dark matter annihilation. Solid lines present 171 estimated sensitivities to power law spectra [FACT CHECK THIS] for each 172 experiment. Green lines are Fermi-LAT sensitivities where lighter green is 173 the sensitivity to the galactic center and dark green is its sensitivity to higher 174 declinations. Orange, red, and purple solid lines represent the MAGIC, HESS, 175 and VERITAS 50 hour sensitivities respectively. The maroon and brown lines 176 are the HAWC 1 year and 5 year sensitivities. Across four decades of gamma- 177 ray energy, these experiments have similar sensitivities on the order $10^{-12}$ 178 $\text{erg cm}^{-2}\text{s}^{-1}$ . The dotted lines are estimated dark matter fluxes assuming 179 $m_\chi = 5 \text{ TeV}$ DM annihilating to bottom quarks (red), tau leptons (blue), 180 and W bosons (green). Faded gray lines outline percentage flux of the Crab 181 nebula. Figure is an augmented version of [25] . . . . .	24

182	Figure 5.2	Effect of Electroweak (EW) corrections on expected DM annihilation spectrum for $\chi\chi \rightarrow W^-W^+$ . Solid lines are spectral models that consider EW corrections. Dash-dot lines are spectral models without EW corrections. Red lines are models for $M_\chi = 1$ TeV. Blue lines represent models for $M_\chi = 100$ TeV. All models are sourced from the PPPC4DMID [44]. . . . .	28
187	Figure 5.3	$\frac{dJ}{d\Omega}$ maps for Segue1 (top) and Coma Berenices (bottom). Origin is centered on the specific dwarf spheroidal galaxies (dSph). X and Y axes are the angular separation from the center of the dwarf. Plots of the remaining 11 dSph HAWC studied are linked in Fig. A.1. . . . .	30
191	Figure 5.4	Illustration of the combination technique showing a comparison between $-2 \ln \lambda$ provided by four instruments (colored lines) from the observation of the same dSph without any $J$ nuisance and their sum, <i>i.e.</i> the resulting combined likelihood (thin black line). According to the test statistics of Equation (5.6), the intersection of the likelihood profiles with the line $-2 \ln \lambda = 2.71$ indicates the 95% C.L. upper limit on $\langle \sigma v \rangle$ . The combined likelihood (thin black line) shows a smaller value of upper limit on $\langle \sigma v \rangle$ than those derived by individual instruments. We also show how the uncertainties on the $J$ factor effects the combined likelihood and degrade the upper limit on $\langle \sigma v \rangle$ (thick black line). All likelihood profiles are normalized so that the global minimum $\widehat{\langle \sigma v \rangle}$ is 0. We note that each profile depends on the observational conditions in which a target object was observed. The sensitivity of a given instrument can be degraded and the upper limits less constraining if the observations are performed in non-optimal conditions such as a high zenith angle or a short exposure time. . . . .	35
206	Figure 5.5	. . . . .	38
207	Figure 5.6	HAWC TS values for best fit $\langle \sigma v \rangle$ versus $m_\chi$ for seven SM annihilation channels with $J$ factors from $\mathcal{GS}$ . The solid black line shows the combined best fit TS values. The colored, dashed lines are the TS values for each of the 13 sources HAWC studied. . . . .	39
211	Figure 5.7	HAWC Brazil bands at 95% confidence level on $\langle \sigma v \rangle$ versus DM mass for seven annihilation channels with $J$ -factors from $\mathcal{GS}$ [53]. The solid line represents the combined limit from 13 dSphs. The dashed line is the expected limit. The green band is the 68% containment. The yellow band is the 95% containment. . . . .	40

216	Figure 5.8	Upper limits at 95% confidence level on $\langle \sigma v \rangle$ in function of the DM mass for 217 eight annihilation channels, using the set of $J$ factors from Ref. [53] ( $\mathcal{GS}$ set 218 in Table 5.1). The black solid line represents the observed combined limit, 219 the black dashed line is the median of the null hypothesis corresponding 220 to the expected limit, while the green and yellow bands show the 68% and 221 95% containment bands. Combined upper limits for each individual detector 222 are also indicated as solid, colored lines. The value of the thermal relic 223 cross-section in function of the DM mass is given as the red dotted-dashed 224 line [54]. . . . .	41
225	Figure 5.9	Same as Fig. 5.8, using the set of $J$ factors from Ref. [47, 55] ( $\mathcal{B}$ set in Table 5.1). . . . .	42
226	Figure 5.10	Comparisons of the combined limits at 95% confidence level for each of the 227 eight annihilation channels when using the $J$ factors from Ref. [53] ( $\mathcal{GS}$ set in 228 Table 5.1), plain lines, and the $J$ factor from Ref. [47, 55] ( $\mathcal{B}$ set in Table 5.1), 229 dashed lines. The cross-section given by the thermal relic is also indicated [54]. . . . .	44
230	Figure 5.11	Comparisons of the combined limits at 95% confidence level for a point source 231 analysis and extended source using [53] $\mathcal{GS}$ J-factor distributions and PPPC 232 [44] annihilation spectra. Shown are the limits for Segue1 which will have 233 the most significant impact on the combined limit. 6 of the 7 DM annihilation 234 channels are shown. Solid lines are extended source studies. Dashed lines 235 are point source studies. Overall, the extended source analysis improves the 236 limit by a factor of 2. . . . .	46
237	Figure 5.12	Same as Fig. 5.11 on Coma Berenices. This dSph also contributes signifi- 238 cantly to the limit. The limits are identical in this case. . . . .	47
239	Figure 5.13	Comparison of combined limits when correcting for HAWC's pointing sys- 240 tematic. All DM annihilation channels are shown. The solid black line is the 241 ratio between published limit to the declination corrected limit. The blue solid 242 line or "Combined_og" represented the limits computed for Glory Duck. The 243 solid orange line or "Combined_ad" represented the limits computed after 244 correcting for the pointing systematic. . . . .	48
245	Figure 5.14	Differential map of $dJ/\Omega$ from model built in Section 5.8.1 and profiles 246 provided directly from authors. (Top) Differential from Segue1. (bottom) 247 Differential from Coma Berenices. Note that their scales are not the same. 248 Segue1 shows the deepest discrepancies which is congruent with its large 249 uncertainties. Both models show anuli where unique models become apparent. . . . .	49

250	Figure 5.15 HAWC limits for Coma Berenices (top) and Segue1 (bottom) for two different map sets. Blue lines are limits calculated on maps with poor model representation. Orange lines are limits calculated on spatial profiles provided by the authors of [45]. Black line is the ratio of the poor spatial model limits to the corrected spatial models. The left y-axis measures $\langle \sigma v \rangle$ for the blue and orange lines. The right y-axis measures the ratio and is unitless. . . . .	50
251		
252		
253		
254		
255		
256	Figure 5.16 Comparisons between the $J$ -factors versus the angular radius for the computation of $J$ factors from Ref. [53] ( $\mathcal{GS}$ set in Table 5.1) in blue and for the computation from Ref. [47, 55] ( $\mathcal{B}$ set in Tab. 5.1) in orange. The solid lines represent the central value of the $J$ -factors while the shaded regions correspond to the $1\sigma$ standard deviation. . . . .	53
257		
258		
259		
260		
261	Figure 5.17 Comparisons between the $J$ -factors versus the angular radius for the computation of $J$ factors from Ref. [53] ( $\mathcal{GS}$ set in Tab. 5.1) in blue and for the computation from Ref. [47, 55] ( $\mathcal{B}$ set in Tab. 5.1) in orange. The solid lines represent the central value of the $J$ -factors while the shaded regions correspond to the $1\sigma$ standard deviation. . . . .	54
262		
263		
264		
265		
266	Figure 6.1 Difference between spectral hypotheses from PPPC [44] and HDM [64]. Shown is the expected DM annihilation spectrum for $\chi\chi \rightarrow W^-W^+$ . Solid lines are spectral models with EW corrections from the PPPC. Dash-dot lines are spectral models from HDM. Red lines are models for $M_\chi = 1$ TeV. Blue lines represent models for $M_\chi = 100$ TeV. . . . .	59
267		
268		
269		
270		
271	Figure 6.2 Photon spectra for $\chi\chi \rightarrow \gamma\gamma$ (left) and $\chi\chi \rightarrow ZZ$ (right) after Gaussian convolution of line features. Both spectra have $\delta$ -features at photon energies equal to the DM mass. Bluer lines are annihilation spectra with lower DM mass. Redder lines are spectra from larger DM mass. All Spectral models are sourced from the Heavy Dark Matter models [64]. Axes are drawn roughly according to the energy sensitivity of HAWC. . . . .	60
272		
273		
274		
275		
276		
277	Figure 6.3 $\frac{dJ}{d\Omega}$ maps for Coma Berenices, Draco, Segue1, and Sextans. Columns are divided for the $\pm 1\sigma$ uncertainties in $dJ/d\Omega$ around the mean value from $\mathcal{LS}$ [65]. Origin is centered on the specific dwarf spheroidal galaxies (dSph). $\theta$ and $\phi$ axes are the angular separation from the center of the dwarf . . . . .	61
278		
279		
280		
281	Figure 6.4 Infographic on how jobs and DM computation was organized in Section 5.3. Jobs were built for each permutation of CHANS and SOURCES shown by the left block in the figure. Each job, which took on the order 2 hrs to compute, had the following work flow: 1. Import HAWC analysis software, 2 min to run. 2. Load HAWC count maps, 5 min to run. 3. Load HAWC energy and spatial resolutions, 4 min. 5. Load DM spatial source templates and spectral models, less than 1 s. 6. Perform likelihood fit on data and model, about 8 min per DM mass. 7. Write results to file, less than 1s. . . . .	63
282		
283		
284		
285		
286		
287		
288		

289	Figure 6.5	Graphic of Gustafson parallel coding pattern. $f_s$ is the fraction of a program, in time, spent on serial computation. $f_p$ is the fraction of computing time that is parallelizable. $T_p$ is the total time for a parallel program to run. $T_1$ is the total time for a parallel program to run if only 1 processor is allocated. $P_N$ is the $N$ -th processor where it's row is the computation the processor performs. The Gustafson pattern is most similar to what is implemented for this analysis. Figure is pulled from [67]. . . . .	64
296	Figure 6.6	Task chart for one multithreaded job developed for this project. Green blocks indicate a shared resource across the threads AND computation performed serially. Red blocks indicate functional parallel processing within each thread. 3 threads are represented here, yet many more can be employed during the full analysis. Jobs are defined by the SOURCE as these require unique maps to be loaded into the likelihood estimator. The $m_\chi$ , CHAN, and $\langle\sigma v\rangle$ variables are entered into the thread pool and allocated as evenly as possible across the threads. . . . .	66
304	Figure 6.7	HAWC upper limits at 95% confidence level on $\langle\sigma v\rangle$ versus DM mass for $\chi\chi \rightarrow b\bar{b}, t\bar{t}, u\bar{u}, d\bar{d}, s\bar{s}, c\bar{c}, gg, W^+W^-$ , and $hh$ . Limits are with $\mathcal{LS}$ $J$ - factors [65]. The solid line represents the observed combined limit. Dashed lines represent limits from individual dSphs. . . . .	69
308	Figure 6.8	HAWC upper limits at 95% confidence level on $\langle\sigma v\rangle$ versus DM mass for $\chi\chi \rightarrow \nu_e\bar{\nu}_e, \nu_\mu\bar{\nu}_\mu, \nu_\tau\bar{\nu}_\tau, e\bar{e}, \mu\bar{\mu}, \tau\bar{\tau}, \gamma\gamma$ and $ZZ$ . Limits use $\mathcal{LS}$ $J$ factors [65]. The solid line represents the observed combined limit. Dashed lines represent limits from individual dSphs. . . . .	70
312	Figure 6.9	HAWC TS values for best fit $\langle\sigma v\rangle$ versus $m_\chi$ for SM annihilation channels: $\chi\chi \rightarrow b\bar{b}, t\bar{t}, u\bar{u}, d\bar{d}, s\bar{s}, c\bar{c}, gg, W^+W^-$ , and $hh$ . Limits use $\mathcal{LS}$ $J$ factors. The solid black line shows the combined best fit TS values. The colored, dashed lines are the TS values from each dSph. . . . .	71
316	Figure 6.10	HAWC TS values for best fit $\langle\sigma v\rangle$ versus $m_\chi$ for SM annihilation channels: $\chi\chi \rightarrow \nu_e\bar{\nu}_e, \nu_\mu\bar{\nu}_\mu, \nu_\tau\bar{\nu}_\tau, e\bar{e}, \mu\bar{\mu}, \tau\bar{\tau}, \gamma\gamma$ and $ZZ$ . Limits use $\mathcal{LS}$ $J$ factors. The solid black line shows the combined best fit TS values. The colored, dashed lines are the TS values from each dSph. . . . .	72
320	Figure 6.11	Comparison of HAWC limits from this analysis to Glory Duck (Fig. 5.5) for 3 dSphs and 3 SM annihilation channels: $b\bar{b}, \tau\bar{\tau}$ , and $e\bar{e}$ . Each sector shows the 95% confidence limit from Glory Duck (blue line) and this analysis (orange line) in the top plot. The lower plot features the ratio in log scale of Glory Duck to this analysis in a red solid line. Horizontal dashed lines are for ratios of 1.0 (black) and $\sqrt{2}$ (blue). Ratios larger than 1.0 are for limits smaller, or stricter, than Glory Duck. Ratios larger than $\sqrt{2}$ indicates limits are stricter than a simple doubling of the Glory Duck data. . . . .	74

328	Figure 7.1	Neutrino spectra at production (left panels) and after oscillation at Earth 329 (right panels). Blue, orange, and green lines are the $\nu_e$ , $\nu_\mu$ , and $\nu_\tau$ spectra 330 respectively. Top panels show the spectra in $\frac{dN}{dE}$ . Lower panels plot the flavor 331 ratio to $\nu_e + \nu_\mu + \nu_\tau$ . SM annihilation channels $b\bar{b}$ , $\tau\bar{\tau}$ , and $\nu_\mu\bar{\nu}_\mu$ are shown 332 for $M_\chi = 1$ PeV, TeV, and EeV. . . . .	79
333	Figure 7.2	Signal recovery for 100 TeV DM annihilation into $\nu_\mu\bar{\nu}_\mu$ for a source at Dec 334 = 16.06°. $n_{\text{inj}}$ is the number of injected signal events in simulation. $n_s$ is 335 the number of reconstructed signal events from the simulation. Although 336 the uncertainties are small and tight, the reconstructed $n_s$ are systematically 337 underestimated. . . . .	80
338	Figure 7.3	Top left panel shows the two kernels overlayed the original spectrum from 339 Charon. delta I is the difference in the integral of the peaks with respect to the 340 original spectrum. The vertical red line indicated where the original neutrino 341 line is maximized. Lower right shows the signal recovers of the DM model 342 using the Gaussian kernel with parameters enumerated above. . . . .	81
343	Figure 7.4	Example spline that failed the fit. Failed splined are corrected on a case by 344 case basis unless the SM channel has a systematic problem fitting the splines. 345 In this case, I made a bookkeeping error and loaded the incorrected neutrino 346 flavor . . . . .	83
347	Figure 7.5	<b>TODO: Show the post processed spectra that you are sampling[NEEDS A 348 SOURCE][FACT CHECK THIS]</b> . . . . .	84
349	Figure 7.6	<b>TODO: update text because there is no title.</b> Each subplot, except the final, is 350 the TS distribution for a specific DM mass listed in the subplot. The final 351 subplot plots the all DM spectral models used as input for the TS distribution 352 calculations with bluer lines indicating lower DM mass and redder indicating 353 higher DM mass. . . . .	87
354	Figure 7.7	<b>TODO: update text because there is no title.</b> Each subplot, except the final, is 355 the TS distribution for a specific DM mass listed in the subplot. The final 356 subplot plots the all DM spectral models used as input for the TS distribution 357 calculations with bluer lines indicating lower DM mass and redder indicating 358 higher DM mass. . . . .	88
359	Figure 7.8	<b>TODO: update text because there is no title.</b> Each subplot, except the final, is 360 the TS distribution for a specific DM mass listed in the subplot. The final 361 subplot plots the all DM spectral models used as input for the TS distribution 362 calculations with bluer lines indicating lower DM mass and redder indicating 363 higher DM mass. . . . .	89

364	Figure 7.9	<b>TODO: update text because there is no title.</b> Each subplot, except the final, is the TS distribution for a specific DM mass listed in the subplot. The final subplot plots the all DM spectral models used as input for the TS distribution calculations with bluer lines indicating lower DM mass and redder indicating higher DM mass. . . . .	90
369	Figure 7.10	<b>TODO: update text because there is no title.</b> Each subplot, except the final, is the TS distribution for a specific DM mass listed in the subplot. The final subplot plots the all DM spectral models used as input for the TS distribution calculations with bluer lines indicating lower DM mass and redder indicating higher DM mass. . . . .	91
374	Figure 7.11	<b>TODO: update text because there is no title.</b> Each subplot, except the final, is the TS distribution for a specific DM mass listed in the subplot. The final subplot plots the all DM spectral models used as input for the TS distribution calculations with bluer lines indicating lower DM mass and redder indicating higher DM mass. . . . .	92
379	Figure A.1	Sister figure to Figure 5.3. Sources in the first row from left to right: Bootes I, Canes Venatici I, II. In second row: Draco, Hercules, Leo I. In the first row: Leo II, Leo IV, Sextans. In the final row: Ursa Major I, Ursa Major II. . . . .	94
382	Figure B.1	Sister figure to Figure 6.2 for remaining SM primary annihilation channels studied for this thesis. These did not require any post generation smoothing and so are directly pulled from [64] with a binning scheme most helpful for a HAWC analysis. . . . .	95
386	Figure B.2	<b>TODO: fill this out</b> . . . . .	105
387	Figure B.3	<b>TODO: fill this out</b> . . . . .	106
388	Figure B.4	<b>TODO: fill this out</b> . . . . .	107
389	Figure C.1	<b>TODO: fill me daddy</b> . . . . .	111

**LIST OF ABBREVIATIONS**

- 391 **MSU** Michigan State University  
392 **LANL** Los Alamos National Laboratory  
393 **DM** Dark Matter  
394 **SM** Standard Model  
395 **HAWC** High Altitude Water Cherenkov Observatory  
396 **dSph** Dwarf Spheroidal Galaxy

## CHAPTER 1

### INTRODUCTION

398 Is the text not rendering right? Ah ok it knows im basically drafting the doc still

## CHAPTER 2

399

### DARK MATTER IN THE COSMOS

#### 400 2.1 Introduction

401 The dark matter problem can be summarized in part by the following thought experiment.

402 Let us say you are the teacher for an elementary school classroom. You take them on a field  
403 trip to your local science museum and among the exhibits is one for mass and weight. The exhibit  
404 has a gigantic scale, and you come up with a fun problem for your class.

405 You ask your class, "What is the total weight of the classroom? Give your best estimation to  
406 me in 30 minutes, and then we'll check your guess on the scale. If your guess is within 10% of the  
407 right answer, we will stop for ice cream on the way back."

408 The students are ecstatic to hear this, and they get to work. The solution is some variation of  
409 the following strategy. The students should give each other their weight or best guess if they do  
410 not know. Then, all they must do is add each student's weight and get a grand total for the class.

411 The measurement on the giant scale should show the true weight of the class. When comparing  
412 the measured weight to your estimation, multiply the measurement by  $1.0 \pm 0.1$  to get the  $\pm 10\%$   
413 tolerances for your estimation.

414 Two of your students, Sandra and Mario, return to you with a solution.

415 They say, "We weren't sure of everyone's weight. We used 65 lbs. for the people we didn't  
416 know and added everyone who does know. There are 30 of us, and we got 2,000 lbs.! That's a ton!"

417 You estimated 1,900 lbs. assuming the average weight of a student in your class was 60 lbs.  
418 So, you are pleased with Sandra's and Mario's answer. You instruct your students to all gather on  
419 the giant scale and read off the weight together. To all your surprise, the scale reads *10,000 lbs.*!  
420 10,000 is significantly more than a 10% error from 2,000. In fact, it is approximately 5 times more  
421 massive than either your or your students' estimates. You think to yourself and conclude there  
422 must be something wrong with the scale. You ask an employee to check the scale and verify it is  
423 well calibrated. They confirm that the scale is in working order. You weigh a couple of students  
424 individually to assess that the scale is well calibrated. Sandra weighs 59 lbs., and Mario weighs

425 62 lbs., typical weights for their age. You then weigh each student individually and see that their  
426 weights individually do not deviate greatly from 60 lbs. So, where does all the extra weight come  
427 from?

428 This thought experiment serves as an analogy to the Dark Matter problem. The important  
429 substitution to make however is to replace the students with stars and the classroom with a galaxy,  
430 say the Milky Way. Individually the mass of stars is well measured and defined with the Sun as our  
431 nearest test case. However, when we set out to measure the mass of a collection of stars as large as  
432 galaxies, our well-motivated estimation is wildly incorrect. There simply is no way to account for  
433 this discrepancy except without some unseen, or dark, contribution to mass and matter in galaxies.  
434 I set out in my thesis to narrow the possibilities of what this Dark Matter could be.

435 This chapter is organized like the following... **TODO: Text should look like ... Chapter x has**  
436 **blah blah blah.**

## 437 2.2 Dark Matter Basics

438 Presently, a more compelling theory of cosmology that includes Dark Matter (DM) in order  
439 to explain a variety of observations is  $\Lambda$  Cold Dark Matter, or  $\Lambda$ CDM. I present the evidence  
440 supporting  $\Lambda$ CDM in Section 2.3 yet discuss the conclusions of the  $\Lambda$ CDM model here. According  
441 to  $\Lambda$ CDM fit to observations on the Cosmic Microwave Background (CMB), DM is 26.8% of the  
442 universe's current energy budget. Baryonic matter, stuff like atoms, gas, and stars, contributes to  
443 4.9% of the universe's current energy budget [1, 2, 3].

444 DM is dark; it does not interact readily with light at any wavelength. DM also does not interact  
445 noticeably with the other standard model forces (Strong and Weak) at a rate that is readily observed  
446 [3]. DM is cold, which is to say that the average velocity of DM is below relativistic speeds [1].  
447 'Hot' DM would not likely manifest the dense structures we observe like galaxies, and instead  
448 would produce much more diffuse galaxies than what is observed [3, 1]. DM is old; it played a  
449 critical role in the formation of the universe and the structures within it [1, 2].

450 Observations of DM have so far been only gravitational. The parameter space available to what  
451 DM could be therefore is extremely broad. The broad DM parameter space is iteratively tested in

452 DM searches by supposing a hypothesis that has not yet been ruled out and performing observations  
453 to test them. When the observations yield a null result, the parameter space is constrained further.  
454 I present some approaches for DM searches in Section 2.4.

455 **2.3 Evidence for Dark Matter**

456 Dark Matter (DM) has been a looming problem in physics for almost 100 years. Anomalies  
457 have been observed by astrophysicists in galactic dynamics as early as 1933 when Fritz Zwicky  
458 noticed unusually large velocity dispersion in the Coma cluster. Zwicky's measurement was the  
459 first recorded to use the Virial theorem to measure the mass fraction of visible and invisible matter  
460 in celestial bodies [4]. From Zwicky in [5], "*If this would be confirmed, we would get the surprising*  
461 *result that dark matter is present in much greater amount than luminous matter.*" Zwicky's and  
462 others' observation did not instigate a crisis in astrophysics because the measurements did not  
463 entirely conflict with their understanding of galaxies [4]. In 1978, Rubin, Ford, and Norbert  
464 measured rotation curves for ten spiral galaxies [6]. Rubin et al.'s 1978 publication presented a  
465 major challenge to the conventional understanding of galaxies that could no longer be dismissed by  
466 measurement uncertainties. Evidence has been mounting ever since for this exotic form of matter.  
467 The following subsections provide three compelling pieces of evidence in support of the existence  
468 of DM.

469 **2.3.1 First Clues: Stellar Velocities**

470 Zwicky, and later Rubin, measured the stellar velocities of various galaxies to estimate their  
471 virial mass. The Virial Theorem upon which these observations are interpreted is written as

$$2T + V = 0. \quad (2.1)$$

472 Where  $T$  is the kinetic energy and  $V$  is the potential energy in a self-gravitating system. The  
473 classical Newton's law of gravity from stars and gas was used for gravitational potential modeled in  
474 the observed galaxies:

$$V = -\frac{1}{2} \sum_i \sum_{j \neq i} \frac{m_i m_j}{r_{ij}}. \quad (2.2)$$

475 Zwicky et al. measured just the velocities of stars apparent in optical wavelengths [5]. Rubin et al.  
 476 added by measuring the velocity of the hydrogen gas via the 21 cm emission line of Hydrogen [6].  
 477 The velocities of the stars and gas are used to infer the total mass of galaxies and galaxy clusters  
 478 via Equation (2.1). An inferred mass is obtained from the luminosity of the selected sources. The  
 479 two inferences are compared to each other as a luminosity to mass ratio which typically yielded [1]

$$\frac{M}{L} \sim 400 \frac{M_{\odot}}{L_{\odot}} \quad (2.3)$$

480  $M_{\odot}$  and  $L_{\odot}$  referring to stellar mass and stellar luminosity, respectively. These ratios clearly indicate  
 481 a discrepancy in apparent light and mass from stars and gas and their velocities.

482 Rubin et al. [6] demonstrated that the discrepancy was unlikely to be an underestimation of  
 483 the mass of the stars and gas. The inferred "dark" mass was up to 5 times more than the luminous  
 484 mass. This dark mass also needed to extend well beyond the extent of the luminous matter.

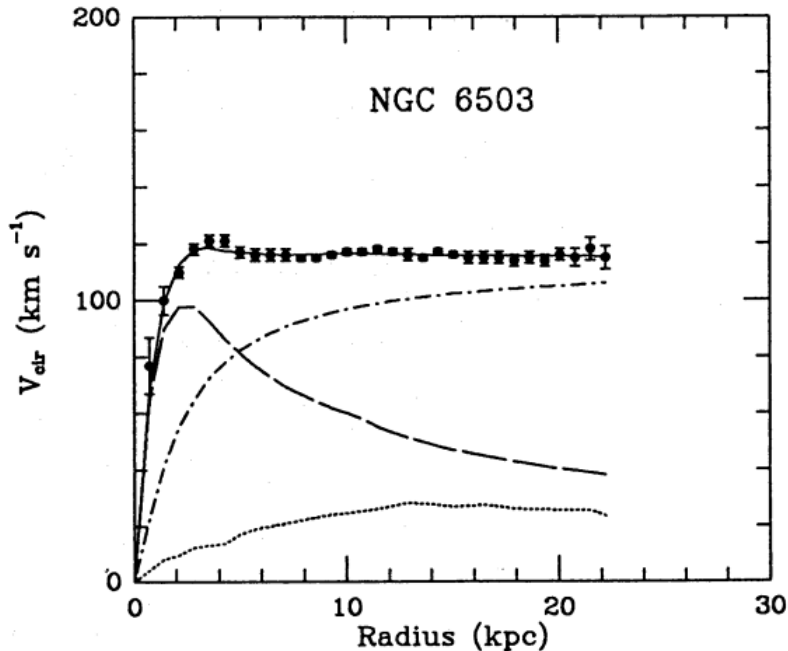


Figure 2.1 Rotation curve fit to NGC 6503 from [7]. Dashed line is the contribution from visible matter. Dotted curves are from gas. Dash-dot curves are from dark matter (DM). Solid line is the composite contribution from all matter and DM sources. Data are indicated with bold dots with error bars. Data agree strongly with a matter + DM composite prediction.

485 Figure 2.1 features one of many rotation curves plotted from the stellar velocities within galaxies.

486 The measured rotation curves mostly feature a flattening of velocities at higher radius which is not  
487 expected if the gravity was only coming from gas and luminous matter. The extension of the  
488 flat velocity region also indicates that the DM is distributed far from the center of the galaxy.  
489 Modern velocity measurements include significantly larger objects, galactic clusters, and smaller  
490 objects, dwarf galaxies. Yet, measurements along this regime are leveraging the Virial theorem  
491 with Newtonian potential energies. We know Newtonian gravity is not a comprehensive description  
492 of gravity. New observational techniques have been developed since 1978, and those are discussed  
493 in the following sections.

494 **2.3.2 Evidence for Dark Matter: Gravitational Lensing**

495 Modern evidence for dark matter comes from new avenues beyond stellar velocities. Grav-  
496 itational lensing from DM is a new channel from general relativity. General relativity predicts  
497 aberrations in light caused by massive objects. In recent decades we have been able to measure the  
498 lensing effects from compact objects and DM halos. Figure 2.2 shows how different massive ob-  
499 jects change the final image of a faraway galaxy resulting from gravitational lensing. Gravitational  
500 lensing developed our understanding of dark matter in two important ways.

501 Gravitational lensing provides additional compelling evidence for DM. The observation of two  
502 merging galactic clusters in 2006, shown in Figure 2.3, provided a compelling argument for DM  
503 outside the Standard Model. These clusters merged recently in astrophysical time scales. Galaxies  
504 and star cluster have mostly passed by each other as the likelihood of their collision is low. Therefore,  
505 these massive objects will mostly track the highest mass, dark and/or baryonic, density. Yet, the  
506 intergalactic gas is responsible for the majority of the baryonic mass in the systems [4]. These gas  
507 bodies will not phase through and will heat up as they collide together. The hot gas is located via  
508 x-ray emission from the cluster. Two observations of the clusters were performed independently of  
509 each other.

510 The first was the lensing of light around the galaxies due to their gravitational influences.  
511 When celestial bodies are large enough, the gravity they exert bends space and time itself. The  
512 warped space-time lenses light and will deflect in an analogous way to how glass lenses will bend

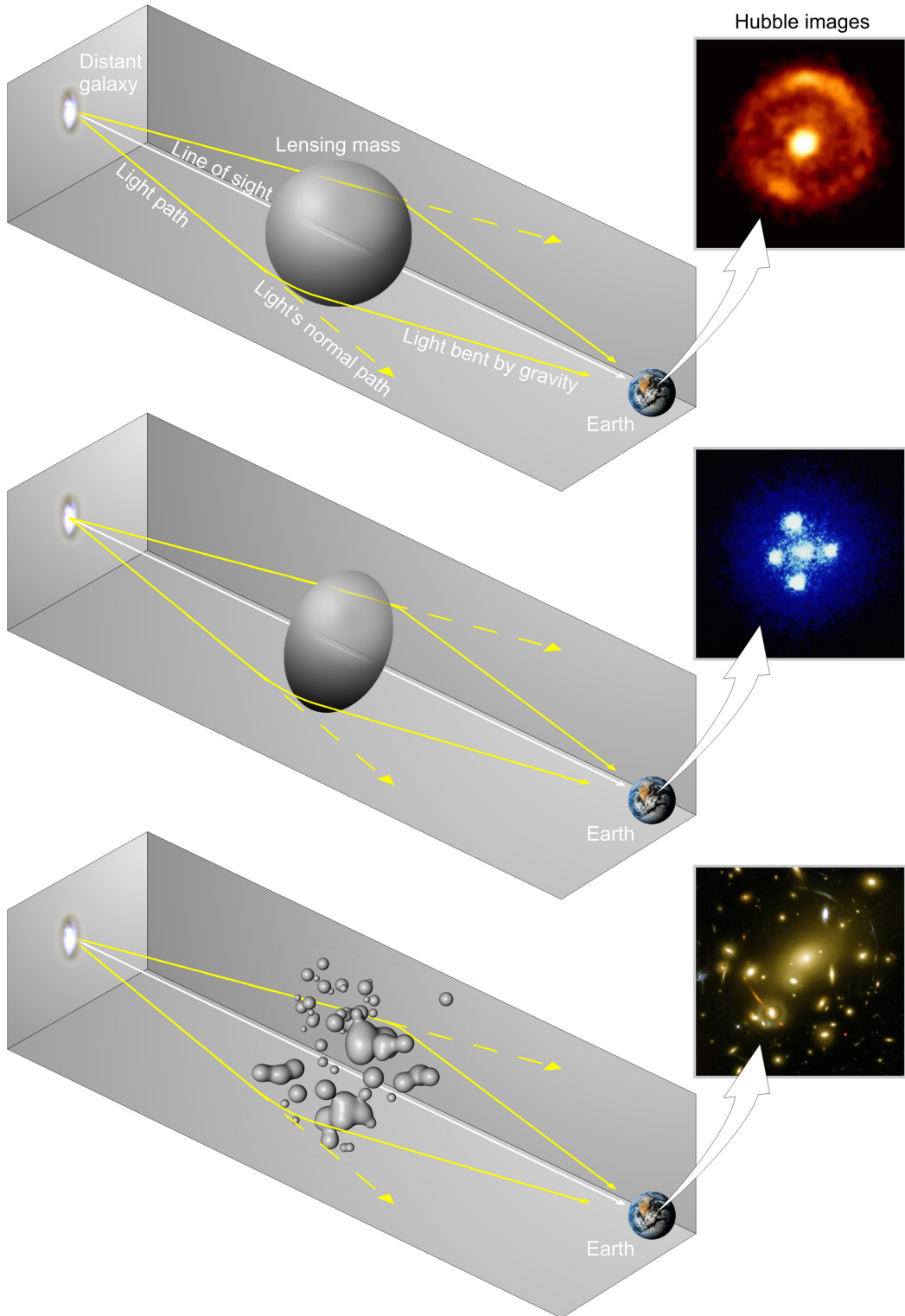


Figure 2.2 Light from distant galaxy is bent in unique ways depending on the distribution of mass between the galaxy and Earth. Yellow dashed lines indicate where the light would have gone if the matter were not present [8].

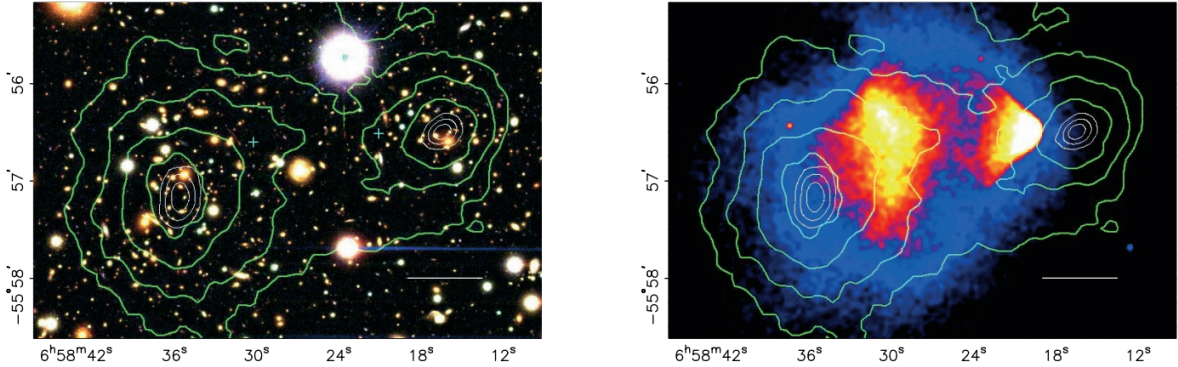


Figure 2.3 (left) Optical image of galactic cluster 1E0657-558. (right) X-ray image of the cluster with redder meaning hotter and higher baryon density. (both) Green contours are reconstruction of gravity contours from weak lensing. White rings are the best fit mass maxima at 68.3%, 95.5%, and 99.7% confidence. The matter maxima of the clusters are clearly separated from x-ray maxima. [9]

513 light, see Figure 2.2. With a sufficient understanding of light sources behind a massive object, we  
 514 can reconstruct the contours of the gravitational lenses. The gradient of the contours shown in  
 515 Figure 2.3 then indicates how dense the matter is and where it is.

516 The x-ray emission can then be observed from the clusters. Since these galaxies are mostly gas  
 517 and are merging, then the gas should be getting hotter. If they are merging, the x-ray emissions  
 518 should be the strongest where the gas is mostly moving through each other. Hence, X-ray emission  
 519 maps out where the gas is in the merging galaxy cluster.

520 The lensing and x-ray observations were done on the Bullet cluster featured on Figure 2.3.  
 521 The x-ray emissions do not align with the gravitational contours from lensing. The incongruence  
 522 in mass density and baryon density suggests that there is a lot of matter somewhere that does  
 523 not interact with light. Moreover, this dark matter cannot be baryonic [9]. The Bullet Cluster  
 524 measurement did not really tell us what DM is exactly, but it did give the clue that DM also does  
 525 not interact with itself very strongly. If DM did interact strongly with itself, then it would have been  
 526 more aligned with the x-ray emission [9]. There have been follow-up studies of galaxy clusters with  
 527 similar results. The Bullet Cluster and others like it provide a persuasive case against something  
 528 possibly amiss in our gravitational theories.

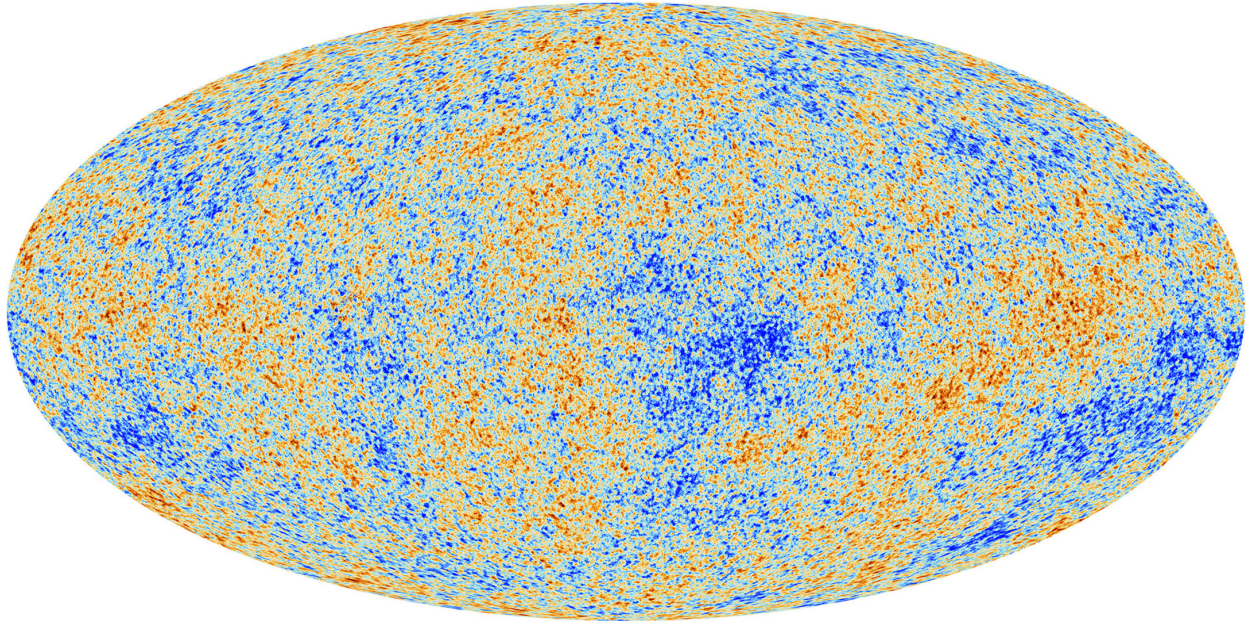


Figure 2.4 Plank CMB sky. Sky map features small variations in temperature in primordial light. These anisotropies are used to make inferences about the universe’s energy budget and developmental history. [10]

529     **2.3.3 Evidence for Dark Matter: Cosmic Microwave Background**

530       The Cosmic Microwave Background (CMB) is the primordial light from the early universe  
531       when Hydrogen atoms formed from the free electron and proton soup in the early universe. The  
532       CMB is the earliest light we can observe; released when the universe was about 380,000 years old.  
533       Then we look at how the simulated universes look like compared to what we see. Figure 2.4 is the  
534       most recent CMB image from the Plank satellite after subtracting the average value and masking the  
535       galactic plane [10]. Redder regions indicate a slightly hotter region in the CMB, and blue indicates  
536       colder. The intensity variations are on the order of 1 in 1000 with respect to the average value.

537       The Cosmic Microwave Background shows that the universe had DM in it from an incredibly  
538       early stage. To measure the DM, Dark Energy, and matter fractions of the universe from the CMB,  
539       the image is analyzed into a power spectrum, which shows the amplitude of the fluctuations as  
540       a function of spherical multipole moments.  $\Lambda$ CDM provides the best fit to the power spectra of  
541       the CMB as shown in Figure 2.5. The CMB power spectrum is quite sensitive to the fraction  
542       of each energy contribution in the early universe. Low  $l$  modes are dominated by variations  
543       in gravitational potential. Intermediate  $l$  emerge from oscillations in photon-baryon fluid from

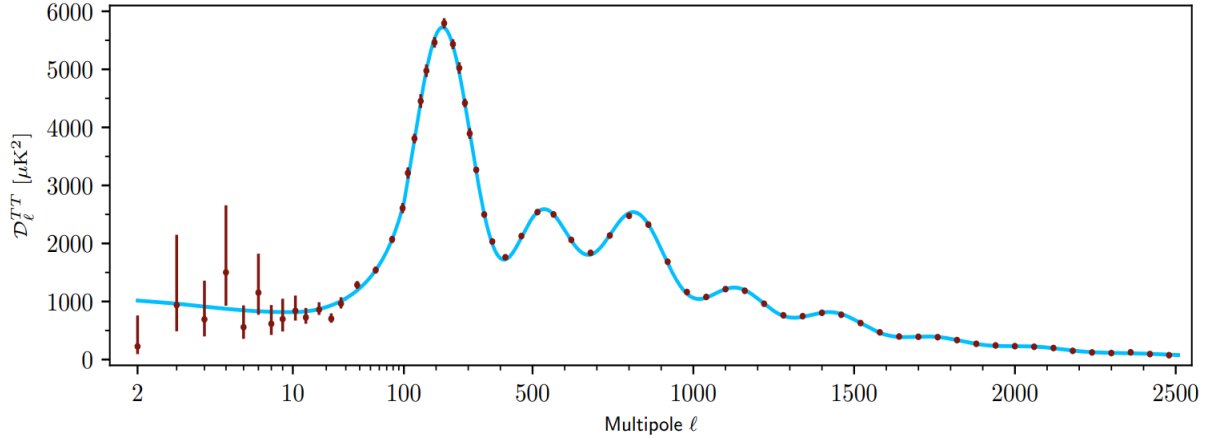


Figure 2.5 Observed Cosmic Microwave Background power spectrum as a function of multipole moment from Plank [10]. Blue line is best fit model from  $\Lambda$ CDM. Red points and lines are data and error, respectively.

544 competing baryon pressures and gravity. High  $l$  is a damped region from the diffusion of photons  
 545 during electron-proton recombination. [1]

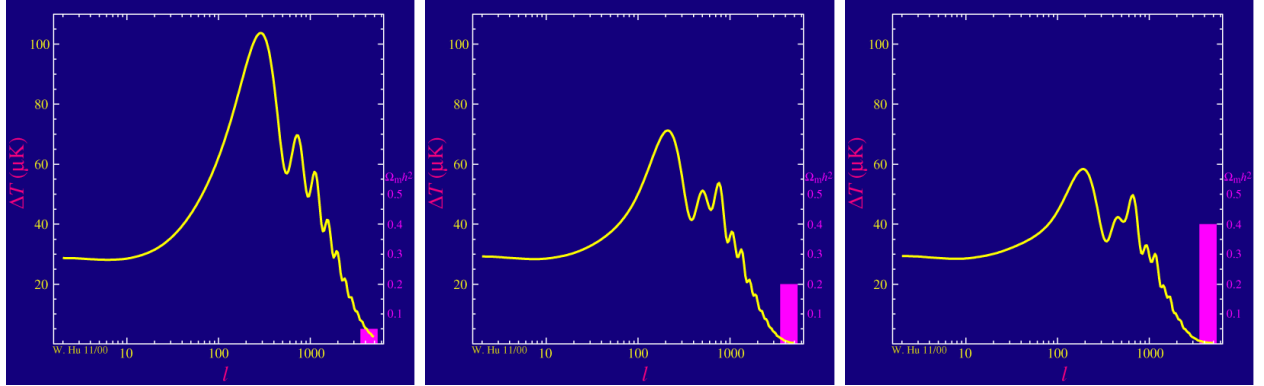


Figure 2.6 Predicted power spectra of CMB for different  $\Omega_m h^2$  values for fixed baryon density from [11]. (left) Low  $\Omega_m h^2$  increases the prominence of first and second peaks. (middle)  $\Omega_m h^2$  is most similar to the observed power spectrum. The second and third peaks are similar in height. (right)  $\Omega_m h^2$  is large which suppresses the first peak and raises the prominence of the third peak.

546 The harmonics would look quite different for a universe with less DM. Figure 2.6 demonstrates  
 547 the effect  $\Omega_m h^2$  has on the expected power spectrum for fixed baryon matter density. [11] Sweeping  
 548  $\Omega_m h^2$  in this way clearly shows the effect dark matter has on the CMB power spectrum. The  
 549 observations fit well with the  $\Lambda$ CDM model, and the derived fractions are as follows. The matter  
 550 fraction:  $\Omega_m = 0.3153$ ; and the baryon fraction:  $\Omega_b = 0.04936$  [10]. Plank's observations also  
 551 provide a measure of the Hubble constant,  $H_0$ .  $H_0$  especially has seen a growing tension in the

552 past decade that continues to deepened with observations from instruments like the James Webb  
553 Telescope [12, 13]. As Hubble tensions deepen, we may find that perhaps  $\Lambda$ **CDM**, despite its  
554 successes, is missing some critical physics.

555 Overall, the Newtonian motion of stars in galaxies, weak lensing from galactic clusters, and  
556 power spectra from primordial light form a compelling body of research in favor of dark matter.  
557 It takes another leap of theory and experimentation to make observations of DM that are non-  
558 gravitational in nature. In Section 2.3, the evidence for DM implies strongly that the DM is matter  
559 and not a lost parameter in the gravitational fields between massive objects. Finally, if we take one  
560 axiom: that this matter has quantum behavior, such as being described by some Bohr wavelength  
561 and abiding by some fermion or boson statistics; then we arrive at particle dark matter. One particle  
562 DM hypothesis is the Weakly Interacting Massive Particle (WIMP). This DM candidate theory is  
563 discussed further in the next section and is the focus of this thesis.

564 **2.4 Searching for Dark Matter: Particle DM**

565 Section 2.4 shows the Standard Model of particle physics and is currently the most accurate  
566 model for the dynamics of fundamental particles like electrons and photons. The current status  
567 of the SM does not have a viable DM candidate. When looking at the standard model, we can  
568 immediately exclude any charged particle because charged particles interact strongly with light.  
569 Specifically, this will rule out the following charged, fundamental particles:  $e, \mu, \tau, W, u, d, s, c, t, b$   
570 and their corresponding antiparticles. Recalling from Section 2.2 that DM must be long-lived and  
571 stable over the age of the universe which excludes all SM particles with decay half-lives at or shorter  
572 than the age of the universe. The lifetime constraint additionally eliminates the  $Z$  and  $H$  bosons.  
573 Finally, the candidate DM needs to be somewhat massive. Recall from Section 2.2 that DM is cold  
574 or not relativistic through the universe. This eliminates the remaining SM particles:  $\nu_{e,\mu,\tau}, g, \gamma$  as  
575 DM candidates. Because there are no DM candidates within the SM, the DM problem strongly  
576 hints to physics beyond the SM (BSM).

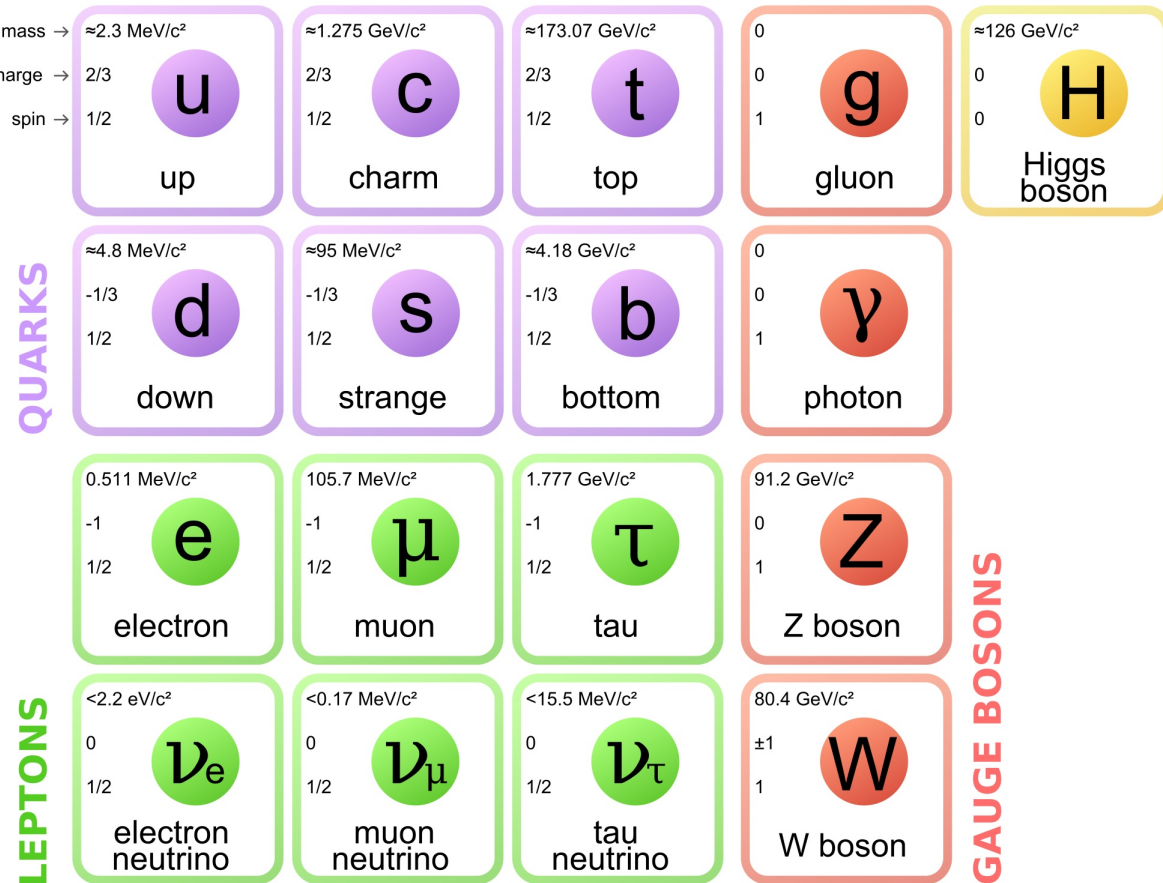


Figure 2.7 The Standard Model (SM) of particle physics. Figure taken from <http://www.quantumdiaries.org/2014/03/14/the-standard-model-a-beautiful-but-flawed-theory/>

### 577 2.4.1 Shake it, Break it, Make it

578 When considering DM that couples in some way with the SM, the interactions are roughly  
 579 demonstrated by interaction demonstrated in Figure 2.8. The figure is a simplified Feynman  
 580 diagram where the arrow of time represents the interaction modes of: **Shake it, Break it, Make it.**

581 **Shake it** refers to the direct detection of dark matter. Direct detection interactions start with  
 582 a free DM particle and an SM particle. The DM and SM interact via elastic or inelastic collision  
 583 and recoil away from each other. The DM remains in the dark sector and imparts some momentum  
 584 onto the SM particle. The hope is that the momentum imparted onto the SM particle is sufficiently  
 585 high enough to pick up with extremely sensitive instruments. Because we cannot create the DM in  
 586 the lab, a direct detection experiment must wait until DM is incident on the detector. Most direct  
 587 detection experiments are therefore placed in low-background environments with inert detection

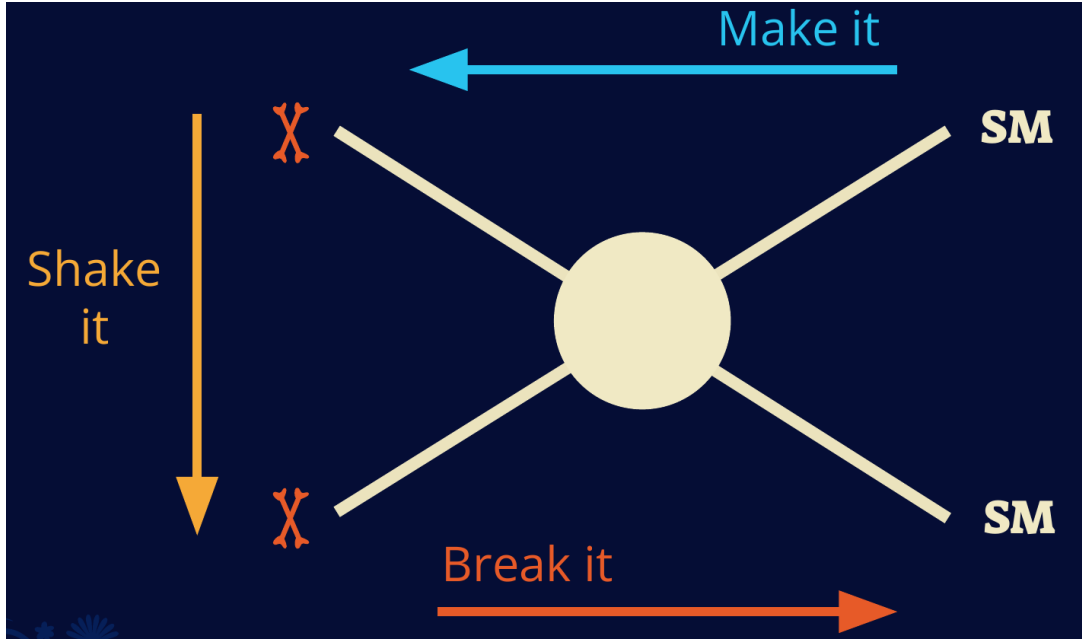


Figure 2.8 Simplified Feynman diagram demonstrating different ways DM can interact with SM particles. The 'X's refer to the DM particles whereas the SM refer to fundamental particles in the SM. The large circle in the center indicates the vertex of interaction and is purposely left vague. The colored arrows refer to different directions of time as well as their respective labels. The arrows indicate the initial and final state of the DM -SM interaction in time.

588 media like the noble gas Xenon. [14]

589 **Make it** refers to the production of DM from SM initial states. The experiment starts with  
 590 particles in the SM. These SM particles are accelerated to incredibly high energies and then collide  
 591 with each other. In the confluence of energy, DM hopefully emerges as a byproduct of the SM  
 592 annihilation. Often it is the collider experiments that are energetic enough to hypothetically produce  
 593 DM. These experiments include the world-wide collaborations ATLAS and CMS at CERN where  
 594 proton collide together at extreme energies. The DM searches, however, are complex. DM likely  
 595 does not interact with the detectors and lives long enough to escape the detection apparatus of  
 596 CERN's colliders. This means any DM production experiment searches for an excess of events  
 597 with missing momentum or energy in the events. An example event with missing transverse  
 598 momentum is shown in Figure 2.9. The missing momentum with no particle tracks implies a  
 599 neutral particle carried the energy out of the detector. However, there are other neutral particles  
 600 in the SM, like neutrons or neutrinos, so any analysis has to account for SM signatures of missing

601 momentum. [15]

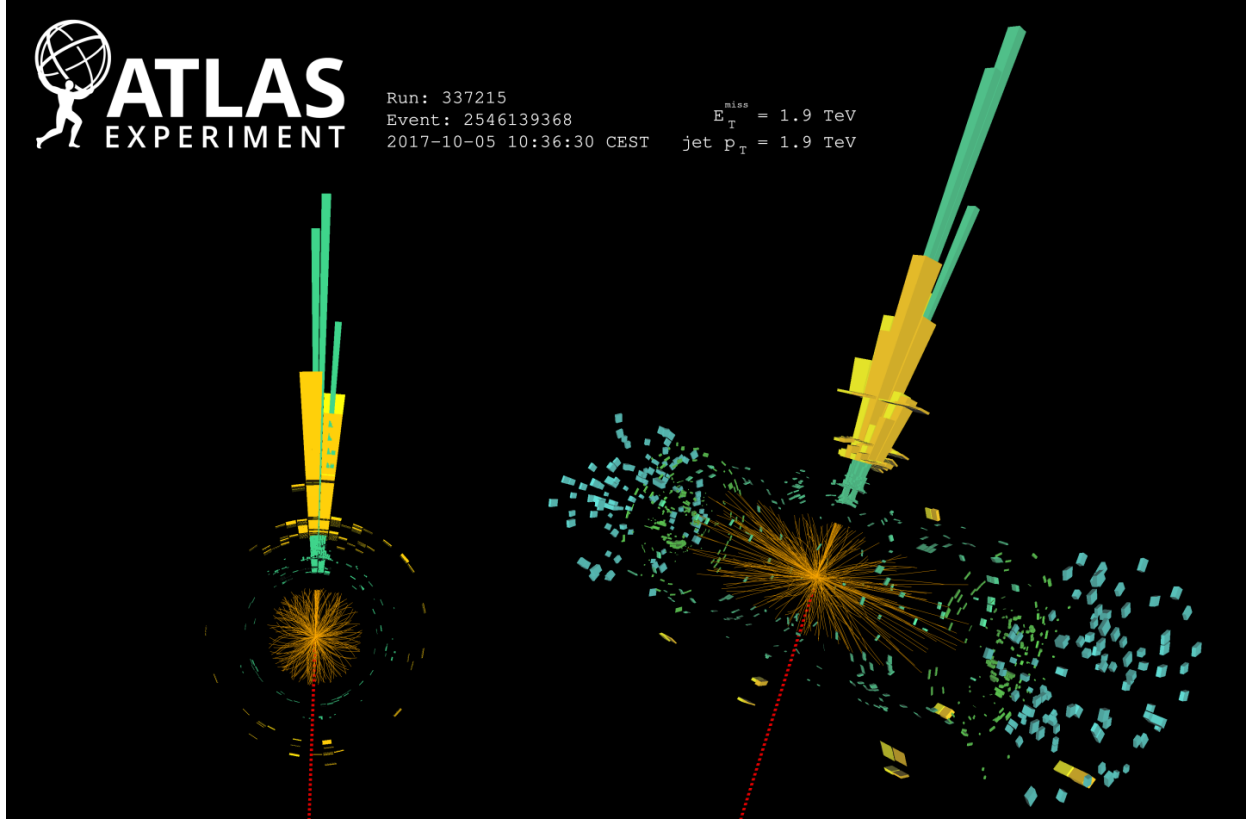


Figure 2.9 A single jet event in ATLAS detector from 2017 [16]. Jet momentum was observed to be 1.9 TeV. Missing transverse momentum was observed to be 1.9 TeV compared to the initial transverse momentum of the event was 0. Implied MET is traced by a red dashed line in event display.

## 602 2.4.2 Break it: Standard Model Signatures of Dark Matter through Indirect Searches

603 **Break it** refers to the creation of SM particles from the dark sector, and it is the primary focus  
604 of this thesis. The interaction begins with DM or in the dark sector. The hypothesis is that this  
605 DM will either annihilate with itself or decay and produce an SM byproduct. This method is  
606 often referred to as the Indirect Detection of DM because we have no lab to directly control or  
607 manipulate the DM. Therefore, most indirect DM searches are performed using observations of  
608 known DM densities among the astrophysical sources. The strength is that we have the whole of the  
609 universe and its 13.6-billion-year lifespan to use as a detector and particle accelerator. Additionally,  
610 locations of dark matter are well cataloged since it was astrophysical observations that presented

611 the problem of DM in the first place.

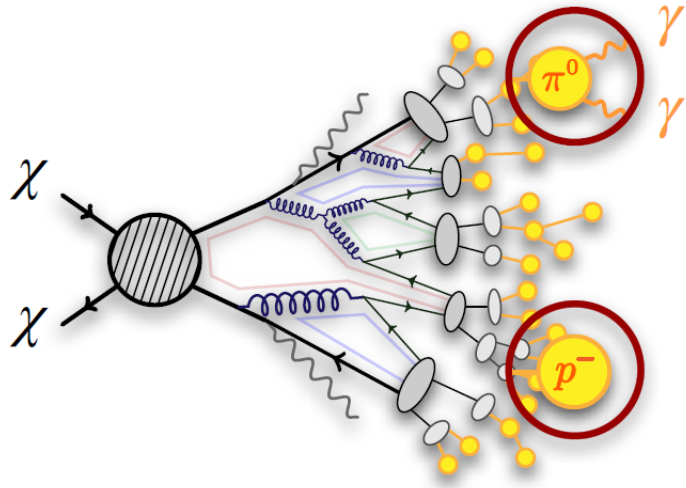


Figure 2.10 More detailed pseudo-Feynman diagram of particle cascade from dark matter annihilation into 2 quarks. The quarks hadronize and down to stable particles like  $\gamma$  or the anti-proton ( $p^-$ ). Diagram pulled from ICRC 2021 presentation on DM annihilation search [17].

612 However, anything can happen in the universe. There are many difficult to deconvolve back-  
613 grounds when searching for DM. One prominent example is the galactic center. We know the  
614 galactic center has a large DM content because of stellar kinematics in our Milky Way and DM halo  
615 simulations. Yet, any signal from the galactic center is challenging to parse apart from the extreme  
616 environment of our supermassive black hole, unresolved sources, and diffuse emission from the  
617 interstellar medium [18]. Despite the challenges, any DM model that yields evidence in the other  
618 two observation methods, **Shake it or Make it** must be corroborated with indirect observations of  
619 the known DM sources. Without corroborating evidence, DM observation in the lab is hard-pressed  
620 to demonstrate that it is the model contributing to the DM seen at the universal scale.

621 In the case of WIMP DM, signals are described in terms of primary SM particles produced  
622 from DM decay or annihilation. The SM initial state particles are then simulated down to stable  
623 final states such as the  $\gamma$ ,  $\nu$ ,  $p$ , or  $e$  which can traverse galactic lengths to reach Earth.

624 Figure 2.10 shows the quagmire of SM particles that emerges from SM initial states that are not  
625 stable [17]. There are many SM particles with varying energies that can be produced in such an

626 interaction. For any arbitrary DM source and stable SM particle, the SM flux from DM annihilating  
 627 to a neutral particle in the SM,  $\phi$ , from a region in the sky is described by the following.

$$\frac{d\Phi_\phi}{dE_\phi} = \frac{\langle\sigma v\rangle}{8\pi m_\chi^2} \frac{dN_\phi}{dE_\phi} \times \int_{\text{source}} d\Omega \int_{l.o.s} \rho_\chi^2 dl(r, \theta') \quad (2.4)$$

628 In Equation (7.1),  $\langle\sigma v\rangle$  is the velocity-weighted annihilation cross-section of DM to the SM.  $m_\chi$   
 629 refers to the mass of DM, noted with Greek letter  $\chi$ .  $\frac{dN_\phi}{dE_\phi}$  is the N particle flux weighted by the  
 630 particle energy. An example is provided in Figure 2.11 for the  $\gamma$  final state. The integrated terms  
 631 are performed over the solid angle,  $d\Omega$ , and line of sight, l.o.s.  $\rho$  is the density of DM for a  
 632 location  $(r, \theta')$  in the sky. The terms left of the ' $\times$ ' are often referred to as the particle physics  
 633 component. The terms on the right are referred to as the astrophysical component. For decaying  
 634 DM, the equation changes to...

$$\frac{d\Phi_\phi}{dE_\phi} = \frac{1}{4\pi\tau m_\chi} \frac{dN_\phi}{dE_\phi} \times \int_{\text{source}} d\Omega \int_{l.o.s} \rho_\chi dl(r, \theta') \quad (2.5)$$

635 In Equation (6.1),  $\tau$  is the decay lifetime of the DM. Just as in Equation (7.1), the left and right  
 636 terms are the particle physics and the astrophysical components respectively. The integrated  
 637 astrophysical component of Equation (7.1) is often called the J-Factor. Whereas the integrated  
 638 astrophysical component of Equation (6.1) is often called the D-Factor.

639     Exact DM  $\text{DM} \rightarrow \text{SM SM}$  branching ratios are not known, so it is usually assumed to go 100%  
 640 into an SM particle/anti-particle. Additionally, when a DM annihilation or decay produces one of  
 641 the neutral, long-lived SM particles ( $\nu$  or  $\gamma$ ), the particle is traced back to a DM source. For DM  
 642 above GeV energies, there are very few SM processes that can produce particles with such a high  
 643 energy. Seeing such a signal would almost certainly be an indication of the presence of dark matter.  
 644 Fortunately, the universe provides us with the largest volume and lifetime ever for a particle physics  
 645 experiment.

## 646 2.5 Sources for Indirect Dark Matter Searches

647     The first detection of DM relied on optical observations. Since then, we have developed new  
 648 techniques to find DM dense regions. As described in Section 2.3.1, many DM dense regions were  
 649 through observing galactic rotation curves. Our Milky Way galaxy is among DM dense regions

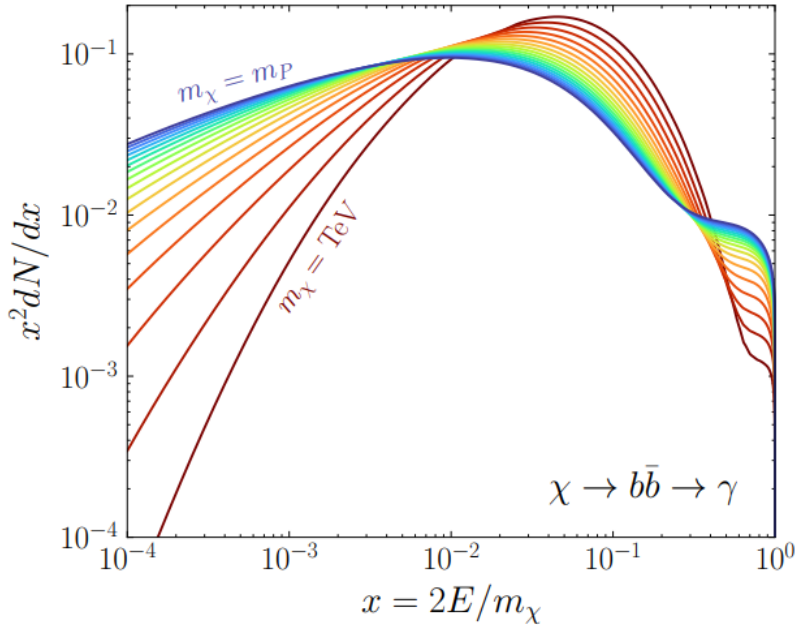


Figure 2.11 Dark Matter (DM) decay spectrum for  $b\bar{b}$  initial state and  $\gamma$  final state. Redder spectra are for larger DM masses. Bluer spectra are light DM masses.  $x$  is a unitless factor defined as the ratio of the mass of DM,  $m_\chi$ , and the final state particle energy  $E_\gamma$ . Figure from [19].

discovered, and it is the largest nearby DM dense region to look at. Additionally, the DM halo surrounding the Milky Way is clumpy [18]. There are regions in the DM halo of the Milky Way that have more DM than others that have captured gas over time. These sub-halos were dense enough collapse gas and form stars. These apparent sub galaxies are known as dwarf spheroidal galaxies and are the main sources studied in this thesis. Each source type comes with different trade-offs. Galactic Center studies will be very sensitive to the assumed distribution of DM. The central DM density can vary substantially as demonstrated in Figure 2.12. At distances close to the center of the galaxy, or small  $r$ , the differences in DM densities can be 3-4 orders of magnitude. Searches toward the galactic center will therefore be quite sensitive to the assumed DM distribution.

Searches toward Dwarf Spheroidal Galaxies (dSph's) suffer from uncertainties in the DM density less than the galactic center studies. This is mostly from their diminutive size being smaller than the angular resolution of most  $\gamma$ -ray observatories [18]. The DM content dSph's are typically determined with the Virial theorem, Equation (2.1), and are usually majority DM [18] in mass. DSph's tend to be ideal sources to look at for DM searches. Their environments are quiet with little

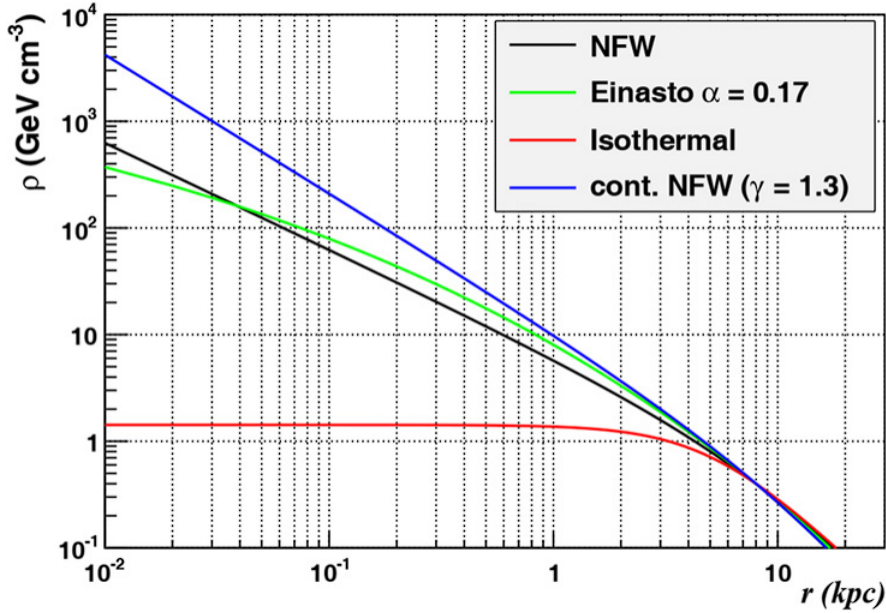


Figure 2.12 Different dark matter density profiles compared. Some models produce exceptionally large densities at small  $r$  [20].

664 astrophysical background. Unlike the galactic center, the most active components of dSph's are the  
 665 stars within them versus a violent accretion disc around a black hole. All this together means that  
 666 dSph's are among the best sources to look at for indirect DM searches. dSph's are the targets of  
 667 focus for this thesis.

## 668 2.6 Multi-Messenger Dark Matter

669 Astrophysics entered a new phase in the past few decades that leverages our increasing sensitivity  
 670 to SM channels and general relativity (GR). Up until the 21st century, astrophysical observations  
 671 were performed with photons ( $\gamma$ ) only. Astrophysics with this 'messenger' is fairly mature now.  
 672 Novel observations of the universe have since only adjusted the sensitivity of the wavelength of  
 673 light that is observed except at MeV energies. Gems like the CMB [10], and more have ultimately  
 674 been observations of different wavelengths of light. Multi-messenger astrophysics proposes using  
 675 other SM particles such the  $p^{+-}$ , or  $\nu$  or gravitation waves predicted by general relativity.

676 The experiment LIGO had a revolutionary discovery in 2016 with the first detection of a binary  
 677 black hole merger [21]. This opened the collective imagination to observing the universe through  
 678 gravitational waves. There has also been a surge of interest in the neutrino ( $\nu$ ) sector. IceCube

679 demonstrated that we are sensitive to neutrinos in regions that correlate with significant photon  
 680 emission like the galactic plane [22]. Neutrinos, like gravitational waves and light, travel mostly  
 681 unimpeded from their source to our observatories. This makes pointing to the originating source  
 682 of these messengers much easier than it is for cosmic rays which are deflected from their source by  
 683 magnetic fields.

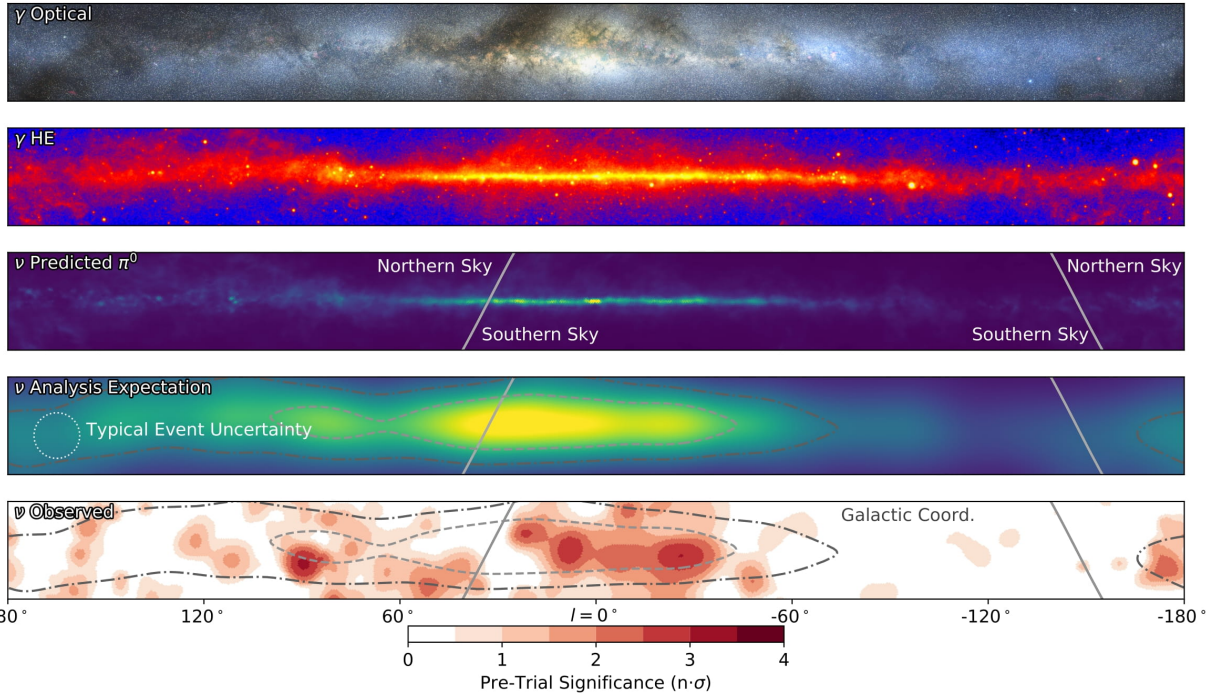


Figure 2.13 The Milky Way Galaxy in photons ( $\gamma$ ) and neutrinos ( $\nu$ ) [22]. The Galactic center is at  $l=0^\circ$  and is the brightest region in all panels. (top) An Optical color image of the Milky Way galaxy seen from Earth. Clouds of gas and dust obscure some light from stars. (2nd down) Integrated flux of  $\gamma$ -rays observed by the Fermi-LAT telescope [23]. (middle) Expected neutrino emission that corresponds with Fermi-LAT observations. (2nd up) Expected neutrino emission profile after considering detector systematics of IceCube. (bottom) Observed neutrino emission from region of the galactic plane. Substantial neutrino emission was detected.

684 The IceCube collaboration recently published a groundbreaking result of the Milky Way in  
 685 neutrinos. The recent result from IceCube, shown in Figure 2.13, proves that we can make  
 686 observations under different messenger regimes. The top two panels show the appearance of the  
 687 galactic plane to different wavelengths of light. Some sources are more apparent in some panels,  
 688 while others are not. This new channel is powerful because neutrinos are readily able to penetrate  
 689 through gas and dust in the Milky Way. This new image also refines our understanding of how high

690 energy particles are produced. For example, the fit to IceCube data prefers neutrino production  
 691 from the decay of  $\pi^0$  [22].

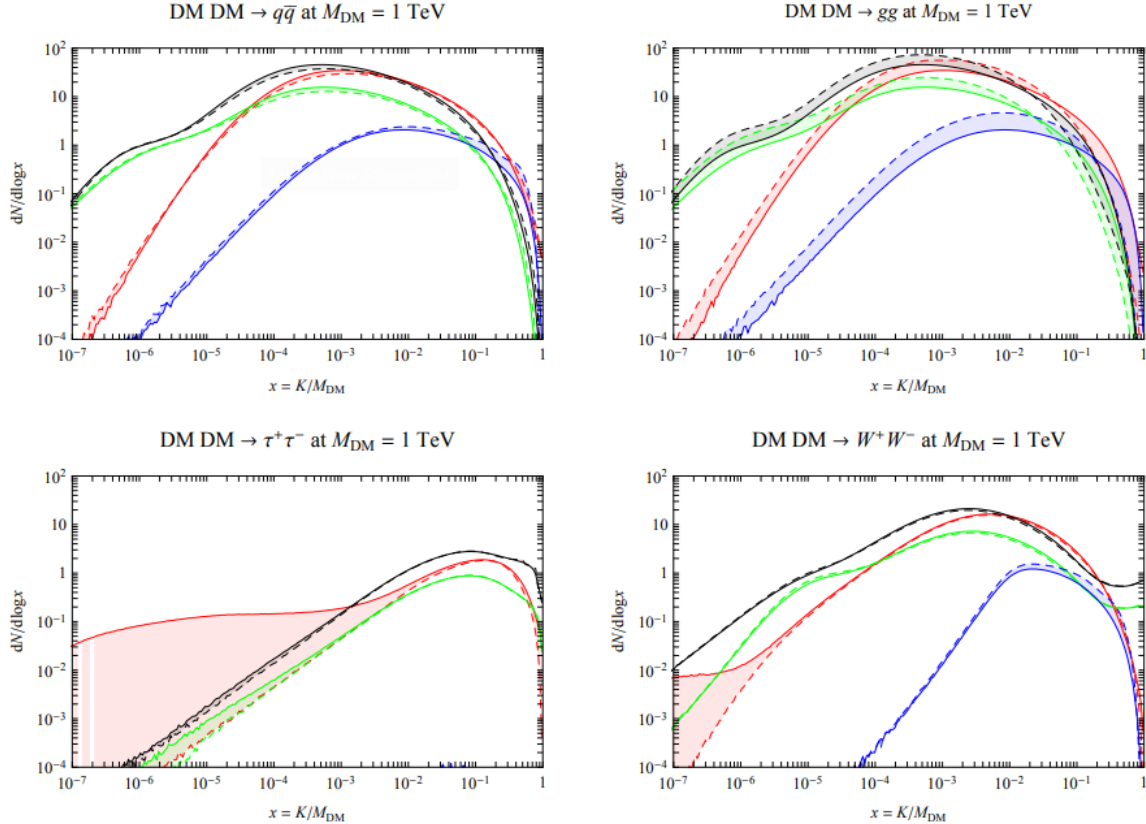


Figure 2.14 Dark Matter annihilation spectra for different final state particle and standard model annihilation channels [24]. Photons (red),  $e^\pm$  (green),  $\bar{p}$  (blue),  $\nu$  (black).

692 Exposing our observations to more cosmic messengers greatly increases our sensitivity to  
 693 rare processes. In the case of DM, Figure 2.14, there are many SM particles produced in DM  
 694 annihilation. Among the final state fluxes are gammas and neutrinos. Charged particles are also  
 695 produced however they would not likely make it to Earth since they will be deflected by magnetic  
 696 fields between the source and Earth. This means observatories that can see the neutral messengers  
 697 are especially good for DM searches and for combining data for a multi-messenger DM search.

## CHAPTER 3

698                   **HIGH ALTITUDE WATER CHERENKOV (HAWC) OBSERVATORY**

699   **3.1 The Detector**

700   **3.2 Events Reconstruction and Data Acquisition**

701   **3.2.1 G/H Discrimination**

702   **3.2.2 Angle**

703   **3.2.3 Energy**

704   **3.3 Remote Monitoring**

705   **3.3.1 ATHENA Database**

706   **3.3.2 HOMER**

707

## CHAPTER 4

### ICECUBE NEUTRINO OBSERVATORY

708 **4.1 The Detector**

709 **4.2 Events Reconstruction and Data Acquisition**

710 **4.2.1 Angle**

711 **4.2.2 Energy**

712 **4.3 Northern Test Site**

713 **4.3.1 PIgeon remote dark rate testing**

714 **4.3.2 Bulkhead Construction**

## CHAPTER 5

### GLORY DUCK: MULTI-WAVELENGTH SEARCH FOR DARK MATTTER ANNIHILATION TOWARDS DWARF SPHEROIDAL GALAXIES

#### 5.1 Introduction

The field of astrophysics now has several instruments and observatories sensitive to high energy gamma-rays. The energy sensitivity for the modern gamma-ray program spans many orders of magnitude. Figure 5.1 demonstrates these similar sensitivities across energies for the five experiments: Fermi-LAT, HAWC, HESS, MAGIC, and VERITAS.

Each of the five experiments featured in Figure 5.1 have independently searched for DM annihilation from dwarf spheroidal galaxies (dSph) and set limits. Intriguingly, there are regions of substantial overlap in their energy sensitivities. This clearly motivates an analysis that combines data from these five. Each experiment has unique gamma-ray detection methods and their weaknesses and strengths can be leveraged with each other. The HAWC gamma-ray observatory is extensively introduced in chapter 3, so it is not introduced here. A brief description of the remaining experiments are in the following paragraphs.

The Large Area Telescope (LAT) is a pair conversion telescope mounted on the NASA Fermi satellite in orbit  $\sim$ 550 km above the Earth [26]. LAT's field of view covers about 20% of the whole sky, and it sweeps the whole sky approximately every 3 hours. LAT's gamma-ray energy sensitivity ranges from 20 MeV up to 1 TeV. Previous DM searches towards dSphs using Fermi-LAT are published in [27] and [28]

The High Energy Spectroscopic System (HESS), Major Atmospheric Gamma Imaging Cherenkov (MAGIC), and Very Energetic Radiation Imaging Telescope Array System (VERITAS) are arrays of Imaging Atmospheric Cherenkov Telescopes (IACT). These telescopes observe the Cherenkov light emitted from gamma-ray showers in the Earth's atmosphere. The field of view for these telescopes is no larger than  $5^\circ$  with energy sensitivities ranging from 30 GeV up to 100 TeV [29, 30, 31]. IACTs are able to make precise observations in selected regions of the sky, however can only be operated in ideal dark conditions. HESS's observations of the dwarves

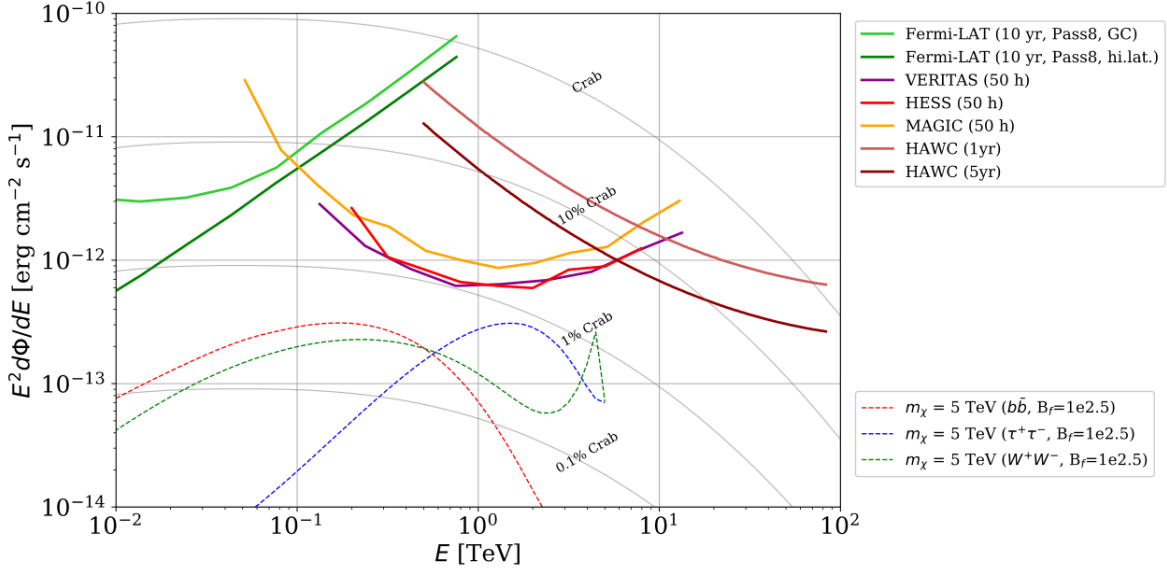


Figure 5.1 Sensitivities of five gamma-ray experiments compared to percentages of the Crab nebula’s emission and dark matter annihilation. Solid lines present estimated sensitivities to power law spectra [FACT CHECK THIS] for each experiment. Green lines are Fermi-LAT sensitivities where lighter green is the sensitivity to the galactic center and dark green is its sensitivity to higher declinations. Orange, red, and purple solid lines represent the MAGIC, HESS, and VERITAS 50 hour sensitivities respectively. The maroon and brown lines are the HAWC 1 year and 5 year sensitivities. Across four decades of gamma-ray energy, these experiments have similar sensitivities on the order  $10^{-12}$  erg  $\text{cm}^{-2}\text{s}^{-1}$ . The dotted lines are estimated dark matter fluxes assuming  $m_\chi = 5$  TeV DM annihilating to bottom quarks (red), tau leptons (blue), and W bosons (green). Faded gray lines outline percentage flux of the Crab nebula. Figure is an augmented version of [25]

741 Sculptor and Carina were between January 2008 and December 2009. HESS’s observations of  
 742 Coma Berenices were from 2010 to 2013, and Fornax was observed in 2010 [32, 33, 34]. MAGIC  
 743 provided deep observations of Segue1 between 2011 and 2013 [35]. MAGIC also provides data  
 744 for three dwarves: Coma Berenices, Draco, and Ursa Major II where observations were made  
 745 in: January - June 2019 [36], March - September 2018 [36], and 2014 - 2016 [37] respectively.  
 746 VERITAS provided data for Boötes I, Draco, Segue 1, and Ursa Minor from 2009 to 2016 [38].

747 This chapter presents the Glory Duck analysis, the name given for the search for dark matter  
 748 annihilation from dSph by combining data from the five gamma-ray observatories: Fermi-LAT,  
 749 HAWC, HESS, MAGIC, and VERITAS. Specifically, the methods in analysis and modeling are  
 750 presented for the HAWC gamma-ray observatory. This work was published to the Journal of  
 751 Cosmology and Astroparticle Physics and presented at the International Cosmic Ray Conference

752 in 2019, 2021, and 2023 [39, 40, 41] and others.

753 **5.2 Dataset and Background**

754 This section enumerates the data and background methods used for HAWC's study of dSphs.

755 Section 5.2.1 and Section 5.2.2 are most useful for fellow HAWC collaborators looking to replicate

756 the Glory Duck analysis.

757 **5.2.1 Itemized HAWC files**

758 • Detector Resolution: `response_aerie_svn_27754_systematics_best_mc_test_no`  
759 `broadpulse\_10pctlogchargesmearing_0.63qe_25kHzNoise_run5481_curvatu`  
760 `re0_index3.root`

761 • Data Map: `maps-20180119/liff/maptree_1024.root`

762 • Spectral Dictionary: `DM_CirrelliSpectrum_dict_gammas.npy`

763 • Analysis wiki: [https://private.hawc-observatory.org/wiki/index.php/Glory\\_Duck\\_Multi-Experiment\\_Dark\\_Matter\\_Search](https://private.hawc-observatory.org/wiki/index.php/Glory_Duck_Multi-Experiment_Dark_Matter_Search)

765 **5.2.2 Software Tools and Development**

766 This analysis was performed using HAL and 3ML [42, 43] in Python version 2. I built software  
767 to implement the *A Poor Particle Physicist Cookbook for Dark Matter Indirect Detection* (PPPC)  
768 [44] DM spectral model and dSphs spatial model from [45] for HAWC analysis. A NumPy version  
769 of this dictionary was made for both Py2 and Py3. The code base for creating this dictionary is  
770 linked on my GitLab sandbox:

771 • Py2: [Dictionary Generator \(Deprecated\)](#)

772 • Py3: [PPPC2Dict](#)

773 The analysis was performed using the  $f_{\text{hit}}$  framework performed in the HAWC Crab paper  
774 [42]. The Python2 NumPy dictionary file for gamma-ray final states is `dmCirSpecDict.npy`. The  
775 corresponding Python3 file is `DM_CirrelliSpectrum_dict_gammas.npy`. These files can also

776 be used for decay channels and the PPPC describes how [44]. All other software used for data  
777 analysis, DM profile generation, and job submission to SLURM are also kept in my sandbox for  
778 [the Glory Duck](#) project.

779 **5.2.3 Data Set and Background Description**

780 The HAWC data maps used for this analysis contain 1017 days of data between runs 2104  
781 (2014-11-26) and 7476 (2017-12-20). They were generated from pass 4.0 reconstruction. The  
782 analysis is performed using the  $f_{hit}$  energy binning scheme with bins (1-9) similar to what was done  
783 for the Crab and previous HAWC dSph analysis [42, 46]. Bin 0 was excluded as it has substantial  
784 hadronic contamination and poor angular resolution.

785 This analysis was done on dSphs because of their large DM mass content relative to baryonic  
786 mass. We consider the following to estimate the background to this study.

- 787 • The dSphs are small in HAWC’s field of view, so the analysis is not sensitive to large or small  
788 scale anisotropies.
- 789 • The dSphs used in this analysis are off the galactic plane.
- 790 • The dSphs are baryonically faint relative to their expected dark matter content and are not  
791 expected to contain high energy gamma-ray sources.

792 Therefor we make no additional assumptions on the background from our sources and use  
793 HAWC’s standard direct integration method for background estimation [42]. It is possible for  
794 gamma rays from DM annihilation to scatter in transit to HAWC via Inverse Compton Scattering  
795 (ICS). This was investigated and its impact on the flux is basically zero. Supporting information  
796 on this is in Section 5.7.1

797 **5.3 Analysis**

798 The expected differential photon flux from DM-DM annihilation to standard model particles,  
799  $d\Phi_\gamma/dE_\gamma$ , over solid angle,  $\Omega$  is described by the familiar equation.

$$\frac{d\Phi_\gamma}{dE_\gamma} = \frac{\langle\sigma v\rangle}{8\pi m_\chi^2} \frac{dN_\gamma}{dE_\gamma} \times \int_{\text{source}} d\Omega \int_{l.o.s} \rho_\chi^2 dl(r, \theta') \quad (5.1)$$

800 Where  $\langle \sigma v \rangle$  is the velocity weighted annihilation cross-section.  $\frac{dN}{dE}$  is the expected differential  
 801 number of photons produced at each energy per annihilation.  $m_\chi$  is the rest mass of the supposed  
 802 DM particle.  $\rho_\chi$  is the DM density.  $J$  is the astrophysical J-factor and is defined as

$$J = \int d\Omega \int_{l.o.s} dl \rho_\chi^2(r, \theta') \quad (5.2)$$

803  $l$  is the distance to the source from Earth.  $r$  is the radial distance from the center of the source.  $\theta'$  is  
 804 the half angle defining a cone containing the DM source. How each component is synthesized and  
 805 considered for HAWC's analysis is presented in the following sections. Section 5.3.1 presents the  
 806 particle physics model for DM annihilation. Section 5.3.2 presents the spatial distributions built  
 807 for each dSph.

808 **5.3.1  $\frac{dN_\gamma}{dE_\gamma}$  - Particle Physics Component**

809 For these spectra, we import the PPPC with Electroweak (EW) corrections [44]. The spectrum  
 810 is implemented as a model script in astromodels for 3ML. The EW corrections were previously not  
 811 considered for HAWC and are significant for DM annihilating to EW coupled SM particles such  
 812 as all leptons, and the  $\gamma$ ,  $Z$ , and  $W$  bosons [46]. Figure 5.2 demonstrates the significance of EW  
 813 corrections for W boson annihilation. Across EW SM channels, the gamma-ray spectra become  
 814 harder than spectra without EW corrections. Tables from the PPPC were reformatted into Python  
 815 NumPy dictionaries for collaboration-wide use. A class in astromodels was developed to include  
 816 the EW correction from the PPPC and is aptly named `PPPCSpectra` within `DM_models.py`.

817 **5.3.2  $J$ - Astrophysical Component**

818 The J-factor profiles for each source are imported from Geringer-Sameth (referred to with  $\mathcal{GS}$ )  
 819 [45]. These were pulled from the publication as  $J(\theta)$ , where  $\theta$  is the angular separation from the  
 820 center of the source. HAWC requires maps in terms of  $\frac{dJ}{d\Omega}$ , so the conversion from the maps was  
 821 done in the following way...

822 First, convert the angular distances to solid angles

$$\Omega = 2 \cdot \pi(1 - \cos(\theta)) \quad (5.3)$$

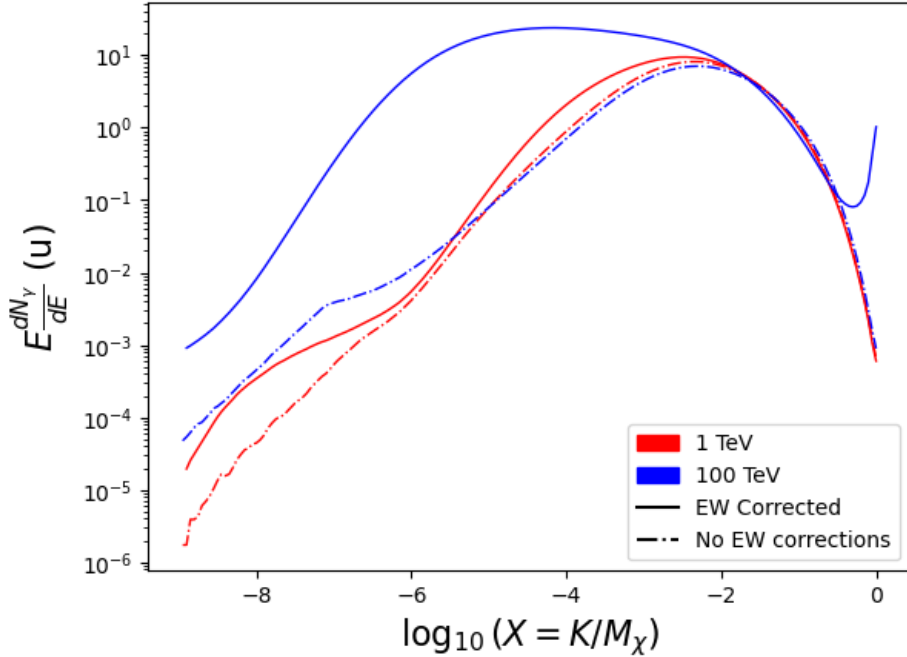


Figure 5.2 Effect of Electroweak (EW) corrections on expected DM annihilation spectrum for  $\chi\chi \rightarrow W^-W^+$ . Solid lines are spectral models that consider EW corrections. Dash-dot lines are spectral models without EW corrections. Red lines are models for  $M_\chi = 1$  TeV. Blue lines represent models for  $M_\chi = 100$  TeV. All models are sourced from the PPPC4DMID [44].

which reduces with a small angle approximation to  $\pi\theta^2$ . Next, the central difference for both the  $\Delta J$  and  $\Delta\Omega$  value were calculated from the discretized  $J(\theta)$  with the central difference stencil:

$$\Delta\phi_i = \phi_{i+1} - \phi_{i-1} \quad (5.4)$$

Where  $\phi$  is either  $\Omega$  or  $J$ . These were done separately in case the grid spacing in  $\theta$  was not uniform. Finally, these lists are divided so that we are left with an approximation of the  $dJ/d\Omega$  profile that is a function of  $\theta$ . Admittedly, this is an approximation method for the map which introduces small errors compared to the true profile estimate. This was checked as a systematic against the author's profiling of the spatial distribution and is documented in Section 5.8.1.

With  $\frac{dJ}{d\Omega}(\theta)$ , a map is generated, first by filling in the north-east quadrant of the map. This quadrant is then reflected twice, vertically then horizontally, to fill the full map. Maps are then normalized by dividing the discrete 2D integral of the map. The 2D integral was a simple height

833 of bins, Newton's integral:

$$p^2 \cdot \sum_{i,j=0}^{N,M} \frac{dJ}{d\Omega}(\theta_{i,j}, \phi_{i,j}) \quad (5.5)$$

834 These maps are HEALpix maps with NSIDE 16384 and saved in the `.fits` format.

835 Another DM spatial distribution model from Bonnivard ( $\mathcal{B}$ ) [47] was used for the Glory Duck  
836 study. However, to save computational time, limits from  $\mathcal{GS}$  were scaled to  $\mathcal{B}$  instead of each  
837 experiment performing a full study a second time. How these models compare is demonstrated  
838 for each dSph in Figure 5.16 and Figure 5.17 Plots of these maps are provided for each source  
839 in chapter A Examples of the two most impactful dSphs derived from  $\mathcal{GS}$ , Segue1 and Coma  
840 Berenices are featured in Figure 5.3

### 841 5.3.3 Source Selection and Annihilation Channels

842 We use many of the dSphs presented in HAWC's previous dSph DM search [46]. HAWC's  
843 sources for Glory Duck include Boötes I, Coma Berenices, Canes Venatici I + II, Draco, Hercules,  
844 Leo I, II, + IV, Segue 1, Sextans, and Ursa Major I + II. A full description of all sources used  
845 in Glory Duck is found in Table 5.1. Triangulum II was excluded from the Glory Duck analysis  
846 because of large uncertainties in its  $J$  factor. Ursa Minor was excluded from HAWC's contribution  
847 to the combination because the source extension model extended Ursa Minor beyond HAWC's field  
848 of view. Ursa Minor was not expected to contribute significantly to the combined limit, so work  
849 was not invested in a solution to include Ursa Minor.

850 This analysis improves on the previous HAWC dSph paper [46] in the following ways. Pre-  
851 viously, the dSphs were treated and implemented as point sources. For this analysis, dSphs are  
852 modeled and treated as extended source. The impact of this change with respect to the upper limit  
853 is source dependent and is explored in Section 5.7.2. Previously, the particle physics model used for  
854 gamma-ray spectra from DM annihilation did not have EW corrections where the PPPC includes  
855 them. Finally, the gamma-ray ray dataset is much larger. The study performed here analyzes over  
856 1000 days of data compared to 507.

857 The SM annihilation channels probed for the Glory Duck combination include  $b\bar{b}$ ,  $e\bar{e}$ ,  $\mu\bar{\mu}$ ,  $\tau\bar{\tau}$ ,  
858  $t\bar{t}$ ,  $W^+W^-$ , and  $ZZ$ . A summary of all sources, with a description of each experiments' sensitivity

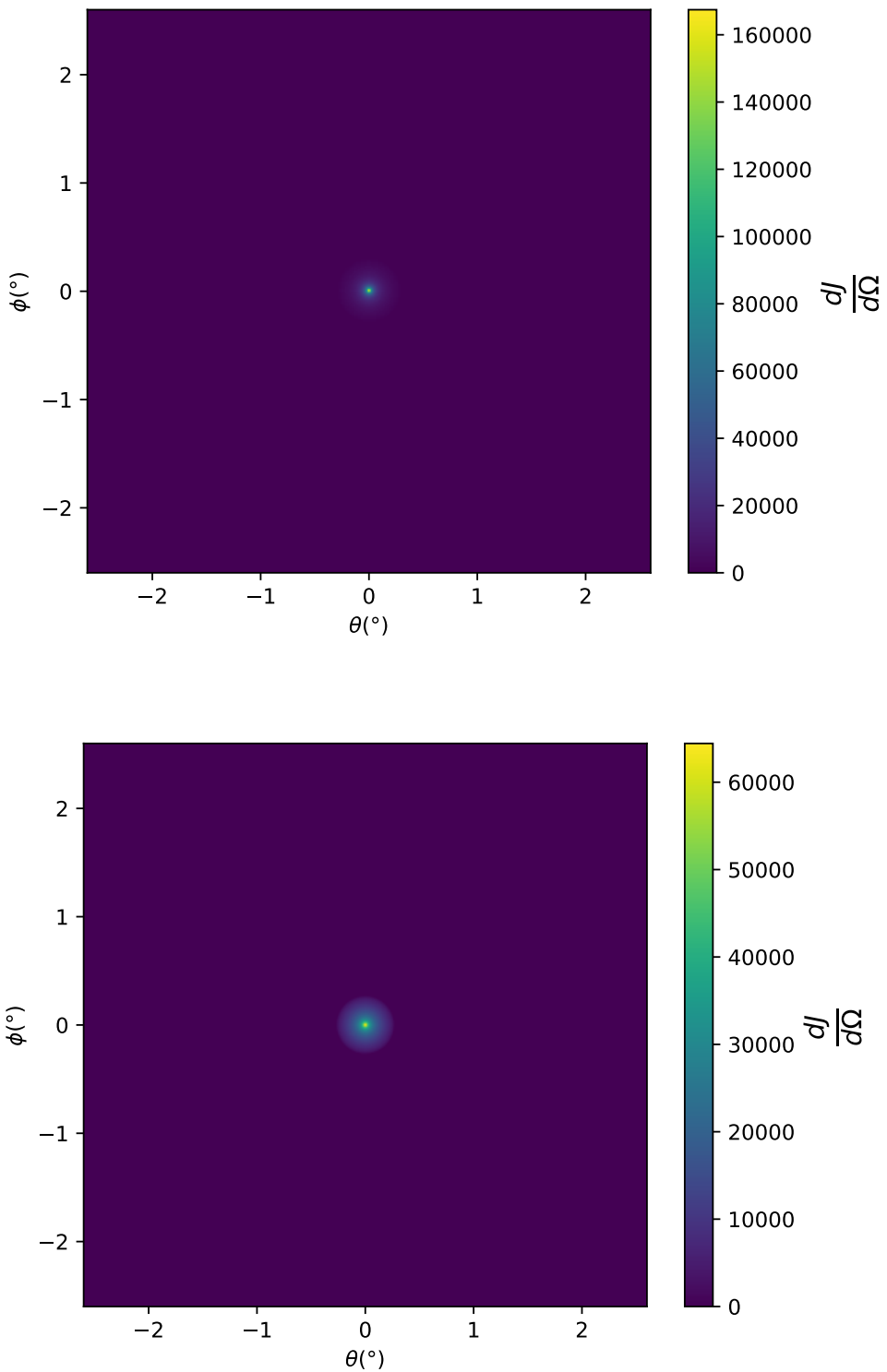


Figure 5.3  $\frac{dJ}{d\Omega}$  maps for Segue1 (top) and Coma Berenices (bottom). Origin is centered on the specific dwarf spheroidal galaxies (dSph). X and Y axes are the angular separation from the center of the dwarf. Plots of the remaining 11 dSph HAWC studied are linked in Fig. A.1.

Table 5.1 Summary of the relevant properties of the dSphs used in the present work. Column 1 lists the dSphs. Columns 2 and 3 present their heliocentric distance and galactic coordinates, respectively. Columns 4 and 5 report the  $J$ -factors of each source given from the  $\mathcal{GS}$  and  $\mathcal{B}$  independent studies and their estimated  $\pm 1\sigma$  uncertainties. The values  $\log_{10} J$  ( $\mathcal{GS}$  set) [45] correspond to the mean  $J$ -factor values for a source extension truncated at the outermost observed star. The values  $\log_{10} J$  ( $\mathcal{B}$  set) [47] are provided for a source extension at the tidal radius of each dSph. **Bolded sources are within HAWC’s field of view and provided to the Glory Duck analysis.**

Name	Distance (kpc)	$l, b$ ( $^{\circ}$ )	$\log_{10} J$ ( $\mathcal{GS}$ set) $\log_{10}(\text{GeV}^2 \text{cm}^{-5} \text{sr})$	$\log_{10} J$ ( $\mathcal{B}$ set) $\log_{10}(\text{GeV}^2 \text{cm}^{-5} \text{sr})$
<b>Boötes I</b>	66	358.08, 69.62	$18.24^{+0.40}_{-0.37}$	$18.85^{+1.10}_{-0.61}$
<b>Canes Venatici I</b>	218	74.31, 79.82	$17.44^{+0.37}_{-0.28}$	$17.63^{+0.50}_{-0.20}$
<b>Canes Venatici II</b>	160	113.58, 82.70	$17.65^{+0.45}_{-0.43}$	$18.67^{+1.54}_{-0.97}$
Carina	105	260.11, -22.22	$17.92^{+0.19}_{-0.11}$	$18.02^{+0.36}_{-0.15}$
<b>Coma Berenices</b>	44	241.89, 83.61	$19.02^{+0.37}_{-0.41}$	$20.13^{+1.56}_{-1.08}$
<b>Draco</b>	76	86.37, 34.72	$19.05^{+0.22}_{-0.21}$	$19.42^{+0.92}_{-0.47}$
Fornax	147	237.10, -65.65	$17.84^{+0.11}_{-0.06}$	$17.85^{+0.11}_{-0.08}$
<b>Hercules</b>	132	28.73, 36.87	$16.86^{+0.74}_{-0.68}$	$17.70^{+1.08}_{-0.73}$
<b>Leo I</b>	254	225.99, 49.11	$17.84^{+0.20}_{-0.16}$	$17.93^{+0.65}_{-0.25}$
<b>Leo II</b>	233	220.17, 67.23	$17.97^{+0.20}_{-0.18}$	$18.11^{+0.71}_{-0.25}$
<b>Leo IV</b>	154	265.44, 56.51	$16.32^{+1.06}_{-1.70}$	$16.36^{+1.44}_{-1.65}$
Leo V	178	261.86, 58.54	$16.37^{+0.94}_{-0.87}$	$16.30^{+1.33}_{-1.16}$
Leo T	417	214.85, 43.66	$17.11^{+0.44}_{-0.39}$	$17.67^{+1.01}_{-0.56}$
Sculptor	86	287.53, -83.16	$18.57^{+0.07}_{-0.05}$	$18.63^{+0.14}_{-0.08}$
<b>Segue I</b>	23	220.48, 50.43	$19.36^{+0.32}_{-0.35}$	$17.52^{+2.54}_{-2.65}$
Segue II	35	149.43, -38.14	$16.21^{+1.06}_{-0.98}$	$19.50^{+1.82}_{-1.48}$
<b>Sextans</b>	86	243.50, 42.27	$17.92^{+0.35}_{-0.29}$	$18.04^{+0.50}_{-0.28}$
<b>Ursa Major I</b>	97	159.43, 54.41	$17.87^{+0.56}_{-0.33}$	$18.84^{+0.97}_{-0.43}$
<b>Ursa Major II</b>	32	152.46, 37.44	$19.42^{+0.44}_{-0.42}$	$20.60^{+1.46}_{-0.95}$
Ursa Minor	76	104.97, 44.80	$18.95^{+0.26}_{-0.18}$	$19.08^{+0.21}_{-0.13}$

859 to the source, is provided in Table 5.2.

## 860 5.4 Likelihood Methods

### 861 5.4.1 HAWC Likelihoods

862 For every analysis bin in energy,  $f_{hit}$  bins (1-9), and location, we can expect  $N$  signal events and  
863  $B$  background events. The expected number of excess signal events from dark matter annihilation,

Table 5.2 Summary of dSph observations by each experiment used in this work. A ‘-’ indicates the experiment did not observe the dSph for this study. For Fermi-LAT, the exposure at 1 GeV is given. For HAWC,  $|\Delta\theta|$  is the absolute difference between the source declination and HAWC latitude. HAWC is more sensitive to sources with smaller  $|\Delta\theta|$ . For IACTs, we show the zenith angle range, the total exposure, the energy range, the angular radius  $\theta$  of the signal or ON region, the ratio of exposures between the background-control (OFF) and signal (ON) regions ( $\tau$ ), and the significance of gamma-ray excess in standard deviations,  $\sigma$ .

Source name	Fermi-LAT	HAWC	H.E.S.S, MAGIC, VERITAS						
	Exposure ( $10^{11}$ s m $^2$ )	$ \Delta\theta $ (°)	IACT	Zenith (°)	Exposure (h)	Energy range (GeV)	$\theta$ (°)	$\tau$	$S$ ( $\sigma$ )
Boötes I	2.6	4.5	VERITAS	15 – 30	14.0	100–41000	0.10	8.6	-1.0
Canes Venatici I	2.9	14.6	–	–	–	–	–	–	–
Canes Venatici II	2.9	15.3	–	–	–	–	–	–	–
Carina	3.1	–	H.E.S.S.	27 – 46	23.7	310 – 70000	0.10	18.0	-0.3
Coma Berenices	2.7	4.9	H.E.S.S.	47 – 49	11.4	550 – 70000	0.10	14.4	-0.4
			MAGIC	5 – 37	49.5	60 – 10000	0.17	1.0	–
			MAGIC	29 – 45	52.1	70 – 10000	0.22	1.0	–
Draco	3.8	38.1	VERITAS	25 – 40	49.8	120 – 70000	0.10	9.0	-1.0
Fornax	2.7	–	H.E.S.S.	11 – 25	6.8	230 – 70000	0.10	45.5	-1.5
Hercules	2.8	6.3	–	–	–	–	–	–	–
Leo I	2.5	6.7	–	–	–	–	–	–	–
Leo II	2.6	3.1	–	–	–	–	–	–	–
Leo IV	2.4	19.5	–	–	–	–	–	–	–
Leo V	2.4	–	–	–	–	–	–	–	–
Leo T	2.6	–	–	–	–	–	–	–	–
Sculptor	2.7	–	H.E.S.S.	10 – 46	11.8	200 – 70000	0.10	19.8	-2.2
Segue I	2.5	2.9	MAGIC	13 – 37	158.0	60 – 10000	0.12	1.0	-0.5
			VERITAS	15 – 35	92.0	80 – 50000	0.10	7.6	0.7
Segue II	2.7	–	–	–	–	–	–	–	–
Sextans	2.4	20.6	–	–	–	–	–	–	–
Ursa Major I	3.4	32.9	–	–	–	–	–	–	–
Ursa Major II	4.0	44.1	MAGIC	35 – 45	94.8	120 – 10000	0.30	1.0	-2.1
Ursa Minor	4.1	–	VERITAS	35 – 45	60.4	160 – 93000	0.10	8.4	-0.1

864  $S$ , is estimated by convolving Equation (7.1) with HAWC's energy response and pixel point spread  
 865 functions. I then compute the test statistic (TS) with the log-likelihood ratio test,

$$\text{TS} = -2 \ln \left( \frac{\mathcal{L}_0}{\mathcal{L}^{\max}} \right) \quad (5.6)$$

867 where  $\mathcal{L}_0$  is the null hypothesis, or no DM emission, likelihood.  $\mathcal{L}^{\max}$  is the best fit signal  
 868 hypothesis where  $\langle \sigma v \rangle$  maximizes the likelihood. We calculate the likelihood of each source and  
 869 model, assuming events are Poisson distributed, with

$$\mathcal{L} = \prod_i \frac{(B_i + S_i)^{N_i} e^{-(B_i + S_i)}}{N_i!} \quad (5.7)$$

870 where  $S_i$  is the sum of expected number of signal counts.  $B_i$  is the number of background counts  
 871 observed.  $N_i$  is the total number of counts.

872 I also calculate an upper limit on  $\langle \sigma v \rangle$  by calculating the 95% confidence level (CL). For the  
 873 CL, we define a parameter,  $\text{TS}_{95}$ , as

$$\text{TS}_{95} \equiv \sum_{\text{bins}} \left[ 2N \ln \left( 1 + \frac{\epsilon S_{\text{ref}}}{B} \right) - 2\epsilon S_{\text{ref}} \right] \quad (5.8)$$

874 where the expected signal counts from a dSph is scaled by  $\epsilon$ .  $S_{\text{ref}}$  is the expected number of excess  
 875 counts in a bin from DM emission from a dSph with a corresponding annihilation cross-section,  
 876  $\langle \sigma v \rangle$ . We scan  $\epsilon$  such that

$$2.71 = \text{TS}_{\max} - \text{TS}_{95} \quad (5.9)$$

#### 877 5.4.2 Glory Duck Joint Likelihood

878 The joint likelihood for the 5-experiment combination was done similarly as Section 5.4.1. We  
 879 calculate upper limits on  $\langle \sigma v \rangle$  from the TS, Eq. (5.6), and define the likelihood ratio more generally

$$\lambda(\langle \sigma v \rangle | \mathcal{D}_{\text{dSphs}}) = \frac{\mathcal{L}(\langle \sigma v \rangle; \hat{\nu} | \mathcal{D}_{\text{dSphs}})}{\mathcal{L}(\widehat{\langle \sigma v \rangle}; \hat{\nu} | \mathcal{D}_{\text{dSphs}})} \quad (5.10)$$

880  $\mathcal{D}_{\text{dSphs}}$  is the totality of observations across experiments and dSphs.  $\nu$  are the nuisance parameters  
 881 which are the  $J$  factors in this study.  $\widehat{\langle \sigma v \rangle}$  and  $\hat{\nu}$  are the respective estimate that maximize  $\mathcal{L}$   
 882 globally. Finally,  $\hat{\nu}$  is the set of nuisance parameters that maximize  $\mathcal{L}$  for a fixed value of  $\langle \sigma v \rangle$ .

883 The *complete* joint likelihood,  $\mathcal{L}$  that encompasses all observations from all instruments and  
 884 dSphs can be factorized into *partial* functions for each dSph  $l$  (with  $\mathcal{L}_{\text{dSph},l}$ ) and its  $J$  factor ( $\mathcal{J}_l$ ):

$$\mathcal{L}(\langle\sigma v\rangle; \nu | \mathcal{D}_{\text{dSphs}}) = \prod_{l=1}^{N_{\text{dSphs}}} \mathcal{L}_{\text{dSph},l}(\langle\sigma v\rangle; J_l, \nu_l | \mathcal{D}_l) \times \mathcal{J}_l(J_l | J_{l,\text{obs}}, \sigma_{\log J_l}). \quad (5.11)$$

885 For this study,  $N_{\text{dSphs}} = 20$  is the number of dSphs studied.  $\mathcal{D}_l$  are the gamma-ray observations  
 886 of dSph,  $l$ .  $\nu_l$  are the nuisance parameters modifying the gamma-ray observations of dSph,  $l$ ,  
 887 but excludes  $\mathcal{J}_l$ .  $\mathcal{J}_l$  is the  $J$  factor for dSph,  $l$ , as defined in Equation (5.2), and it is a nuisance  
 888 parameter whose value is unknown.  $\log_{10} J_{l,\text{obs}}$  and  $\sigma_{\log J_l}$  are obtained from fitting a log-normal  
 889 function of  $J_{l,\text{obs}}$  to the posterior distribution of  $J_l$  [48].  $\log_{10} J_{l,\text{obs}}$  and  $\sigma_{\log J_l}$  values are provided  
 890 in Table 5.1. The term  $\mathcal{J}_l$  constraining  $J_l$  is written as:

$$\mathcal{J}_l(J_l | J_{l,\text{obs}}, \sigma_{\log J_l}) = \frac{1}{\ln(10)J_{l,\text{obs}}\sqrt{2\pi}\sigma_{\log J_l}} \exp\left(-\frac{(\log_{10} J_l - \log_{10} J_{l,\text{obs}})^2}{2\sigma_{\log J_l}^2}\right). \quad (5.12)$$

891 Both the  $\mathcal{GS}$  and  $\mathcal{B}$ , displayed in Table 5.1, sets of  $J$  factors are used in this analysis. Equation (5.12)  
 892 is also normalized, so it can also be interpreted as a probability density function (PDF) for  $J_{l,\text{obs}}$ .  
 893 From Equation (7.1), we can also see that  $\langle\sigma v\rangle$  and  $J_l$  are degenerate when computing  $\mathcal{L}_{\text{dSph},l}$ .  
 894 Therefore, as noted in [49], it is sufficient to compute  $\mathcal{L}_{\text{dSph},l}$  versus  $\langle\sigma v\rangle$  for a fixed value of  $J_l$ .  
 895 We used  $J_{l,\text{obs}}(\mathcal{GS})$  reported in Tab. 5.1, in order to perform the profile of  $\mathcal{L}$  with respect to  $J_l$ .  
 896 The degeneracy implies that for any  $J'_l \neq J_{l,\text{obs}}$  (in practice in our case we used  $J'_l = J_{l,\text{obs}}(\mathcal{B})$  to  
 897 compute results from a different set of  $J$  factors):

$$\mathcal{L}_{\text{dSph},l}(\langle\sigma v\rangle; J'_l, \nu_l | \mathcal{D}_l) = \mathcal{L}_{\text{dSph},l}\left(\frac{J'_l}{J_{l,\text{obs}}}\langle\sigma v\rangle; J_{l,\text{obs}}, \nu_l | \mathcal{D}_l\right), \quad (5.13)$$

898 which is a straightforward rescaling operation that reduces the computational needs of the profiling  
 899 operation since:

$$\mathcal{L}(\langle\sigma v\rangle; \hat{\nu} | \mathcal{D}_{\text{dSphs}}) = \prod_{l=1}^{N_{\text{dSphs}}} \max_{J_l} \left[ \mathcal{L}_{\text{dSph},l}(\langle\sigma v\rangle; J_l, \hat{\nu}_l | \mathcal{D}_l) \times \mathcal{J}_l(J_l | J_{l,\text{obs}}, \sigma_{\log J_l}) \right]. \quad (5.14)$$

900 In addition, Eq. (5.13) enables the combination of data from different gamma-ray instruments and  
 901 observed dSphs via tabulated values of  $\mathcal{L}_{\text{dSph},l}$ , or equivalently of  $\lambda$  from Eq. (5.10) as was done in

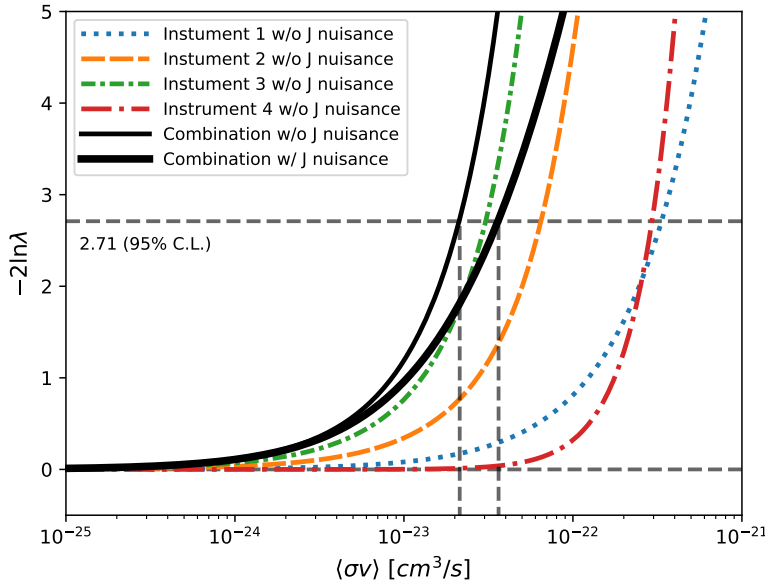


Figure 5.4 Illustration of the combination technique showing a comparison between  $-2 \ln \lambda$  provided by four instruments (colored lines) from the observation of the same dSph without any  $J$  nuisance and their sum, *i.e.* the resulting combined likelihood (thin black line). According to the test statistics of Equation (5.6), the intersection of the likelihood profiles with the line  $-2 \ln \lambda = 2.71$  indicates the 95% C.L. upper limit on  $\langle \sigma v \rangle$ . The combined likelihood (thin black line) shows a smaller value of upper limit on  $\langle \sigma v \rangle$  than those derived by individual instruments. We also show how the uncertainties on the  $J$  factor effects the combined likelihood and degrade the upper limit on  $\langle \sigma v \rangle$  (thick black line). All likelihood profiles are normalized so that the global minimum  $\widehat{\langle \sigma v \rangle}$  is 0. We note that each profile depends on the observational conditions in which a target object was observed. The sensitivity of a given instrument can be degraded and the upper limits less constraining if the observations are performed in non-optimal conditions such as a high zenith angle or a short exposure time.

902 this work, versus  $\langle \sigma v \rangle$ .  $\mathcal{L}_{dSph,l}$  is computed for a fixed value of  $J_l$  and profiled with respect to all  
 903 instrumental nuisance parameters  $\nu_l$ , these nuisance parameters are discussed in more detail below.  
 904 These values are produced by each detector independently and therefore there is no need to share  
 905 sensitive low-level information used to produce them, such as event lists. Figure 5.4 illustrates the  
 906 multi-instrument combination technique used in this study with a comparison of the upper limit  
 907 on  $\langle \sigma v \rangle$  obtained from the combination of the observations of four experiments towards one dSph  
 908 versus the upper limit from individual instruments. It also shows graphically the effect of the  
 909  $J$ -factor uncertainty on the combined observations.

910 The *partial* joint likelihood function for gamma-ray observations of each dSph ( $\mathcal{L}_{dSph,l}$ ) is

written as the product of the likelihood terms describing the  $N_{\text{exp},l}$  observations performed with any of our observatories:

$$\mathcal{L}_{\text{dSph},l} (\langle \sigma v \rangle; J_l, \nu_l | \mathcal{D}_l) = \prod_{k=1}^{N_{\text{exp},l}} \mathcal{L}_{lk} (\langle \sigma v \rangle; J_l, \nu_{lk} | \mathcal{D}_{lk}), \quad (5.15)$$

where each  $\mathcal{L}_{lk}$  term refers to an observation of the  $l$ -th dSph with associated  $k$ -th instrument responses.  $N_{\text{exp},l}$  varies from dSph to dSph and can be inferred from Table 5.2.

Each collaboration separately analyzes their data for  $\mathcal{D}_{lk}$  corresponding to dSph  $l$  and gamma-ray detector  $k$ , using as many common assumptions as possible in the analysis. HAWC's treatment was described earlier in Section 5.4.1 whereas the specifics of the remaining experiments is left to the publication. We compute the values for the likelihood functions  $\mathcal{L}_{lk}$  (see Eq. (5.15)) for a fixed value of  $J_l$  and profile over the rest of the nuisance parameters  $\nu_{lk}$ . Then, values of  $\lambda$  from Eq. (5.10) are computed as a function of  $\langle \sigma v \rangle$ , and shared using a common format. Results are computed for seven annihilation channels,  $W^+W^-$ ,  $ZZ$ ,  $b\bar{b}$ ,  $t\bar{t}$ ,  $e^+e^-$ ,  $\mu^+\mu^-$ , and  $\tau^+\tau^-$  over 62  $m_\chi$  values between 5 GeV and 100 TeV provided in [44]. The  $\langle \sigma v \rangle$  range is defined between  $10^{-28}$  and  $10^{-18} \text{ cm}^3 \cdot \text{s}^{-1}$ , with 1001 logarithmically spaced values. The likelihood combination, i.e. Equation (5.11), and profile over the  $J$ -factor to compute the profile likelihood ratio  $\lambda$ , Equation (5.10), are carried out with two different public analysis software packages, namely `gLike` [50] and `LklCom` [51], that provide the same results [52].

As mentioned previously, each experiment computes the  $\mathcal{L}_{lk}$  from Equation (5.10) differently. The remainder of this section highlights the differences in this calculation across the experiments. Four experiments, namely *Fermi*-LAT, H.E.S.S., HAWC and MAGIC, use a binned likelihood to compute the  $\mathcal{L}_{lk}$ . For these experiments, for each observation  $\mathcal{D}_{lk}$  of a given dSph  $l$  carried out using a given gamma-ray detector  $k$ , the binned likelihood function is:

$$\mathcal{L}_{lk} (\langle \sigma v \rangle; J_l, \nu_{lk} | \mathcal{D}_{lk}) = \prod_{i=1}^{N_E} \prod_{j=1}^{N_P} \left[ \mathcal{P}(s_{lk,ij}(\langle \sigma v \rangle, J_l, \nu_{lk}) + b_{lk,ij}(\nu_{lk}) | N_{lk,ij}) \right] \times \mathcal{L}_{lk,\nu} (\nu_{lk} | \mathcal{D}_{\nu_{lk}}) \quad (5.16)$$

where  $N_E$  and  $N_P$  are the number of considered bins in reconstructed energy and arrival direction, respectively;  $\mathcal{P}$  represents a Poisson PDF for the number of gamma-ray candidate events  $N_{lk,ij}$

934 observed in the  $i$ -th bin in energy and  $j$ -th bin in arrival direction, when the expected number is  
 935 the sum of the expected mean number of signal events  $s_{ij}$  (produced by DM annihilation) and of  
 936 background events  $b_{ij}$ ;  $\mathcal{L}_{lk,\nu}$  is the likelihood term for the extra  $\nu_{lk}$  nuisance parameters that vary  
 937 from one instrument  $k$  to another. The expected counts for signal events  $s_{ij}$  for a given dSph  $l$  and  
 938 detector  $k$  is given by:

$$s_{ij}(\langle\sigma\nu\rangle, J) = \int_{E'_{\min,i}}^{E'_{\max,i}} dE' \int_{P'_{\min,j}}^{P'_{\max,j}} d\Omega' \int_0^\infty dE \int_{\Delta\Omega_{tot}} d\Omega \int_0^{T_{\text{obs}}} dt \frac{d^2\Phi(\langle\sigma\nu\rangle, J)}{dEd\Omega} \text{IRF}(E', P' | E, P, t) \quad (5.17)$$

939 where  $E'$  and  $E$  are the reconstructed and true energies,  $P'$  and  $P$  the reconstructed and true  
 940 arrival directions;  $E'_{\min,i}$ ,  $P'_{\min,j}$ ,  $E'_{\max,i}$ , and  $P'_{\max,j}$  are their lower and upper limits of the  $i$ -th  
 941 energy bin and the  $j$ -th arrival direction bin;  $T_{\text{obs}}$  is the (dead-time corrected) total observation  
 942 time;  $t$  is the time along the observations;  $d^2\Phi/dEd\Omega$  is the DM flux in the source region (see  
 943 Equation (7.1)); and  $\text{IRF}(E', P' | E, P, t)$  is the IRF, which can be factorized as the product of the  
 944 effective collection area of the detector  $A_{\text{eff}}(E, P, t)$ , the PDFs for the energy estimator  $f_E(E' | E, t)$ ,  
 945 and arrival direction  $f_P(P' | E, P, t)$  estimators. Note that for Fermi-LAT, HAWC, MAGIC, and  
 946 VERITAS the effect of the finite angular resolution is taken into account through the convolution  
 947 of  $d\Phi/dEd\Omega$  with  $f_P$  in Equation (5.17), whereas in the cases of H.E.S.S.  $f_P$  is approximated by a  
 948 delta function. This approximation has been made in order to maintain compatibility of the result  
 949 with what has been previously published. The difference introduced by this approximation is  $< 5\%$   
 950 for all considered dSphs. A more comprehensive review of the differences between the analyses of  
 951 different instruments can be found in [25].

## 952 5.5 HAWC Results

953 13 of the 20 dSphs considered for the Glory Duck analysis are within HAWC's field of view.  
 954 These dSph are analyzed for emission from DM annihilation according to the likelihood method  
 955 described in Section 5.4. The 13 likelihood profiles are then stacked to synthesize a combined  
 956 limit on the dark matter cross-section,  $\langle\sigma\nu\rangle$ . This combination is done for the 7 SM annihilation  
 957 channels used in the Glory Duck analysis. Figure 5.5 shows the combined limit for all annihilation  
 958 channels with HAWC only observations. We also perform 300 studies of Poisson trials on the

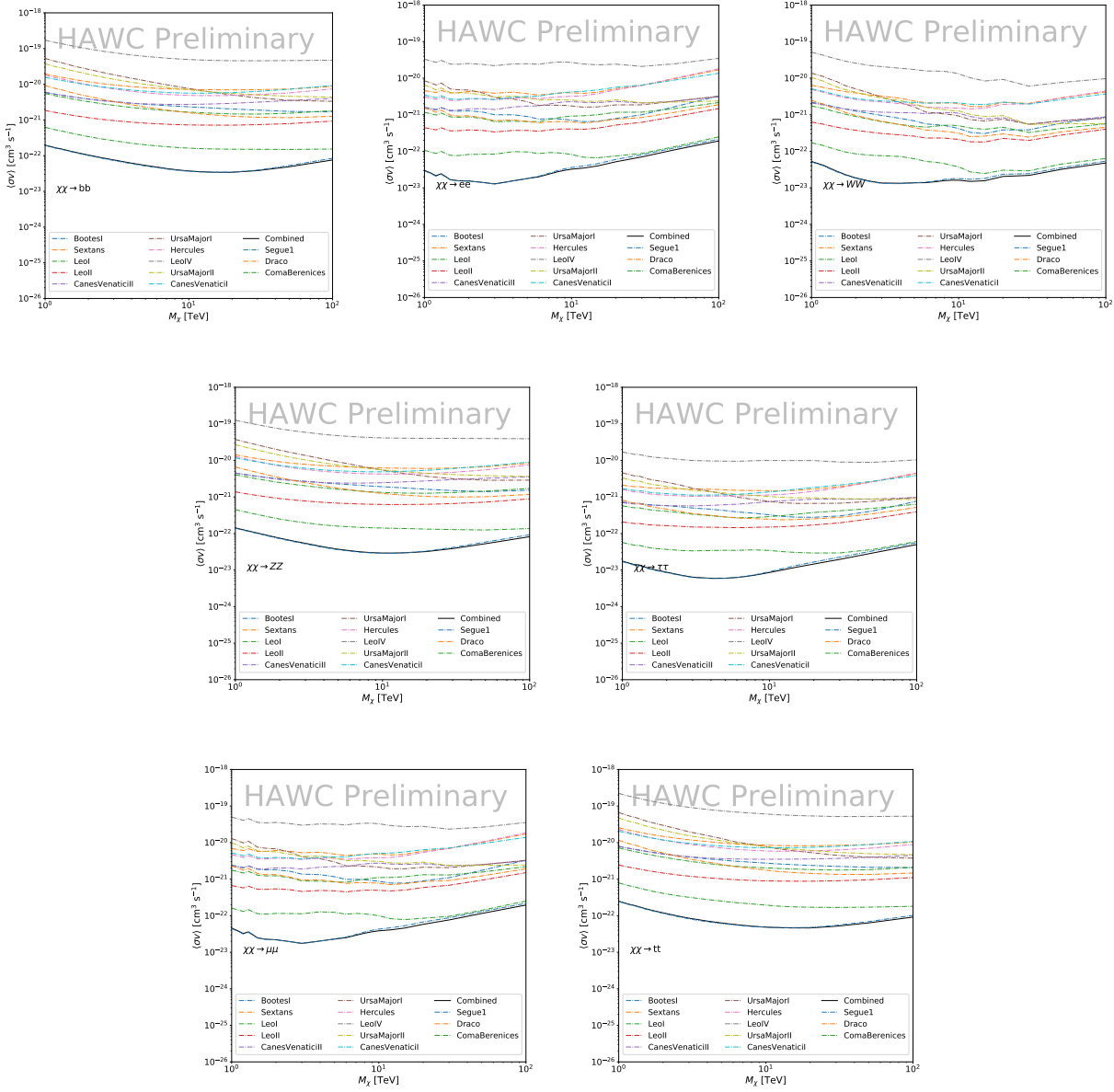


Figure 5.5

background. These trials are used to produce HAWC Brazil bands which were shared with the other collaborators for combined Brazil Bands. The results on fitting to HAWC's Poisson trials of the DM hypothesis is shown in Figure 5.7 for all the DM annihilation channels studied for Glory Duck.

No DM was found in HAWC observations. HAWC's limits are dominated by the dSphs Segue1 and Coma Berenices. The remaining 11 dSphs do not contribute significantly to the limit because

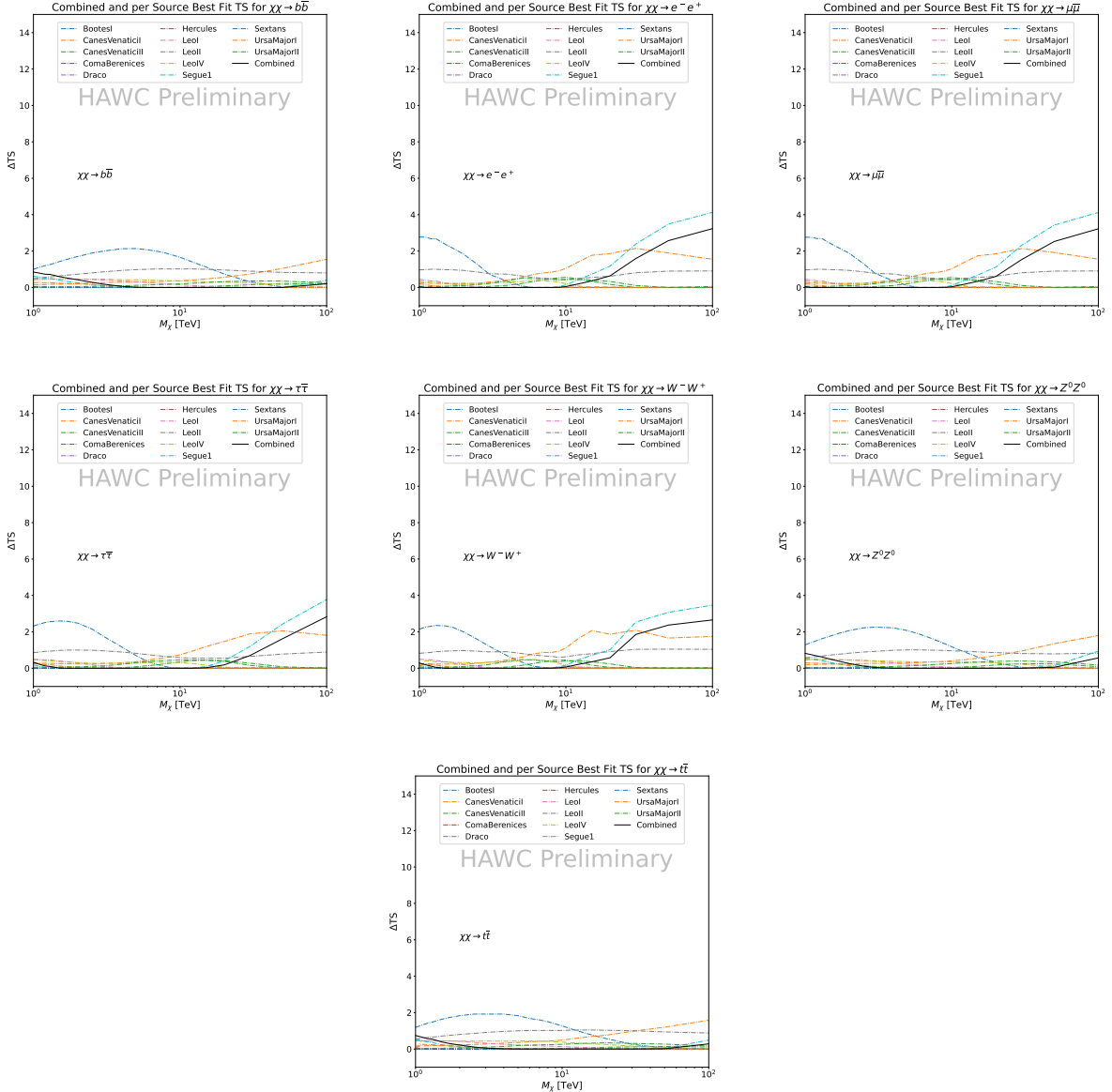


Figure 5.6 HAWC TS values for best fit  $\langle \sigma v \rangle$  versus  $m_\chi$  for seven SM annihilation channels with  $J$  factors from  $\mathcal{GS}$ . The solid black line shows the combined best fit TS values. The colored, dashed lines are the TS values for each of the 13 sources HAWC studied.

they are at high zenith and/or have much smaller  $J$  factors. Even though some remaining dSphs have large  $J$  factors, they are towards the edge of HAWC's field of view where HAWC analysis is less sensitive.

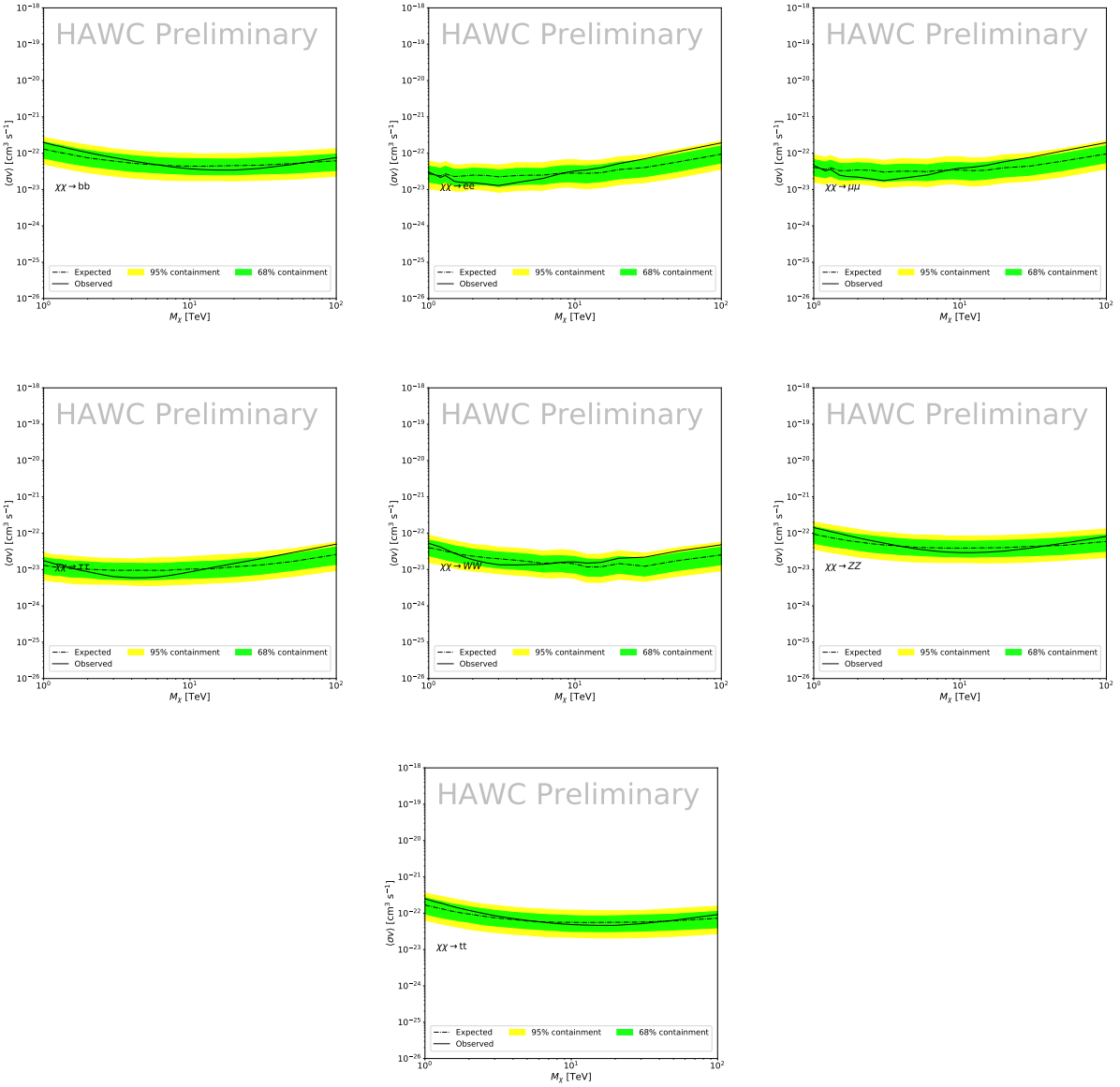


Figure 5.7 HAWC Brazil bands at 95% confidence level on  $\langle\sigma v\rangle$  versus DM mass for seven annihilation channels with  $J$ -factors from  $\mathcal{GS}$  [53]. The solid line represents the combined limit from 13 dSphs. The dashed line is the expected limit. The green band is the 68% containment. The yellow band is the 95% containment.

## 968 5.6 Glory Duck Combined Results

969 The crux of this analysis is that HAWC's results are combined with 4 other gamma-ray observa-  
 970 tories: Fermi-LAT, H.E.S.S., MAGIC, and VERITAS. No significant DM emission was observed  
 971 by any of the five instruments. We present the upper limits on  $\langle\sigma v\rangle$  assuming seven independent  
 972 DM self annihilation channels, namely  $W^+W^-$ ,  $Z^+Z^-$ ,  $b\bar{b}$ ,  $t\bar{t}$ ,  $e^+e^-$ ,  $\mu^+\mu^-$ , and  $\tau^+\tau^-$ . The 68%

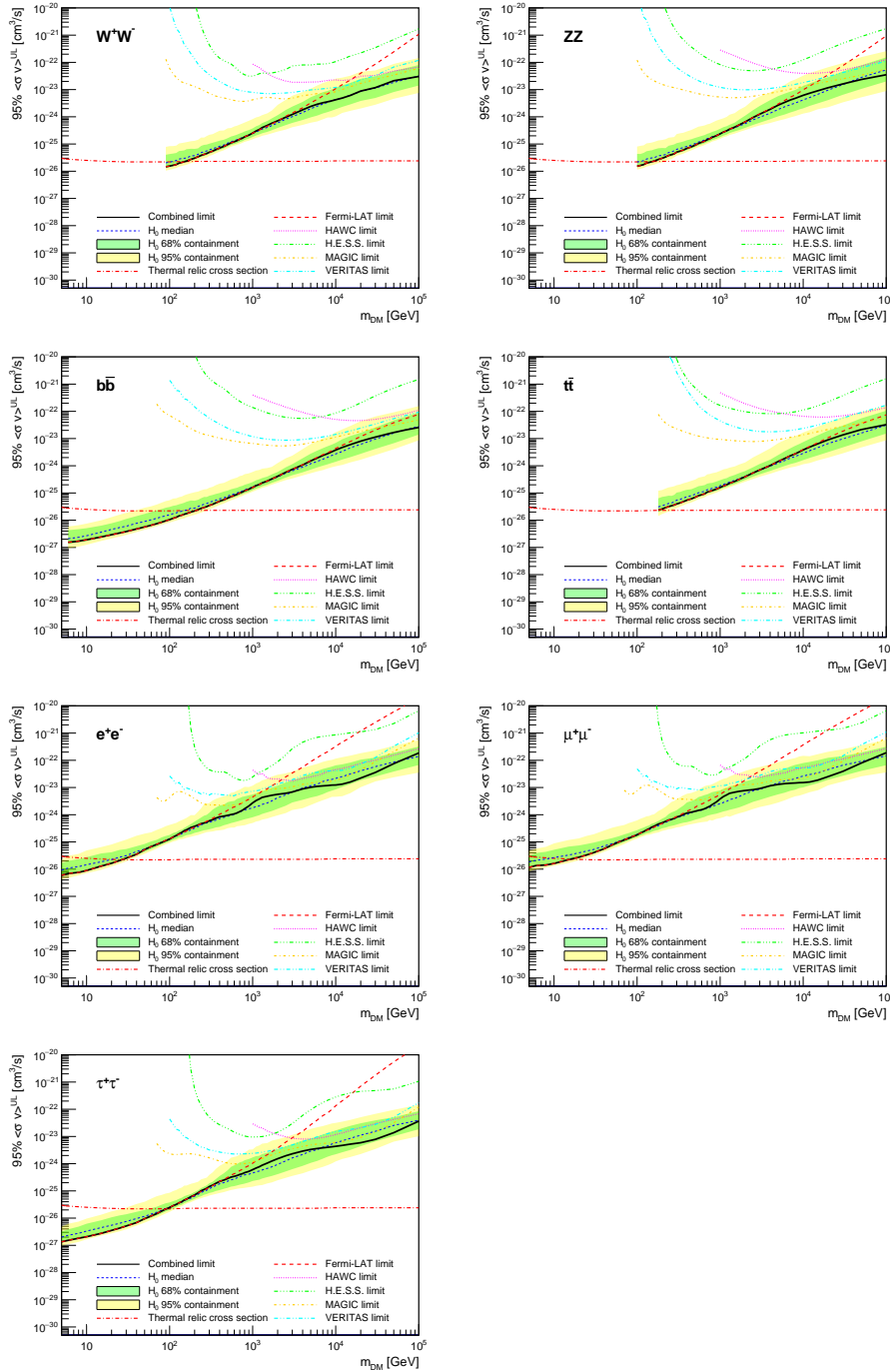


Figure 5.8 Upper limits at 95% confidence level on  $\langle\sigma v\rangle$  in function of the DM mass for eight annihilation channels, using the set of  $J$  factors from Ref. [53] ( $\mathcal{GS}$  set in Table 5.1). The black solid line represents the observed combined limit, the black dashed line is the median of the null hypothesis corresponding to the expected limit, while the green and yellow bands show the 68% and 95% containment bands. Combined upper limits for each individual detector are also indicated as solid, colored lines. The value of the thermal relic cross-section in function of the DM mass is given as the red dotted-dashed line [54].

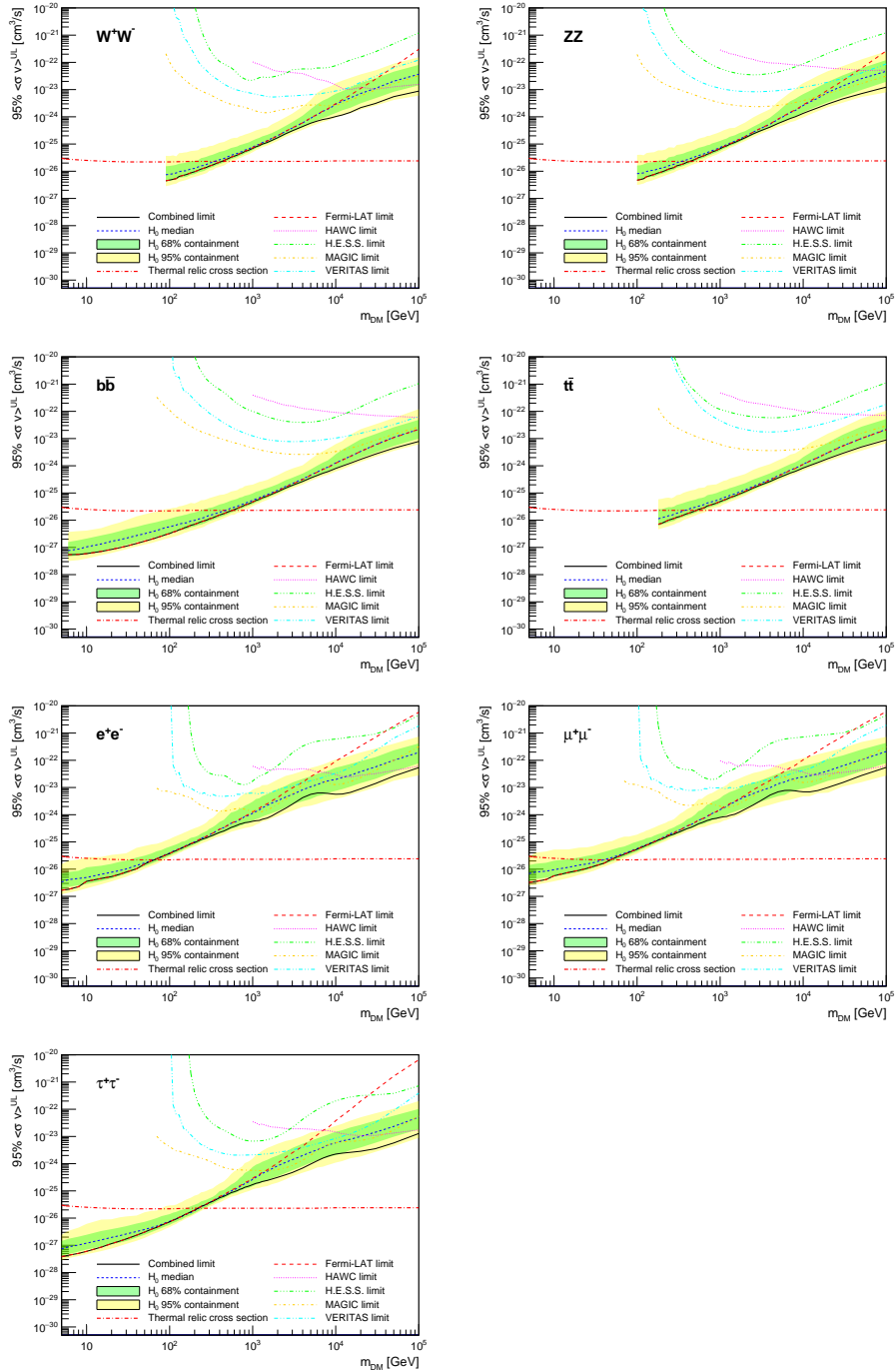


Figure 5.9 Same as Fig. 5.8, using the set of  $J$  factors from Ref. [47, 55] ( $\mathcal{B}$  set in Table 5.1).

and 95% containment bands are produced from 300 Poisson realizations of the null hypothesis corresponding to each of the combined datasets. These 300 realizations are combined identically to dSph observations. The containment bands and the median are extracted from the distribution of resulting limits on the null hypothesis. These 300 realizations are obtained either by fast simu-

977 lations of the OFF observations, for H.E.S.S., MAGIC, VERITAS, and HAWC, or taken from real  
978 observations of empty fields of view in the case of Fermi-LAT [48, 56, 57].

979 The obtained limits are shown in Figure 5.8 for the  $\mathcal{G}\mathcal{S}$  set of  $J$ -factors [53] and in Figure 5.9  
980 for the  $\mathcal{B}$  set of  $J$ -factors [47, 55]. The combined limits are presented with their 68% and 95%  
981 containment bands, and are expected to be close to the median limit when no signal is present.  
982 We observe agreement with the null hypothesis for all channels, within  $2\sigma$  standard deviations,  
983 between the observed limits and the expectations given by the median limits. Limits obtained from  
984 each detector are also indicated in the figures, where limits for all dSphs observed by the specific  
985 instrument have been combined.

986 Below  $\sim 300$  GeV, the *Fermi*-LAT dominates the DM limits for all annihilation channels. From  
987  $\sim 300$  GeV to  $\sim 2$  TeV, *Fermi*-LAT continues to dominate for the hadronic and bosonic DM channels,  
988 yet the IACTs (H.E.S.S., MAGIC, and VERITAS) and *Fermi*-LAT all contribute to the limit for  
989 leptonic DM channels. For DM masses between  $\sim 2$  TeV to  $\sim 10$  TeV, the IACTs dominate leptonic  
990 DM annihilation channels, whereas both the *Fermi*-LAT and the IACTs dominate bosonic and  
991 hadronic DM annihilation channels. From  $\sim 10$  TeV to  $\sim 100$  TeV, both the IACTs and HAWC  
992 contribute significantly to the leptonic DM limit. For hadronic and bosonic DM, the IACTs and  
993 *Fermi*-LAT both contribute strongly.

994 We notice that the limits computed using the  $\mathcal{B}$  set of  $J$ -factor are always better compared to the  
995 ones calculated with the  $\mathcal{G}\mathcal{S}$  set. For the  $W^+W^-$ ,  $Z^+Z^-$ ,  $b\bar{b}$ , and  $t\bar{t}$  channels, the ratio between the  
996 limits computed with the two sets of  $J$ -factor is varying between a factor of  $\sim 3$  and  $\sim 5$  depending  
997 on the energy, with the largest ratio around 10 TeV. For the channels  $e^+e^-$ ,  $\mu^+\mu^-$ , and  $\tau^+\tau^-$ , the  
998 ratio lies between  $\sim 2$  to  $\sim 6$ , being maximum around 1 TeV. Examining Figure 5.16 and Figure 5.17  
999 in Section 5.8, these differences are explained by the fact that the  $\mathcal{B}$  set provides higher  $J$ -factors  
1000 for the majority of the studied dSphs, with the notable exception of Segue I. The variation on the  
1001 ratio of the limits for the two sets is due to different dSph dominating the limits depending on the  
1002 energy. This pushes the range of thermal cross-section which can be excluded to higher mass. This  
1003 comparison demonstrates the magnitude of systematic uncertainties associated with the choice of

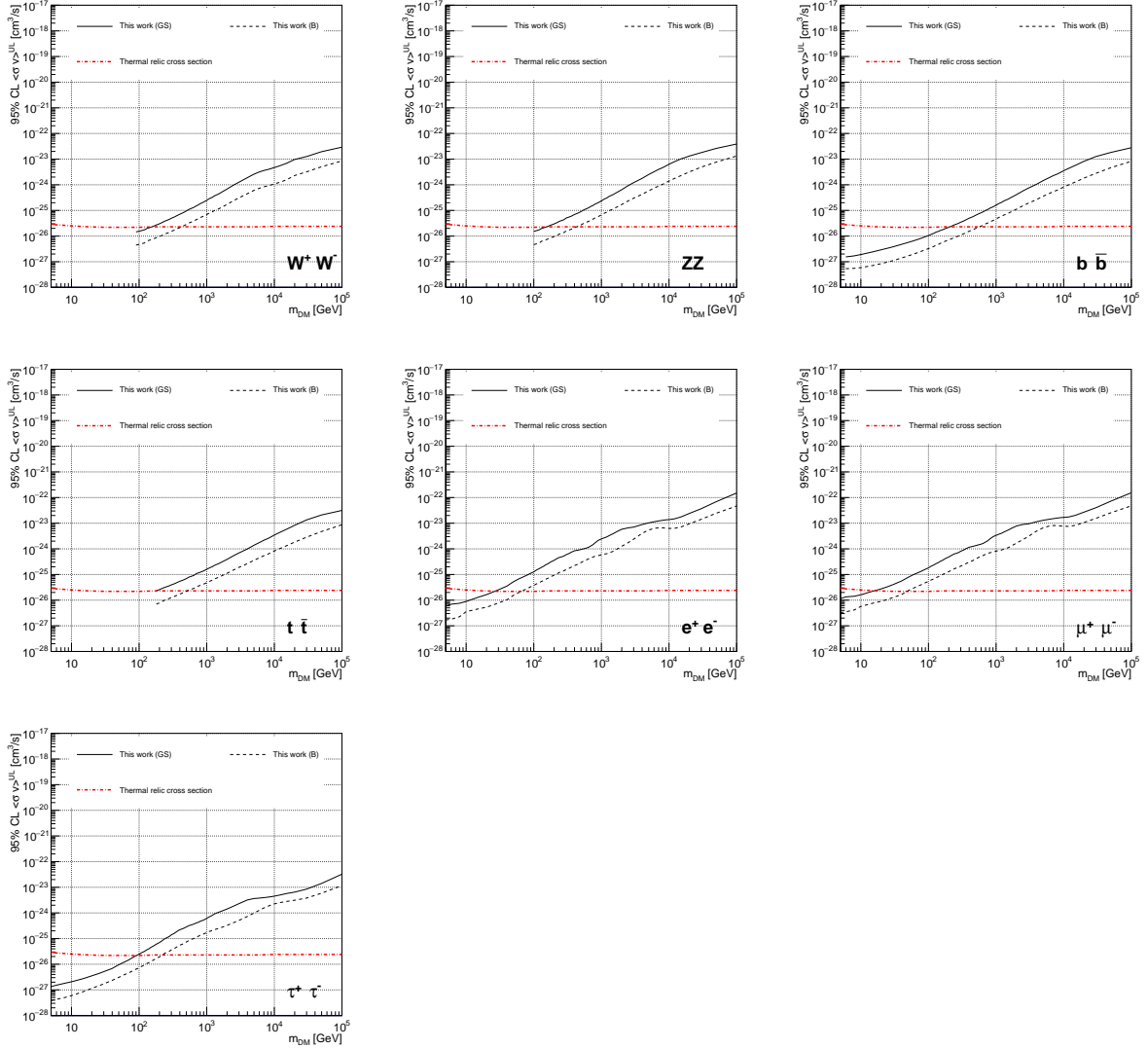


Figure 5.10 Comparisons of the combined limits at 95% confidence level for each of the eight annihilation channels when using the  $J$  factors from Ref. [53] ( $\mathcal{GS}$  set in Table 5.1), plain lines, and the  $J$  factor from Ref. [47, 55] ( $\mathcal{B}$  set in Table 5.1), dashed lines. The cross-section given by the thermal relic is also indicated [54].

#### 1004 the $J$ -factor

1005 This comparison demonstrates the magnitude of systematic uncertainties associated with the  
 1006 choice of the  $J$ -factor calculation. The  $\mathcal{GS}$  and  $\mathcal{B}$  sets present a difference in the limits for all  
 1007 channels of about This difference is explained, see Figure 5.16 and Figure 5.17 in Appendix, by the  
 1008 fact that the  $\mathcal{B}$  set provides higher  $J$  factors for all dSph except for Segue I. This pushes the range  
 1009 of thermal cross-section which can be excluded to higher mass.

1010 **5.7 HAWC Systematics**

1011 **5.7.1 Inverse Compton Scattering**

1012     The DM-DM annihilation channels produce many high energy electrons regardless of the  
1013 primary annihilation channel. These high energy electrons can produce high energy gamma-rays  
1014 through Inverse Compton Scattering (ICS). If this effect is strong, it would change the morphology  
1015 of the source and increase the total expected gamma-ray counts from any source. The PPPC [44]  
1016 provides tools in Mathematica for calculating the impact of ICS for an arbitrary location in the  
1017 sky for a specified annihilation channel. We calculated the change in gamma-ray counts for DM  
1018 annihilation to primary  $e\bar{e}$  for RA and Dec corresponding to Segue1 and Coma Berenices. These  
1019 dSphs were chosen because they are the strongest contributors to the limit.  $e\bar{e}$  was selected because  
1020 it would have the largest number of high energy electrons. The effect was found to be on the order  
1021 of  $10^{-7}$  on the gamma-ray spectrum. As a result, this systematic is not considered in our analysis.

1022 **5.7.2 Point Source Versus Extended Source Limits**

1023     The previous DM search toward dSph approximated the dSphs as point sources [46]. In  
1024 this analysis, the dSphs are implemented as extended with J-factor distributions following those  
1025 produced by [53]. The resolution of the cited map is much finer than HAWC's angular resolution.  
1026 The vast majority of the J-factor distribution is represented on the central HAWC pixel of the dSph  
1027 spatial map. However, the neighboring 8 pixels are not negligible and contribute to our limit.

1028     Figure 5.11 shows a substantial improvement to the limit for Segue1. Fig. 5.12 however showed  
1029 identical limits. These disparities are best explained by the relative difference in their J-Factors.  
1030 Both dSphs pass almost overhead the HAWC detector, however Segue1 has the larger J-Factor  
1031 between the two. Adjacent pixels to the central pixel will therefore contribute to the limits. This is  
1032 the case for other dSph that are closer to overhead the HAWC detector.

1033     Comparison plots for all sources and the combined limit can be found in the sandbox for the  
1034 Glory Duck project.

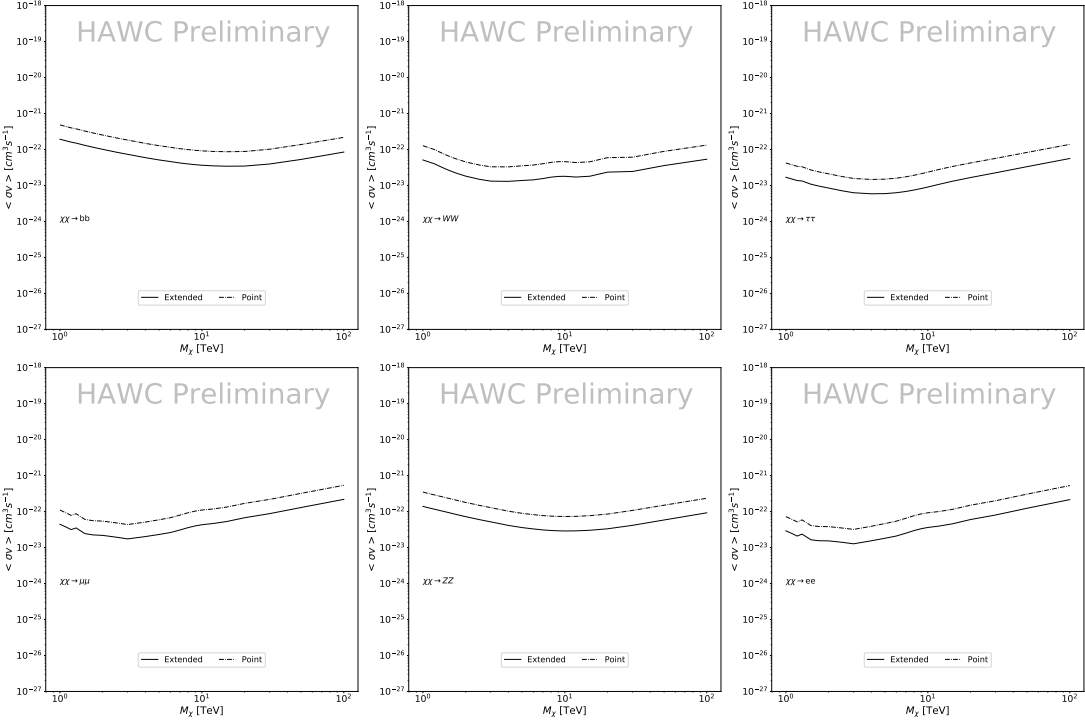


Figure 5.11 Comparisons of the combined limits at 95% confidence level for a point source analysis and extended source using [53]  $\mathcal{GS}$  J-factor distributions and PPPC [44] annihilation spectra. Shown are the limits for Segue1 which will have the most significant impact on the combined limit. 6 of the 7 DM annihilation channels are shown. Solid lines are extended source studies. Dashed lines are point source studies. Overall, the extended source analysis improves the limit by a factor of 2.

### 1035 5.7.3 Impact of Pointing Systematic

1036 During the analysis it was discovered that reconstruction of gamma-rays. Slides describing this  
 1037 systematic can be found [here](#). Shown on the presentation is dependence on the pointing systematic  
 1038 on declination. New spatial profiles were generated for every dSph and limits were computed for  
 1039 the adjusted declination.

1040 Section 5.7.3 demonstrates the impact of this systematic for all DM annihilation channels  
 1041 studied by HAWC. The impact is a tiny improvement, yet mostly identical, to the combined limits.

## 1042 5.8 J-factor distributions

### 1043 5.8.1 Numerical integration of $\mathcal{GS}$ maps

1044 It was discovered well after the HAWC analysis was completed that the published tables from  
 1045  $\mathcal{GS}$  [45] quoted median J-factors were computed in a non-trivial manner. The assumption myself

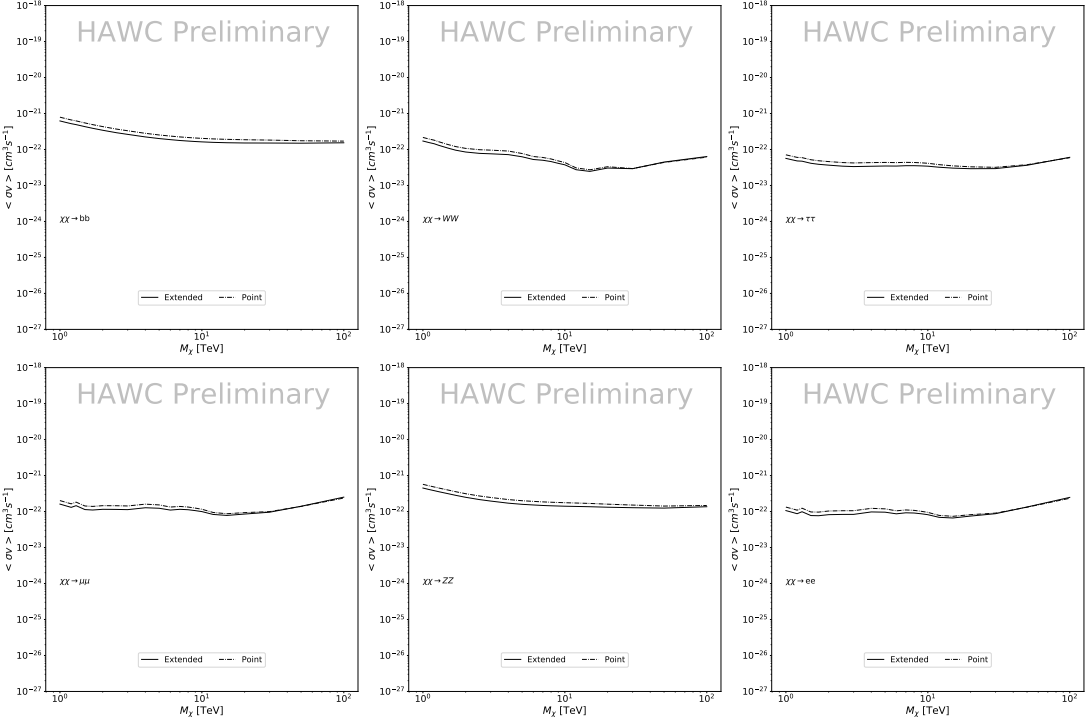


Figure 5.12 Same as Fig. 5.11 on Coma Berenices. This dSph also contributes significantly to the limit. The limits are identical in this case.

and collaborators had been that the published tables represented the  $J$ -factor as a function of  $\theta$  for the best global fit model on a per-source basis. However, this is not the case. Instead, what is published are the best fit model for each dwarf that only considers stars up to the angular separation  $\theta$ . Therefore, the model is changing for each value of  $\theta$  for each dwarf. Yet, the introduced features from unique models at each  $\theta$  are much smaller than the angular resolution of HAWC. It is not expected for these effects to impact the limits and TS greatly as a result.

Median  $J$ -factor model profiles were provided by the authors. New maps were generated and analyzed for Segue1 and Coma Berenices. Figure 5.14 shows the differential between maps generated with the method from Section 5.8.1 and from the authors of [45]. These maps were reanalyzed for all SM DM annihilation channels. Upper limits for these channels are shown in Figure 5.15

From Figure 5.15, we can see that the impact of these model difference was no substantial. The observed impact was a fractional effect which is much smaller than the impact from selecting another DM spatial distribution model as was shown in Figure 5.10.

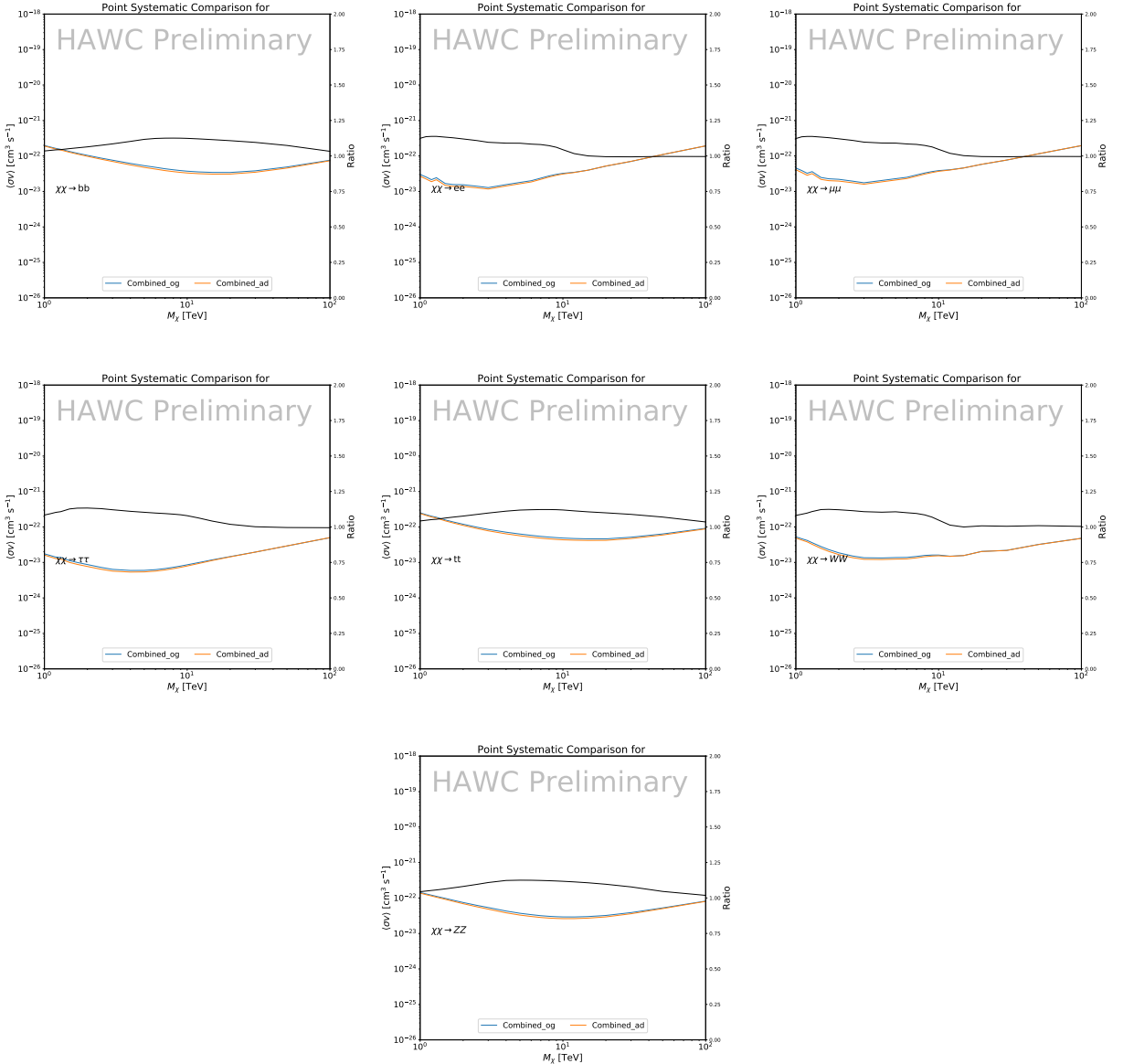


Figure 5.13 Comparison of combined limits when correcting for HAWC's pointing systematic. All DM annihilation channels are shown. The solid black line is the ratio between published limit to the declination corrected limit. The blue solid line or "Combined\_og" represented the limits computed for Glory Duck. The solid orange line or "Combined\_ad" represented the limits computed after correcting for the pointing systematic.

## 1060 5.8.2 $\mathcal{G}\mathcal{S}$ Versus $\mathcal{B}$ spatial models

1061 We show in this appendix a comparison between the  $J$ -factors computed by Geringer-Sameth  
 1062 *et al.* [53] (the  $\mathcal{G}\mathcal{S}$  set) and the ones computed by Bonnivard *et al.* [47, 55] (the  $\mathcal{B}$  set). The  
 1063  $\mathcal{G}\mathcal{S}$   $J$ -factors are computed through a Jeans analysis of the kinematic stellar data of the selected

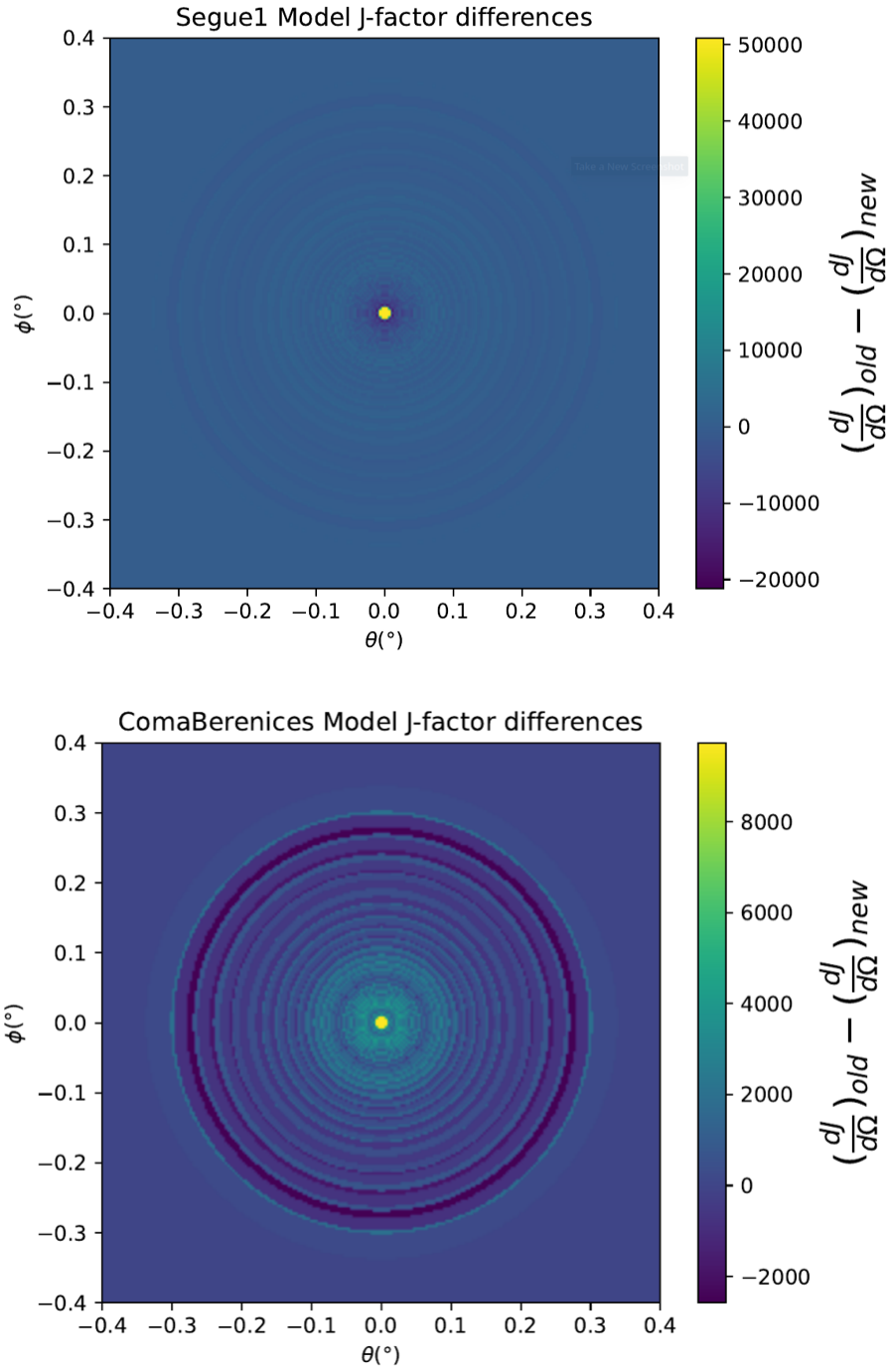


Figure 5.14 Differential map of  $dJ/\Omega$  from model built in Section 5.8.1 and profiles provided directly from authors. (Top) Differential from Segue1. (bottom) Differential from Coma Berenices. Note that their scales are not the same. Segue1 shows the deepest discrepancies which is congruent with its large uncertainties. Both models show anuli where unique models become apparent.

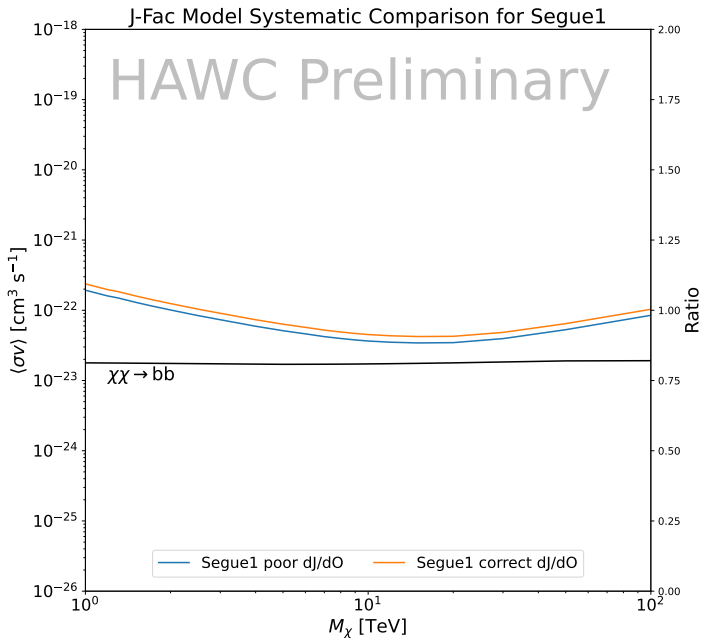
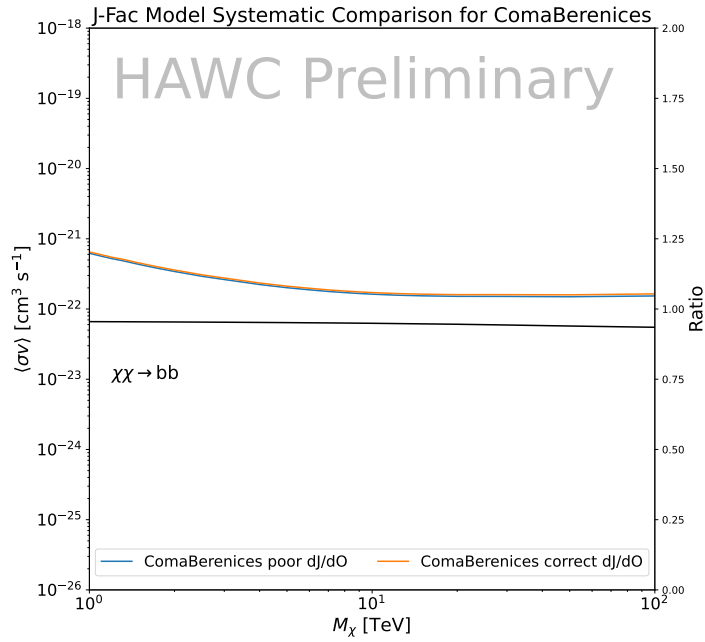


Figure 5.15 HAWC limits for Coma Berenices (top) and Segue1 (bottom) for two different map sets. Blue lines are limits calculated on maps with poor model representation. Orange lines are limits calculated on spatial profiles provided by the authors of [45]. Black line is the ratio of the poor spatial model limits to the corrected spatial models. The left y-axis measures  $\langle \sigma v \rangle$  for the blue and orange lines. The right y-axis measures the ratio and is unitless.

1064 dSphs, assuming a dynamic equilibrium and a spherical symmetry for the dSphs. They adopted  
1065 the generalized DM density distribution, known as Zhao-Hernquist, introduced by [58], carrying  
1066 three additional index parameters to describe the inner and outer slopes, and the break of the  
1067 density profile. Such a profile parametrization allows the reduction of the theoretical bias from  
1068 the choice of a specific radial dependency on the kinematic data. In other words, the increase of  
1069 free parameters with the use of the Zhao-Hernquist profile allows a better description of the mass  
1070 density distribution of dark matter.

1071 In addition, a constant velocity anisotropy profile and a Plummer light profile [59] for the stellar  
1072 distribution were assumed. The velocity anisotropy profile depends on the radial and tangential  
1073 velocity dispersion. However, its determination remains challenging since only the line-of-sight  
1074 velocity dispersion can be derived from velocity measurements. Therefore, the parametrization of  
1075 the anisotropy profile is obtained from simulated halos (see [60] for more details). They provide the  
1076 values of the  $J$ -factors of regions extending to various angular radius up to the outermost member  
1077 star.

1078 The  $\mathcal{B}$   $J$ -factors were computed through a Jeans analysis taking into account the systematic  
1079 uncertainties induced by the DM profile parametrization, the radial velocity anisotropy profile, and  
1080 the triaxiality of the halo of the dwarf galaxies. They performed a more complete study of the dSph  
1081 kinematics and dynamics than  $\mathcal{GS}$  for the determination of the  $J$ -factor. Conservative values of the  
1082  $J$ -factors where obtained using an Einasto DM density profile [61], a realistic anisotropy profile  
1083 known as the Baes & Van Hese profile [62] which takes into account that the inner regions can be  
1084 significantly non-isotropic, and a Zhao-Hernquist light profile [58].

1085 For both sets,  $J$ -factor values are provided for all dSphs as a function of the radius of the  
1086 integration region [53, 47, 55]. Table 5.1 shows the heliocentric distance and Galactic coordinates  
1087 of the twenty dSphs, together with the two sets of  $J$ -factor values integrated up to the outermost  
1088 observed star for  $\mathcal{GS}$  and the tidal radius for  $\mathcal{B}$ . Both  $J$ -factor sets were derived through a Jeans  
1089 analysis based on the same kinematic data, except for Draco where the measurements of [63] have  
1090 been adopted in the computation of the  $\mathcal{B}$  value. The computations for producing the  $\mathcal{GS}$  and  $\mathcal{B}$

1091 samples differ in the choice of the DM density, velocity anisotropy, and light profiles, for which the  
1092 set  $\mathcal{B}$  takes into account some sources of systematic uncertainties.

1093 Figure 5.16 and Figure 5.17 show the comparisons for the  $J$ -factor versus the angular radius  
1094 for each of the 20 dSphs used in this study. The uncertainties provided by the authors are also  
1095 indicated in the figures. For the  $\mathcal{GS}$  set, the computation stops at the angular radius corresponding  
1096 to the outermost observed star, while for the  $\mathcal{B}$  set, the computation stops at the angular radius  
1097 corresponding to the tidal radius.

## 1098 5.9 Discussion and Conclusions

1099 In this multi-instrument analysis, we have used observations of 20 dSphs from the gamma-ray  
1100 telescopes Fermi-LAT, H.E.S.S., MAGIC, VERITAS, and HAWC to perform a collective DM  
1101 search annihilation signals. The data were combined across sources and detectors to significantly  
1102 increase the sensitivity of the search. We have observed no significant deviation from the null, no  
1103 DM, hypothesis, and so present our results in terms of upper limits on the annihilation cross-section  
1104 for seven potential DM annihilation channels.

1105 Fermi-LAT brings the most stringent constraints for continuum channels below approximately  
1106 1 TeV. The remaining detectors dominate at higher energies. Overall, for multi-TeV DM mass,  
1107 the combined DM constraints from all five telescopes are 2-3 times stronger than any individual  
1108 telescope for multi-TeV DM.

1109 Derived from observations of many dSphs, our results produce robust limits given the DM  
1110 content of the dSphs is relatively well constrained. The obtained limits span the largest mass  
1111 range of any WIMP DM search. Our combined analysis improves the sensitivity over previously  
1112 published results from each detector which produces the most stringent limits on DM annihilation  
1113 from dSphs. These results are based on deep exposures of the most promising known dSphs with  
1114 the currently most sensitive gamma-ray instruments. Therefore, our results constitute a legacy of  
1115 a generation of gamma-ray instruments on WIMP DM searches towards dSphs. Our results will  
1116 remain the reference in the field until a new generation of more sensitive gamma-ray instruments  
1117 begin operations, or until new dSphs with higher  $J$ -factors are discovered.

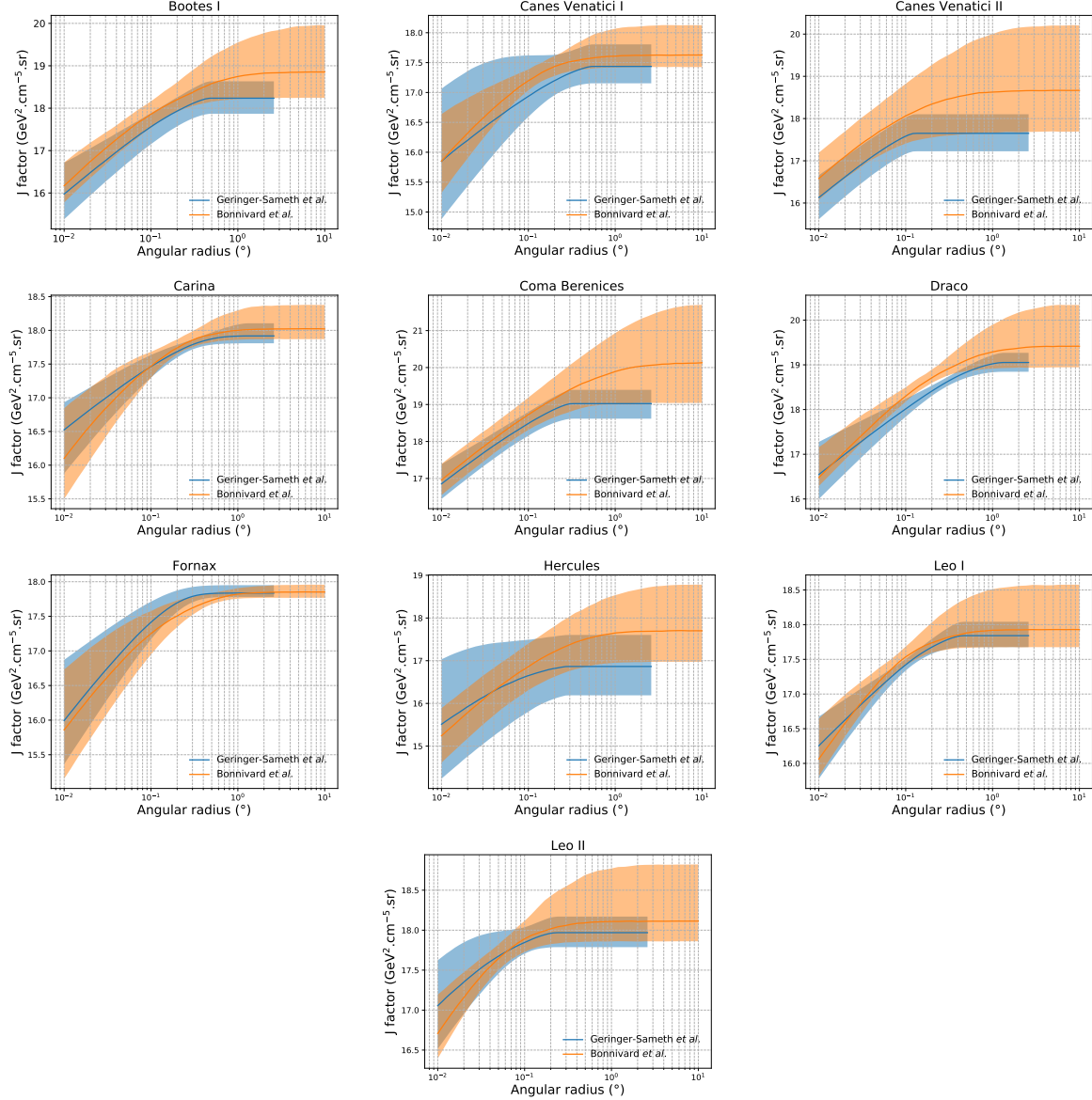


Figure 5.16 Comparisons between the  $J$ -factors versus the angular radius for the computation of  $J$  factors from Ref. [53] ( $\mathcal{GS}$  set in Table 5.1) in blue and for the computation from Ref. [47, 55] ( $\mathcal{B}$  set in Tab. 5.1) in orange. The solid lines represent the central value of the  $J$ -factors while the shaded regions correspond to the  $1\sigma$  standard deviation.

This analysis serves as a proof of concept for future multi-instrument and multi-messenger combination analyses. With this collaborative effort, we have managed to sample over four orders in magnitude in gamma-ray energies with distinct observational techniques. Determining the nature of DM continues to be an elusive and difficult problem. Larger datasets with diverse measurement techniques could be essential to tackling the DM problem. A future collaboration using similar

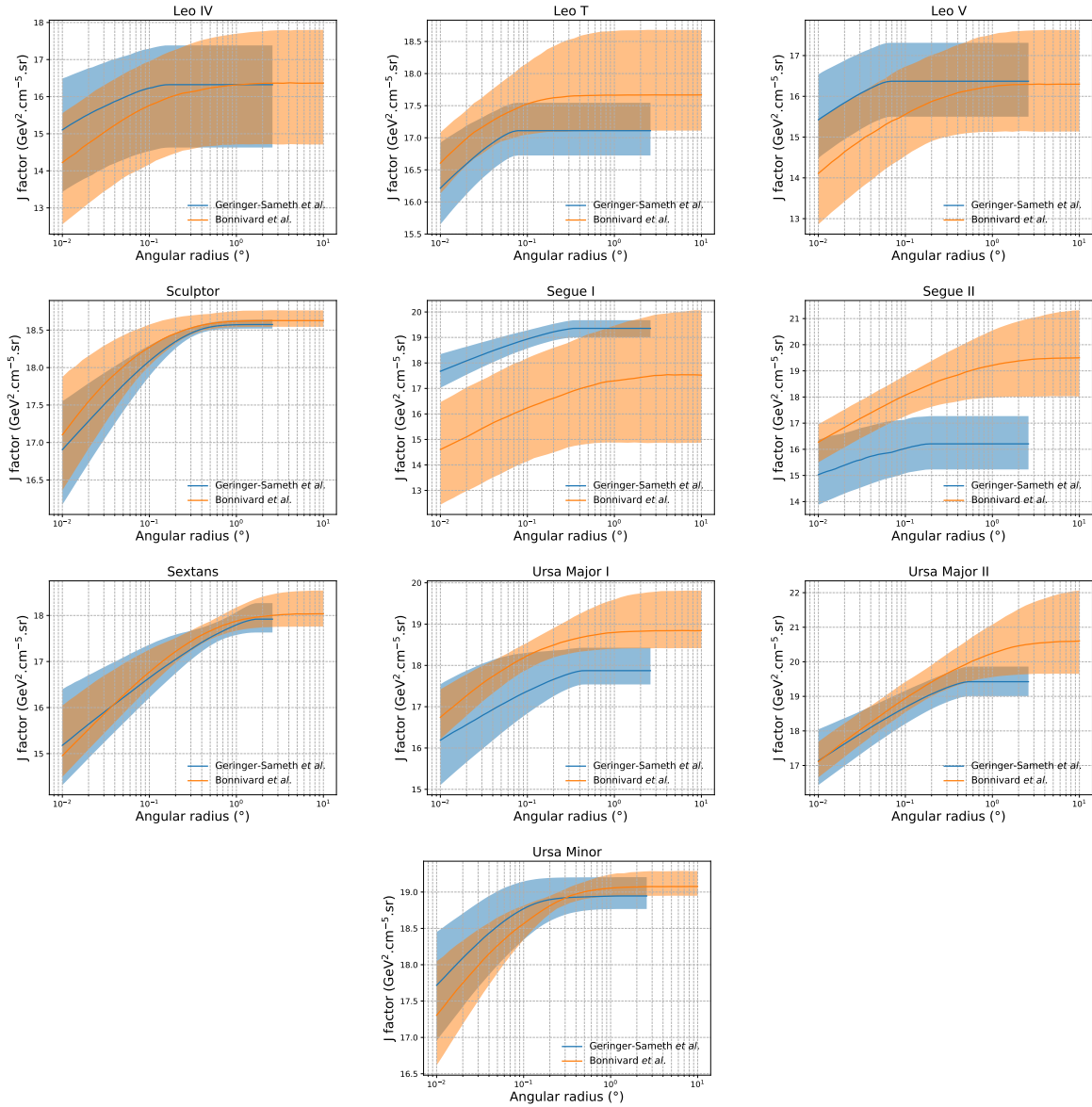


Figure 5.17 Comparisons between the  $J$ -factors versus the angular radius for the computation of  $J$  factors from Ref. [53] ( $\mathcal{GS}$  set in Tab. 5.1) in blue and for the computation from Ref. [47, 55] ( $\mathcal{B}$  set in Tab. 5.1) in orange. The solid lines represent the central value of the  $J$ -factors while the shaded regions correspond to the  $1\sigma$  standard deviation.

techniques as the ones described in this paper could grow even beyond gamma rays. The models we used for this study include annihilation channels with neutrinos in the final state. Advanced studies could aim to merge our results with those from neutrino observatories with large data sets. Efforts are already underway to add data from the IceCube, ANTARES, and KM3NeT observatories to these gamma-ray results.

1128 From this work, a selection of the best candidates for observations, according to the latest  
1129 knowledge on stellar dynamics and modelling techniques for the derivation of the  $J$ -factors on  
1130 the potential dSphs targets, is highly desirable at the time that new experiments are starting their  
1131 dark matter programs using dSphs. Given the systematic uncertainty inherent to the derivation of  
1132 the  $J$ -factors, an informed observational strategy would be to select both objects with the highest  
1133  $J$ -factors that could lead to DM signal detection, and objects with robust  $J$ -factor predictions, i.e.  
1134 with kinematic measurements on many bright stars, which would strengthen the DM interpretation  
1135 reliability of the observation outcome.

1136 This analysis combines data from multiple telescopes to produce strong constraints on astro-  
1137 physical objects. From this perspective, these methods can be applied beyond just DM searches.  
1138 Almost every astrophysical study can benefit from multi-telescope, multi-wavelength gamma-ray  
1139 studies. We have enabled these telescopes to study the cosmos with greater precision and detail.  
1140 Many astrophysical searches can benefit from multi-instrument gamma-ray studies, for which our  
1141 analysis lays the foundation.

## CHAPTER 6

### MULTITHREADING HAWC ANALYSES FOR DARK MATTER SEARCHES

#### 6.1 Introduction

HAWC's current software suite, plugins to 3ML, does not fully utilize computational advancements of recent decades. Said advancements include the proliferation of Graphical Processing Units (GPUs), and multithreading on multicore processors. The analysis described in chapter 5 took up to 3 months of human time waiting for the full gambit of data analysis and simulation of background to run. Additionally, with the addition of a 2D binning scheme,  $f_{\text{hit}}$  and NN, the time needed to compute expected to grow. Although excessive computing time was, in part, from an intense use of a shared computing cluster, it was evident that there was room for improvement. In HAWC's next generation dSph DM search, I decided to develop codes that would utilize the multicore processors on modern high performance computing clusters. The results of this work are featured in this chapter and brought a human timing improvement to computation that scales as  $1/N$  where  $N$  is the number of threads.

#### 6.2 Dataset and Background

This section enumerates the data and background methods used for HAWC's multithreaded study of dSphs. Section 6.2.1 and Section 6.2.2 are most useful for fellow HAWC collaborators looking to replicate a multithreaded dSph DM search.

##### 6.2.1 Itemized HAWC files

- Detector Resolution: `refit-Pass5-Final-NN-detRes-zenith-dependent.root`
- Data Map: `Pass5-Final-NN-maptree-ch103-ch1349-zenith-dependent.root`
- Spectral Dictionary: `HDMspectra_dict_gamma.npy`

##### 6.2.2 Software Tools and Development

This analysis was performed using HAL and 3ML [42, 43] in Python version 3. I built software in collaboration with Michael Martin and Letrell Harris to implement the *Dark Matter Spectra from*

1166 *the Electroweak to the Planck Scale* (HDM) [64] and dSphs spatial model from [65] for HAWC  
1167 analysis. A NumPy dictionary of HDM was made for Py3. The corresponding Python3 file is  
1168 `HDMspectra_dict_gamma.npy`. These files can also be used for decay channels and tools are  
1169 provided in HDM’s [git repository](#) [64]. The analysis was performed using the Neural Network  
1170 energy estimator for Pass 5.F. A description of this estimator was provided in chapter 3. **TODO:**  
1171 **Define a subsection when it’s written**, and its key improvements are an improved energy estimation  
1172 and improved sensitivities at higher zenith angles. All other software used for data analysis, DM  
1173 profile generation, and job submission to SLURM are also kept in my sandbox in the [Dark Matter](#)  
1174 [HAWC](#) project. The above repository also incorporates the model inputs used previously in Glory  
1175 Duck, described in chapter 5

1176 **6.2.3 Data Set and Background Description**

1177 The HAWC data maps used for this analysis contain 2565 days of data between runs 2104 (   
1178 **TODO: Day start**) and 7476 ( **TODO: Day end**). They were generated from pass 5.f reconstruction.  
1179 The analysis is performed using the NN energy estimator with bin list:

1180       B1C0Ea, B1C0Eb, B1C0Ec, B1C0Ed, B1C0Ee, B2C0Ea, B2C0Eb, B2C0Ec, B2C0Ed, B2C0Ee,  
1181       B3C0Ea, B3C0Eb, B3C0Ec, B3C0Ed, B3C0Ee, B3C0Ef, B4C0Eb, B4C0Ec, B4C0Ed, B4C0Ee,  
1182       B4C0Ef, B5C0Ec, B5C0Ed, B5C0Ee, B5C0Ef, B5C0Eg, B6C0Ed, B6C0Ee, B6C0Ef, B6C0Eg,  
1183       B6C0Eh, B7C0Ee, B7C0Ef, B7C0Eg, B7C0Eh, B7C0Ei, B8C0Ee, B8C0Ef, B8C0Eg, B8C0Eh,  
1184       B8C0Ei, B8C0Ej, B9C0Ef, B9C0Eg, B9C0Eh, B9C0Ei, B9C0Ej, B10C0Eg, B10C0Eh,  
1185       B10C0Ei, B10C0Ej, B10C0Ek, B10C0El

1186 Bin 0 was excluded as it has substantial hadronic contamination and poor angular resolution.

1187 Background considerations and source selection was identical to Section 5.2, and no additional  
1188 arguments are provided here. Many of the HAWC systematics explored in Section 5.7 also apply  
1189 for this DM search and are not added upon here.

1190 **6.3 Analysis**

1191 The analysis and its systematics are almost identical to Section 5.3. Importantly, we use the  
1192 same Equation (7.1) and Equation (5.2) for estimating the gamma-ray flux at HAWC from our  
1193 sources. We add on to the previous study with a search for DM decay. The flux equations for DM  
1194 decay are

$$\frac{d\Phi_\gamma}{dE_\gamma} = \frac{1}{4\pi\tau m_\chi} \frac{dN_\gamma}{dE_\gamma} \times \int_{\text{source}} d\Omega \int_{l.o.s} \rho_\chi dl(r, \theta') \quad (6.1)$$

1195 with a new quantity, the  $D$  factor, defined as

$$D = \int d\Omega \int_{l.o.s} dl \rho_\chi(r, \theta') \quad (6.2)$$

1196 Software was written to accommodate DM decay from dSphs, however decay profiles were not  
1197 received from  $\mathcal{L}\mathcal{S}$  by the time of writing this thesis.

1198 **6.3.1  $\frac{dN_\gamma}{dE_\gamma}$  - Particle Physics Component**

1199 For these spectra, we import HDM with Electroweak (EW) corrections and additional correc-  
1200 tions for neutrinos above the EW scale [64]. The spectrum is implemented as a model script in  
1201 astromodels for 3ML. A comprehensive description of EW corrections and neutrino considerations  
1202 are provided later in [TODO: refeance MM nu duck](#).

1203 Figure 6.1 demonstrates the impact of changes from HDM on DM annihilation to W bosons.  
1204 A class in astromodels was developed to include HDM and is aptly named `HDMspectra` within  
1205 `DM_models.py`. The SM DM annihilation channels studied here are  $\chi\chi \rightarrow:$

1206  $e^+e^-, \mu^+\mu^-, \tau^+\tau^-, b\bar{b}, t\bar{t}, gg, W^+W^-, ZZ, c\bar{c}, u\bar{u}, d\bar{d}, s\bar{s}, \nu_e\bar{\nu}_e, \nu_\mu\bar{\nu}_\mu, \nu_\tau\bar{\nu}_\tau, \gamma\gamma, hh.$

1207 For  $\gamma\gamma$  and  $ZZ$ , a substantial fraction of the signal photons are expected to have total energy equal  
1208  $m_\chi$  [64]. This introduces a  $\delta$ -function that is much narrower than the energy resolution of the  
1209 HAWC detector. To ensure that this feature is not lost in the likelihood fits, the 'line' feature is  
1210 convolved with a Gaussian kernel with a  $1\sigma$  width of  $0.05 \cdot m_\chi$  and total kernel window of  $\pm 4\sigma$ .  
1211 This differs from HAWC's previous line study where 30% of HAWC's energy resolution was used  
1212 for the kernel [66]. The NN energy estimator's strength compared to  $f_{\text{hit}}$  at low gamma-ray energy

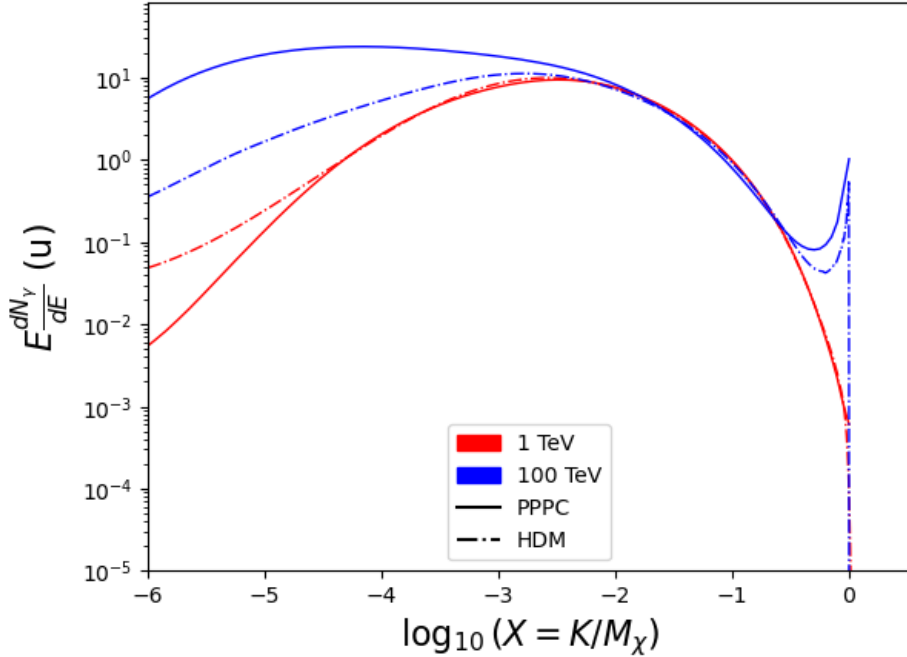


Figure 6.1 Difference between spectral hypotheses from PPPC [44] and HDM [64]. Shown is the expected DM annihilation spectrum for  $\chi\chi \rightarrow W^-W^+$ . Solid lines are spectral models with EW corrections from the PPPC. Dash-dot lines are spectral models from HDM. Red lines are models for  $M_\chi = 1$  TeV. Blue lines represent models for  $M_\chi = 100$  TeV.

enables smaller resolutions in addition to low energy tails in the spectral models [64].  $\chi\chi \rightarrow \gamma\gamma$  and  $ZZ$  spectral hypotheses are shown in Figure 6.2. Spectral models for the remaining annihilation channels are plotted for each  $m_\chi$  in Figure B.1.

### 6.3.2 $J$ and $D$ - Astrophysical Components

The J-factor profiles for each source are imported from Louis Strigari et al. (referred to with  $\mathcal{LS}$ ) [65]. Profiles in  $\frac{dJ}{d\Omega}(\theta)$  up to  $\theta = 0.5^\circ$  were provided directly from the authors. Map generation from these profiles were almost identical to Section 5.3.2 except that a higher order trapezoidal integral was used for the normalization of the square, uniformly-spaced map:

$$p^2 \cdot \sum_{i=0}^N \sum_{j=0}^M w_{i,j} \frac{d\mathcal{K}}{d\Omega}(\theta_{i,j}, \phi_{i,j}) \quad (6.3)$$

$\mathcal{K}$  is either  $J$  or  $D$  for the spatial distributions of annihilation or decay respectively.  $p$  is the angular side of one pixel in the map.  $w_{i,j}$  is a weight assigned the following ways:

$w_{i,j} = 1$  if  $(\theta_{i,j}, \phi_{i,j})$  is fully within the region of integration

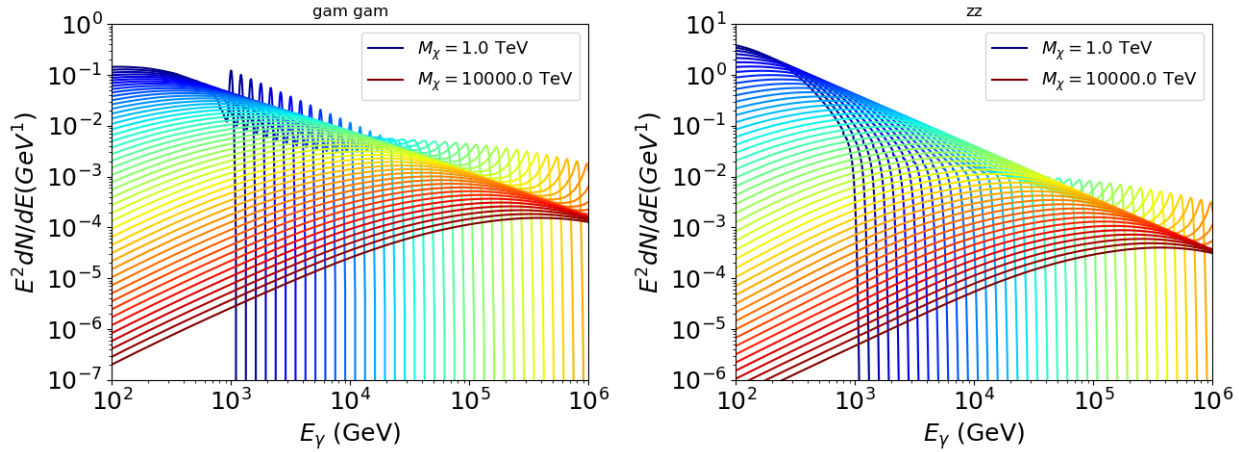


Figure 6.2 Photon spectra for  $\chi\chi \rightarrow \gamma\gamma$  (left) and  $\chi\chi \rightarrow ZZ$  (right) after Gaussian convolution of line features. Both spectra have  $\delta$ -features at photon energies equal to the DM mass. Bluer lines are annihilation spectra with lower DM mass. Redder lines are spectra from larger DM mass. All Spectral models are sourced from the Heavy Dark Matter models [64]. Axes are drawn roughly according to the energy sensitivity of HAWC.

1224        $w_{i,j} = 1/2$  if  $(\theta_{i,j}, \phi_{i,j})$  is on an edge of the region of integration

1225        $w_{i,j} = 1/4$  if  $(\theta_{i,j}, \phi_{i,j})$  is on a corner of the region of integration

1226   Figure 6.3 shows the median and  $\pm 1\sigma$  maps used as input for DM annihilation studied by  $\mathcal{LS}$ .

### 1227   **6.3.3 Source Selection and Annihilation Channels**

1228   HAWC's sources for this multithreaded analysis include Coma Berenices, Draco, Segue 1, and  
 1229   Sextans  $\mathcal{LS}$  observes up to 43 sources in its publication, however only 4 of the best fit profiles were  
 1230   provided at the time this thesis was written. A full description of each source used in this analysis  
 1231   is found in Table 6.1.

1232   This analysis improves on chapter 5 in the following ways. Previously, the particle physics  
 1233   model used for gamma-ray spectra from DM annihilation was from the PPPC [44] which missed  
 1234   important considerations relevant for the neutrino sector. HDM is used to account for this shortfall  
 1235   [64]. HDM also models DM to the Planck scale which permits HAWC to probe PeV scale DM.  
 1236   For this study, we sample DM masses: 1 TeV - 10 PeV with 6 mass bins per decade in DM mass.  
 1237   In the case of line spectra ( $\chi\chi \rightarrow \gamma\gamma$ , or  $ZZ$ ), we double the mass binning to 12 DM mass bins  
 1238   per decade in DM mass. A larger source catalog is used that uses a Navarro–Frenk–White (NFW)

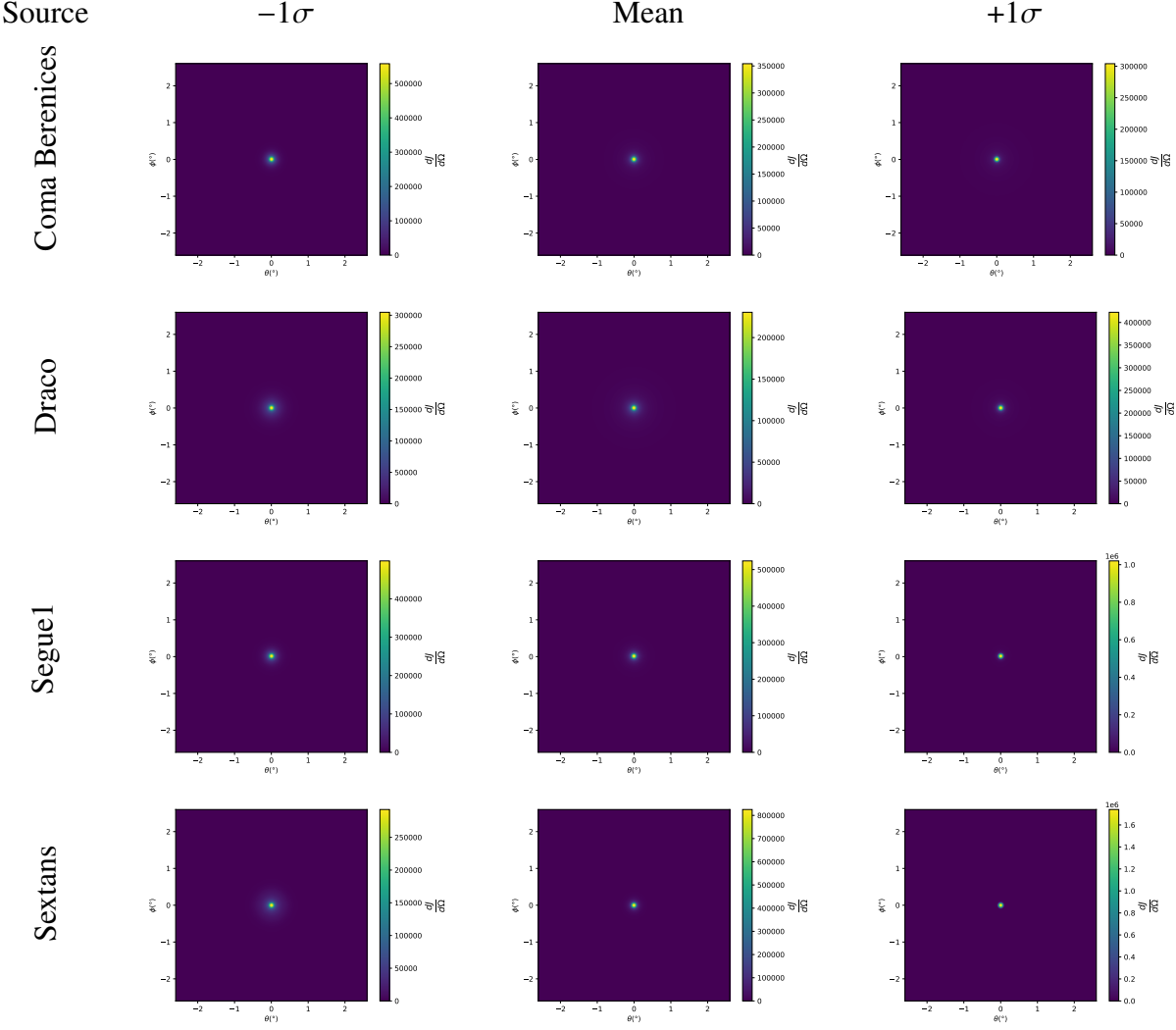


Figure 6.3  $\frac{dJ}{d\Omega}$  maps for Coma Berenices, Draco, Segue1, and Sextans. Columns are divided for the  $\pm 1\sigma$  uncertainties in  $dJ/d\Omega$  around the mean value from  $\mathcal{LS}$  [65]. Origin is centered on the specific dwarf spheroidal galaxies (dSph).  $\theta$  and  $\phi$  axes are the angular separation from the center of the dwarf

1239 spatial DM distribution from  $\mathcal{LS}$  [65]. Because NFW has fewer parameters than what is used  
 1240 for  $\mathcal{GS}$ ,  $\mathcal{LS}$  is able to fit ultra-faint dwarves, expanding the number of sources available for DM  
 1241 searches. Finally, the gamma-ray ray dataset is much larger. The study performed here analyzes  
 1242 2565 days of data compared to 1017 days analyzed in chapter 5.

## 1243 6.4 Likelihood Methods

1244 These are identical to Section 5.4.1 and no additional changes are made to the likelihood. Bins  
 1245 in this analysis are expanded to include HAWC’s NN energy estimator.

1246 **6.5 Computational Methods: Multithreading**

1247 Previously, as in Section 5.3, the likelihood was minimized for one model at a time. One  
 1248 model in this case representing a DM annihilation channel, DM mass, and dSph. In an effort  
 1249 to conserve human and CPU time, jobs submitted for high performance computing contained a  
 1250 list of DM masses to iterate over for likelihood fitting. Jobs were then trivially parallelized for  
 1251 each permutation of the two lists: CHANS (SM annihilation channel) and SOURCES (dSph spatial  
 1252 templates). The lists for CHANS and SOURCES are found in Section 6.3.1 and Table 6.1, respectively.  
 1253 Initially, 11 DM mass bins were serially sampled for one job defined by a [SM channel, dSph] set.  
 1254 Computing the likelihoods would take between 1.5 to 2 hrs, stochastically, for a job. We expect to  
 1255 compute likelihoods for data and 300 Poisson background trials. The estimated CPU time based on  
 1256 the above for all SM annihilation channels (17) and 25 sources (all  $\mathcal{LS}$  sources within HAWC's  
 1257 field of view) amounted to 127,925 jobs. In total, 1,407,175 likelihood fits and profiles would  
 1258 be computed for the 11 mass bins we wished to study. The estimated CPU time ranged between  
 1259 10k CPU days - 8k CPU days. Human time is more challenging to estimate as job allocation is  
 1260 stochastic and highly dependent on what other users are submitting, yet it is unlikely that all jobs  
 1261 would run simultaneously. Therefore, we can expect human time to be about as long as was seen  
 1262 in chapter 5 which was on the order of months to fully compute on a smaller analysis. A visual aid  
 1263 to describe how jobs were organized is provided in Figure 6.4.

Name	Distance (kpc)	$l, b$ ( $^{\circ}$ )	$\log_{10} J$ ( $\mathcal{LS}$ set) $\log_{10}(\text{GeV}^2 \text{cm}^{-5} \text{sr})$
Coma Berenices	44	241.89, 83.61	$19.00^{+0.36}_{-0.35}$
Draco	76	86.37, 34.72	$18.83^{+0.12}_{-0.12}$
Segue I	23	220.48, 50.43	$19.12^{+0.49}_{-0.58}$
Sextans	86	243.50, 42.27	$17.73^{+0.13}_{-0.12}$

Table 6.1 Summary of the relevant properties of the dSphs used in the present work. Column 1 lists the dSphs. Columns 2 and 3 present their heliocentric distance and galactic coordinates, respectively. Column 4 reports the  $J$ -factors of each source given from the  $\mathcal{LS}$  studies and estimated  $\pm 1\sigma$  uncertainties. The values  $\log_{10} J$  ( $\mathcal{LS}$  set) [65] correspond to the mean  $J$ -factor values for a source extension truncated at  $0.5^{\circ}$ .

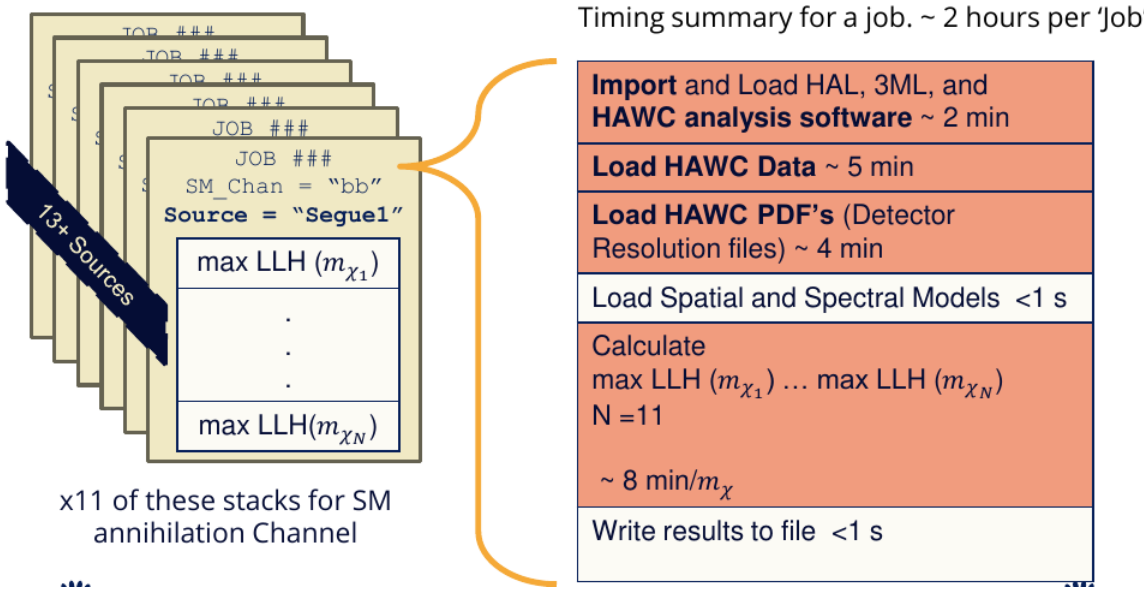


Figure 6.4 Infographic on how jobs and DM computation was organized in Section 5.3. Jobs were built for each permutation of CHANS and SOURCES shown by the left block in the figure. Each job, which took on the order 2 hrs to compute, had the following work flow: 1. Import HAWC analysis software, 2 min to run. 2. Load HAWC count maps, 5 min to run. 3. Load HAWC energy and spatial resolutions, 4 min. 5. Load DM spatial source templates and spectral models, less than 1 s. 6. Perform likelihood fit on data and model, about 8 min per DM mass. 7. Write results to file, less than 1s.

1264     The computational needs for this next generation DM analysis are extreme and is unlike other  
 1265     analyses performed on HAWC. It became clear that there was a lot to gain from optimizing how  
 1266     the likelihoods are computed. This section discusses how multi-threading was applied to solve and  
 1267     reduce HAWC’s computing of likelihoods for large parameter spaces like in DM searches.

### 1268     6.5.1 Relevant Foundational Information

1269     The profiling of the likelihood for HAWC is done via gradient descent where the normalization  
 1270     of Equation (7.1) (linearly correlated with  $\langle \sigma v \rangle$ ) is rescaled in the descent. Additionally, we sample  
 1271     the likelihood space for a defined list of  $\langle \sigma v \rangle$ ’s described in Section 5.4.2. The time to compute  
 1272     these values is not predictable or consistent because many variables can change across the full  
 1273     model-space. Comprehensively, these variables are:

- 1274         •  $m_\chi$  : DM rest mass
- 1275         • CHAN : DM SM annihilation channel.

1276 • SOURCE : dSph within HAWC's field of view. This involves a spatial template AND coordinate  
1277 in HAWC data.

1278 •  $\langle\sigma v\rangle$ : Effectively the flux normalization and free parameter in the likelihood fit.

1279 Therefore, we develop an asynchronous, functional-parallel coding pattern. Asynchronous mean-  
1280 ing that the instructions and computing within a function are independent and permitted to be out  
1281 of sync with sibling computations. Functional-parallel meaning that instructions are the subject of  
1282 parallelization rather than threading the likelihood computation. This is close to trivial parametriza-  
1283 tion seen in Figure 6.4 except that we seek to consolidate the loading stages (software, data, and  
1284 detector resolution loading). Reducing the total instances of loading stages and distributing access  
1285 to the reduced loads across multiple asynchronous threads is expected to reduce serial processing  
1286 time and the overhead implicit to each job in addition to saving human time.

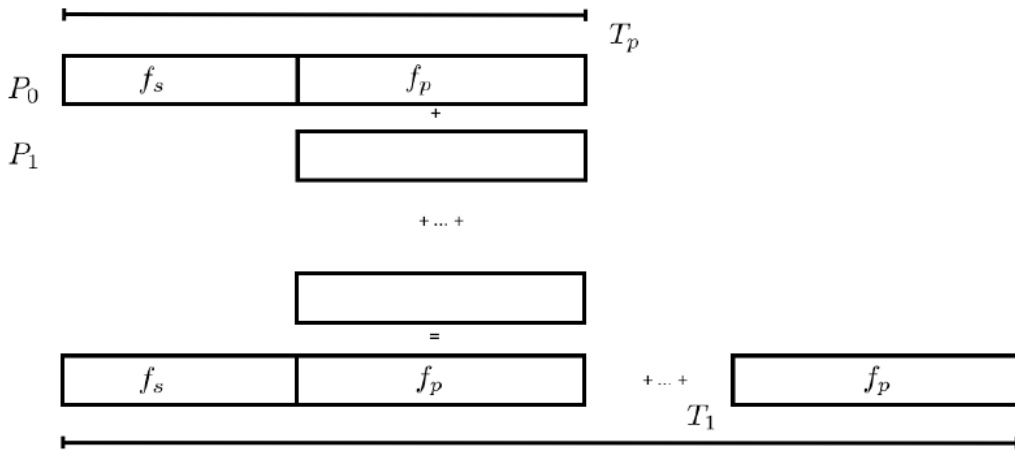


Figure 6.5 Graphic of Gustafson parallel coding pattern.  $f_s$  is the fraction of a program, in time, spent on serial computation.  $f_p$  is the fraction of computing time that is parallelizable.  $T_p$  is the total time for a parallel program to run.  $T_1$  is the total time for a parallel program to run if only 1 processor is allocated.  $P_N$  is the  $N$ -th processor where it's row is the computation the processor performs. The Gustafson pattern is most similar to what is implemented for this analysis. Figure is pulled from [67].

1287 We need a way to measure and compare the expected speedup and efficiency gain for this  
1288 asynchronous coding pattern. I pull inspiration for timing measurement from [67] and use *Amdahl's  
1289 law with hybrid programming*. Hybrid programming meaning that the computation is a mix of

1290 distributed and shared memory programming. If we assume the code is fully parallelizable over  $p$   
1291 processors and  $c$  threads, the ideal speedup is simply  $pc$  and ideal run-time is  $T_1/(pc)$ .  $T_1$  is the  
1292 total time for a parallel program to run if only 1 processor is allocated. However, the coding pattern  
1293 contains some amount of unavoidable serial computation, as shown in Figure 6.5. In our case, the  
1294 run time is estimated to be

$$T_{p,c} = \frac{T_1}{pc} (1 + F_s(c - 1)). \quad (6.4)$$

1295  $F_s$  is the fraction of CPU time dedicated to serial computation. The expected speedup is

$$S_{p,c} \equiv \frac{T_1}{T_{p,c}} = \frac{pc}{1 + F_s(c - 1)}. \quad (6.5)$$

1296 From Equation (6.5), we can see that the speed-up scales with  $p/F_s$ . We are free to minimize  
1297  $F_s$  asymptotically by enlarging the total models that are submitted to the thread pool, thereby  
1298 shrinking the CPU fraction dedicated to serial operation. We are also free to define exactly how  
1299 many threads and processors we utilize, yet eventually hit a hard cap at the hardware available on  
1300 our computing cluster. HAWC uses Intel Xeon processors with 48 cores and 96 threads. This  
1301 means when N-threads ( $c$ ) are defined,  $N \bmod 2$  cores ( $p$ ) are needed. We see that a successful  
1302 code scales well as the expected speedup is inversely correlated with  $F_s$ . As the total number of  
1303 models sampled grows, the speedup will also.

### 1304 6.5.2 Implementation

1305 The multithreaded code was written in Python3 and is documented in the `dark_matter_hawc`  
1306 [repository](#) within the script named `mpu_analysis.py`. A version of the script as of April 25  
1307 **TODO: make sure to update on this date** is also provided in Section B.2 It has many dependencies  
1308 including the HAWC analysis software. Figure 6.6 displays the workflow of a job with 3 threads.  
1309 Within a job, SOURCE is kept fixed . CHAN(S) remains 17 elements long. More  $m_\chi$  are sampled  
1310 from 11 bins up to 49 (for  $\gamma\gamma$  and ZZ) and 25 (for remaining CHANS) which amounts to 12 or 6  
1311 mass bins per decade. The DM mass,  $m_\chi$ , and SM annihilation channels, CHANS, are permuted into  
1312 a 473 element list which is split evenly across N threads where N ranges between 5 - 16. Within a  
1313 thread, for each  $m_\chi$ -CHAN tuple, 1001  $\langle\sigma v\rangle$  values are sampled in the likelihood, and the value of

Timing summary for a multi-threaded job.

Import and Load HAL, 3ML, and <b>HAWC analysis software</b> ~ 2 min		
Load HAWC Data ~ 5 min		
Load HAWC PDF's (Detector Resolution files) ~ 4 min		
Load Spatial Model < 1s		
Load Spectra Models <1 s	Load Spectra Models <1 s	Load Spectra Models <1 s
Calculate max LLH (Chan_0, $m_{\chi_1}$ ) ... max LLH (Chan_?, $m_{\chi_N}$ ) N = TOTAL/N_THREADS  ~ 8 min/Spec_model	Calculate max LLH (Chan_?, $m_{\chi_1}$ ) ... max LLH (Chan_?, $m_{\chi_N}$ ) N = TOTAL/N_THREADS  ~ 8 min/Spec_model	Calculate max LLH (Chan_?, $m_{\chi_1}$ ) ... max LLH (Chan_?, $m_{\chi_N}$ ) N = TOTAL/N_THREADS  ~ 8 min/Spec_model
Write results to file <1 s	Write results to file <1 s	Write results to file <1 s
Join Threads and terminate < 1s		

Figure 6.6 Task chart for one multithreaded job developed for this project. Green blocks indicate a shared resource across the threads AND computation performed serially. Red blocks indicate functional parallel processing within each thread. 3 threads are represented here, yet many more can be employed during the full analysis. Jobs are defined by the SOURCE as these require unique maps to be loaded into the likelihood estimator. The  $m_{\chi}$ , CHAN, and  $\langle \sigma v \rangle$  variables are entered into the thread pool and allocated as evenly as possible across the threads.

- 1314  $\langle \sigma v \rangle$  that maximizes the likelihood is found. Although rare, fits that failed are handled on a case  
 1315 by case basis.

### 1316 6.5.3 Performance

M Tasks	$T_{p,c}$ (hr:min:s)			
	$T_{1,1}$	$T_{1,2}$	$T_{1,8}$	$T_{1,16}$
50	1:40:37.5	0:52:43.7	0:19:13.8	0:13:44.0
74	2:22:30.0	1:15:00.6	0:25:21.3	0:15:49.8
100	(3:07:51.9)	1:40:10.5	0:30:44.4	0:20:01.4
200	(6:02:20.6)	-	1:00:32.0	0:30:35.0
473	(13:58:40.3)	-	<b>TODO: run this</b>	1:07:53.2

Table 6.2 Timing summaries for analyses for serial and multithreaded processes. M tasks is the number of functional-parallel tasks ran for the computation.  $T_{p,c}$  is a single run time in hours:minutes:seconds for runs utilizing  $p$  nodes and  $c$  threads. Runs are run interactively on the same computer to maximize consistency. Empty entries are indicated with '-'. (·) entries are estimated entries extrapolated from data earlier in the column.

- 1317 We see a tremendous reduction to human time waiting for our dSph analyses to run. Table 6.2

1318 shows the timing summaries for analyses of different sizes and thread counts. Additionally, the  
 1319 efficiency gained when consolidating the serial loading of data is also apparent in our ability to  
 1320 study many more tasks in about the same amount of wall time as a smaller serial computation. Trials  
 1321 represented in the table were run on an AMD Opteron® processor 6344 with 48 cores, 2 threads  
 1322 per core; 2.6 GHz clock. This is not the same architecture used for analysis on the computing  
 1323 cluster however they are similar enough that results shown here are reasonably representative of  
 1324 computing on the HAWC computing cluster. I use the Tab. 6.2 for the inferences and conclusions  
 1325 in the following paragraphs.

1326 First, we want to find  $T_s$ , the time of serial computation. From Fig. 6.5, the timing for our  
 1327 coding pattern can be written as

$$T_s + Mt_p = T_{1,1}^M. \quad (6.6)$$

1328  $M$  is the number of functional-parallel tasks (represented as column 1 of Tab. 6.2), and  $t_p$  is the  
 1329 average time to complete a single parallel task.  $T_{1,1}^M$  is the total time for a parallel program to run if  
 1330 only 1 processor is allocated for  $M$  parallel task. With two runs of different  $M$  ( $M1$  and  $M2$ ), we  
 1331 can use a system of equations to derive

$$T_s = T_{1,1}^{M1} - M1 \left( \frac{T_{1,1}^{M1} - T_{1,1}^{M2}}{M1 - M2} \right). \quad (6.7)$$

1332 We also extract  $t_p$  using the same methods:

$$t_p = \frac{T_{1,1}^{M1} - T_{1,1}^{M2}}{M1 - M2}. \quad (6.8)$$

1333 From Tab. 6.2, we set  $M1 = 50$  and  $M2 = 74$  and take their corresponding  $T_{1,1}$  from the table to  
 1334 calculate  $T_s$  and  $t_p$ .

$$T_s = 803.1\text{s} \text{ and } t_p = 104.6\text{s} \quad (6.9)$$

1335 Now, we have specific estimation for the fraction of serial computing time,  $F_s$ :

$$F_s = \frac{803.1}{803.1 + 104.6 \cdot M}. \quad (6.10)$$

1336 The maximum  $M$  for this study is 473 which evaluates using Eq. (6.10):  $F_s = 0.016$  or 1.6% of  
 1337 computing time. Table 6.3 shows the resulting speedups.

M Tasks	$F_s$	$S_{1,2}$	$S_{1,8}$	$S_{1,16}$
50	1.33 E-1	1.90 [1.76]	5.23 [4.14]	6.35 [5.34]
74	9.40 E-2	1.90 [1.83]	5.62 [4.82]	9.00 [6.64]
100	7.13 E-2	1.88 [1.87]	6.11 [5.34]	9.38 [7.73]
200	3.70 E-2	- [1.93]	5.98 [6.36]	11.85 [10.29]
473	1.60 E-2	- [1.97]	[7.20]	12.35 [12.91]

Table 6.3 Speed up summaries for analyses for serial and multithreaded processes. M tasks is the number of functional-parallel tasks ran for the computation.  $S_{p,c}$  is a single speedup comparison for runs utilizing  $p$  nodes and  $c$  threads. [·] are the estimated speedups calculated from Tab. 6.2, Eq. (6.10), and Eq. (6.5). Empty entries are indicated with '-'.

1338 We see a speedup that generally exceeds expectations from Eq. (6.5) for real trail runs. We also  
 1339 see that there are diminishing returns as the number of threads increases. For small jobs with large  $c$ ,  
 1340 both the expected and observed speedup are significantly smaller than  $c$ . One thing not considered  
 1341 in Eq. (6.5) is the time incurred via communication latency. Communication latency increases  
 1342 with the number of threads and contributes to diminishing returns. Additionally, these values are  
 1343 for single runs and do not consider the stochastic variation expected in a shared high performance  
 1344 computing resource. Therefor, these results are not strictly conclusive, yet demonstrate the merits  
 1345 of multi-threading. We see very clearly that there is a lot to gain, and this new coding pattern will  
 1346 expand HAWC's analysis capabilities.

1347 **6.6 Analysis Results**

1348 3 of the 43  $\mathcal{LS}$  dSphs considered for the multithreaded analysis. These dSph are analyzed for  
 1349 emission from DM annihilation according to the likelihood method described in Section 5.4. The 3  
 1350 likelihood profiles are then stacked to synthesize a combined limit on the dark matter cross-section,  
 1351  $\langle\sigma v\rangle$ . This combination is done for the 17 SM annihilation channels. Figure 6.7 and Fig. 6.8 show  
 1352 the combined limits for all annihilation channels with HAWC's observations. Test statistics of the  
 1353 best fit  $\langle\sigma v\rangle$  values for each DM mass and SM annihilation channels are shown in Fig. 6.9 and  
 1354 Fig. 6.10. We also compare these limits to HAWC's Glory Duck limits shown in Section 5.5. The  
 1355 comparison to Glory Duck are featured in Fig. 6.11 for all the DM annihilation channels studied  
 1356 for Glory Duck. A full comparison is provided in the appendix in Fig. B.2, Fig. B.3, and Fig. B.4.  
 1357 Here, we show updated limits for  $\chi\chi \rightarrow b\bar{b}, e\bar{e}, \mu\bar{\mu}, \tau\bar{\tau}, t\bar{t}, W^+W^-$ ,  $\gamma\gamma$  and  $ZZ$ . For the first time

ever, we show limits for  $\chi\chi \rightarrow c\bar{c}$ ,  $s\bar{s}$ ,  $u\bar{u}$ ,  $d\bar{d}$ ,  $\nu_e\bar{\nu}_e$ ,  $\nu_\mu\bar{\nu}_\mu$ ,  $\nu_\tau\bar{\nu}_\tau$ ,  $gg$ , and  $hh$ .

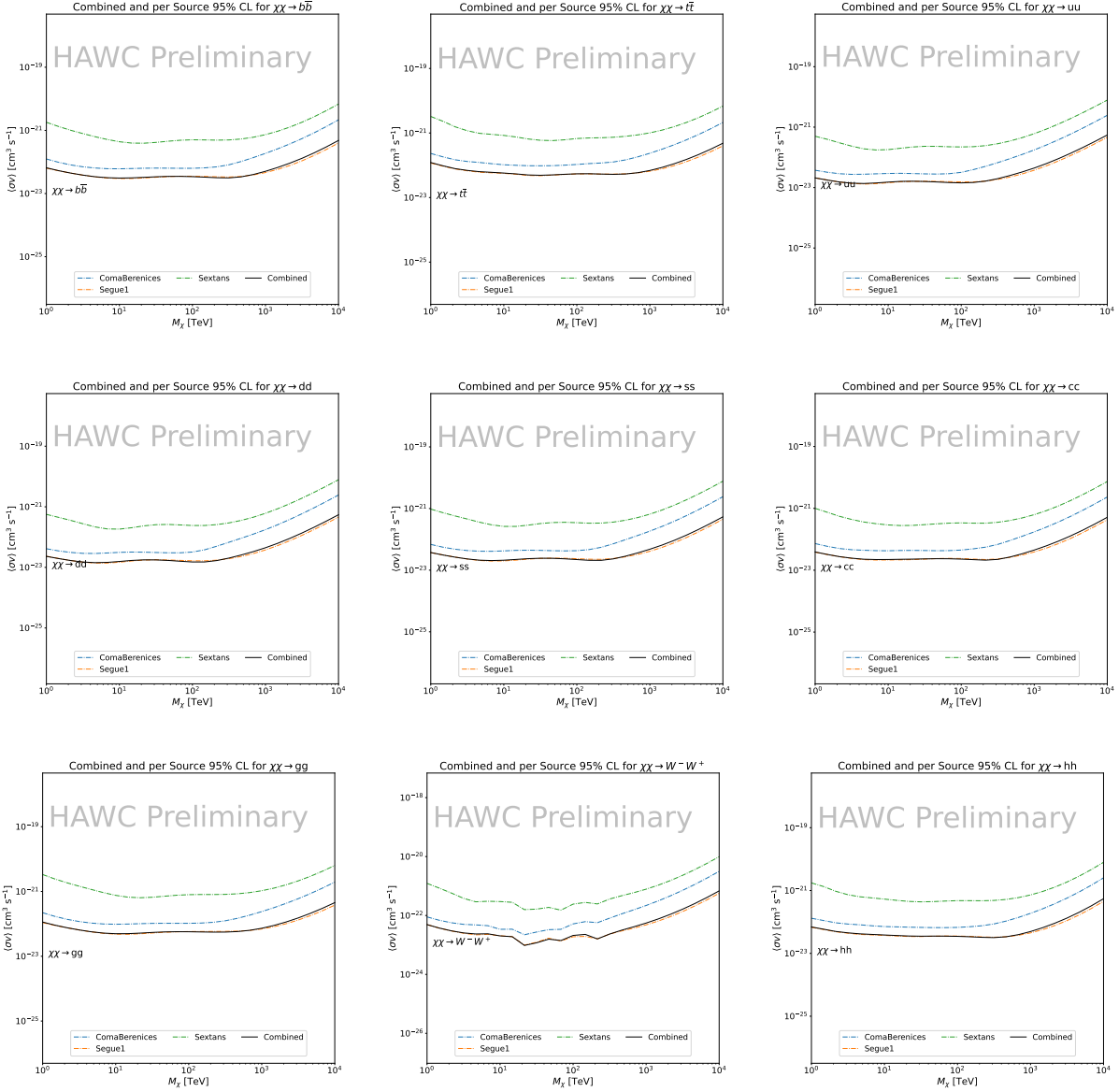


Figure 6.7 HAWC upper limits at 95% confidence level on  $\langle\sigma v\rangle$ versus DM mass for  $\chi\chi \rightarrow b\bar{b}$ ,  $t\bar{t}$ ,  $u\bar{u}$ ,  $d\bar{d}$ ,  $s\bar{s}$ ,  $c\bar{c}$ ,  $gg$ ,  $W^+W^-$ , and  $hh$ . Limits are with  $\mathcal{LS}$   $J$ -factors [65]. The solid line represents the observed combined limit. Dashed lines represent limits from individual dSphs.

No DM was found in HAWC observations. The largest excess found in HAWC data was for DM annihilating to  $W$ -bosons for  $m_\chi = 10 \text{ TeV}$  at  $2\sigma$ . HAWC's limits and excesses are dominated by Segue1. Coma Berenices shows excess at higher DM mass, yet no similar excesses were observed in Segue1. Sextans did not contribute significantly to signal excess or the combined limit as it is

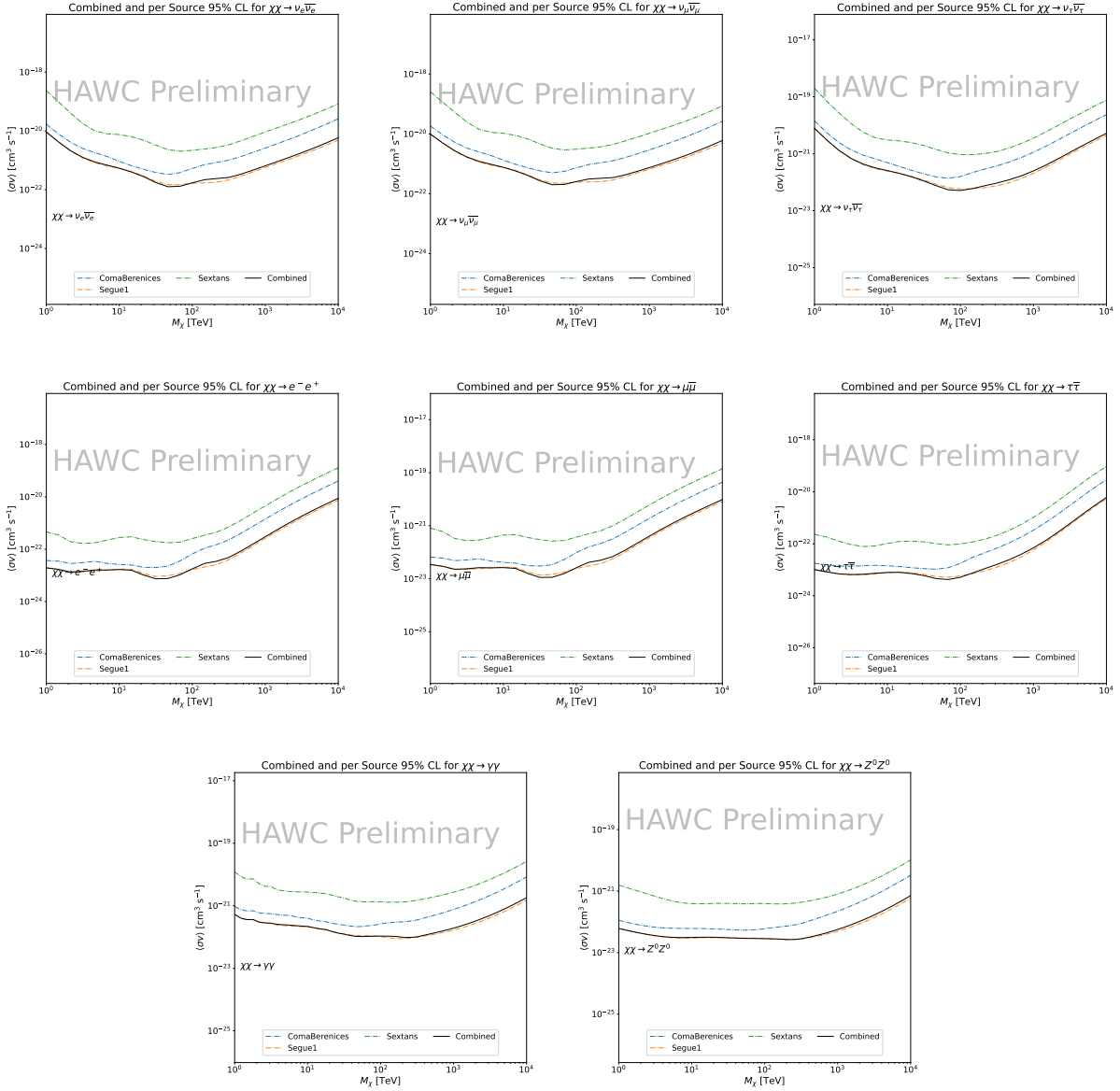


Figure 6.8 HAWC upper limits at 95% confidence level on  $\langle\sigma v\rangle$  versus DM mass for  $\chi\chi \rightarrow \nu_e \bar{\nu}_e$ ,  $\nu_\mu \bar{\nu}_\mu$ ,  $\nu_\tau \bar{\nu}_\tau$ ,  $e^- e^+$ ,  $\mu \bar{\mu}$ ,  $\tau \bar{\tau}$ ,  $\gamma \gamma$  and  $ZZ$ . Limits use  $\mathcal{L}S J$  factors [65]. The solid line represents the observed combined limit. Dashed lines represent limits from individual dSphs.

at high zenith. Draco was not included as the PDF of some of our analysis bins were wider than what is reasonable for a point source analysis. Draco is at a high zenith for HAWC, so the effort required to include it was not justified by the benefits.

We were not able to generate background trials in time of writing this thesis. These are not shown and are an immediate next step for this analysis before publication.

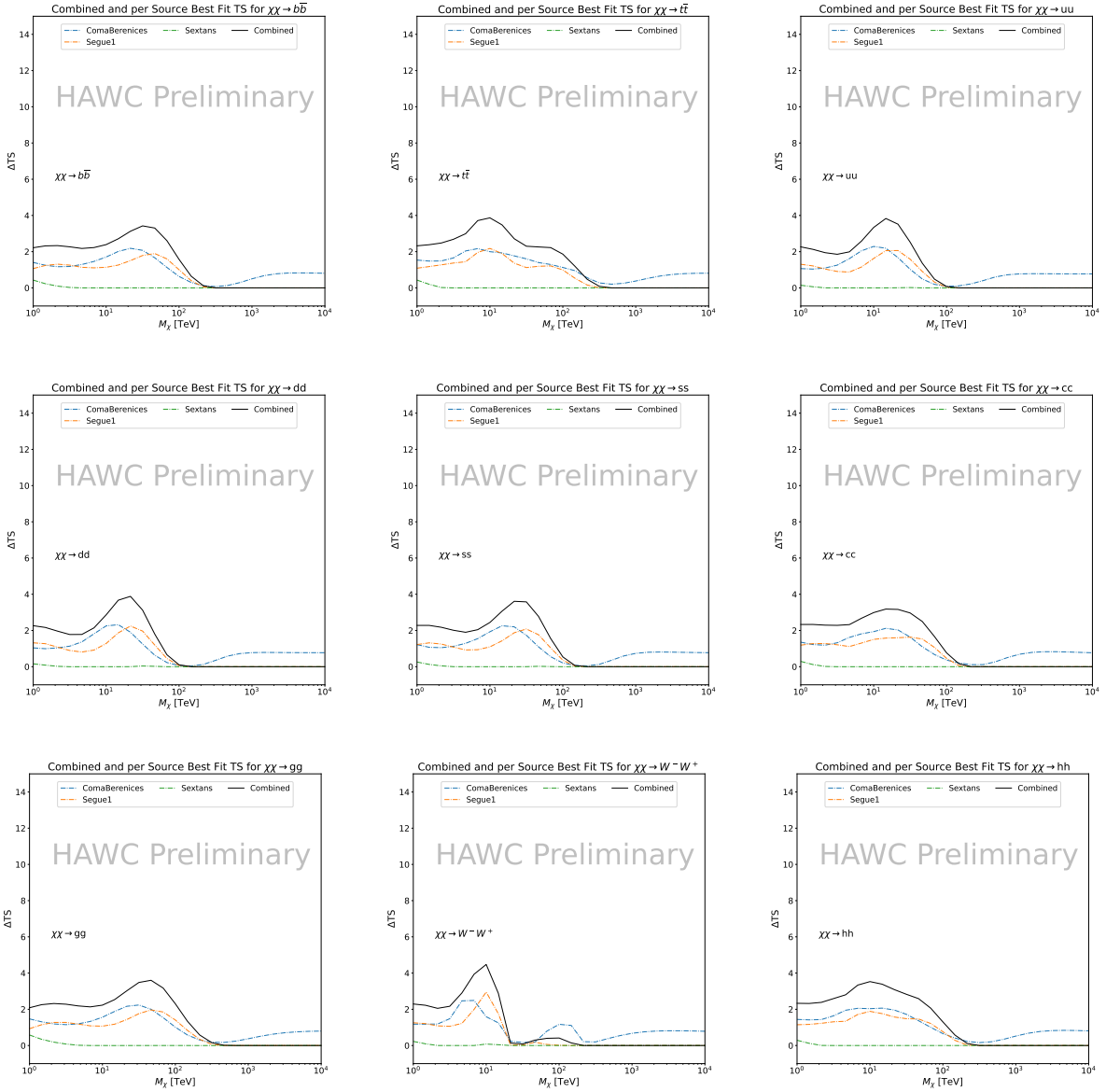


Figure 6.9 HAWC TS values for best fit  $\langle\sigma v\rangle$  versus  $m_\chi$  for SM annihilation channels:  $\chi\chi \rightarrow b\bar{b}$ ,  $t\bar{t}$ ,  $u\bar{u}$ ,  $d\bar{d}$ ,  $s\bar{s}$ ,  $c\bar{c}$ ,  $gg$ ,  $W^-W^+$ , and  $hh$ . Limits use  $\mathcal{L}\mathcal{S} J$  factors. The solid black line shows the combined best fit TS values. The colored, dashed lines are the TS values from each dSph.

When comparing these results to Section 5.5, we see an overall decrease to the confidence limit therefore improvement to HAWC's expected sensitivity. This improvement is generally stronger than a doubling of data, or a factor  $\sqrt{2}$  decrease. The comparison is somewhat complex and dependent on the dSph and SM annihilation channel. Figure 6.11 shows the comparisons of limits calculated for this analysis and Glory Duck (Section 5.5). Segue 1 and Coma Berenices are low

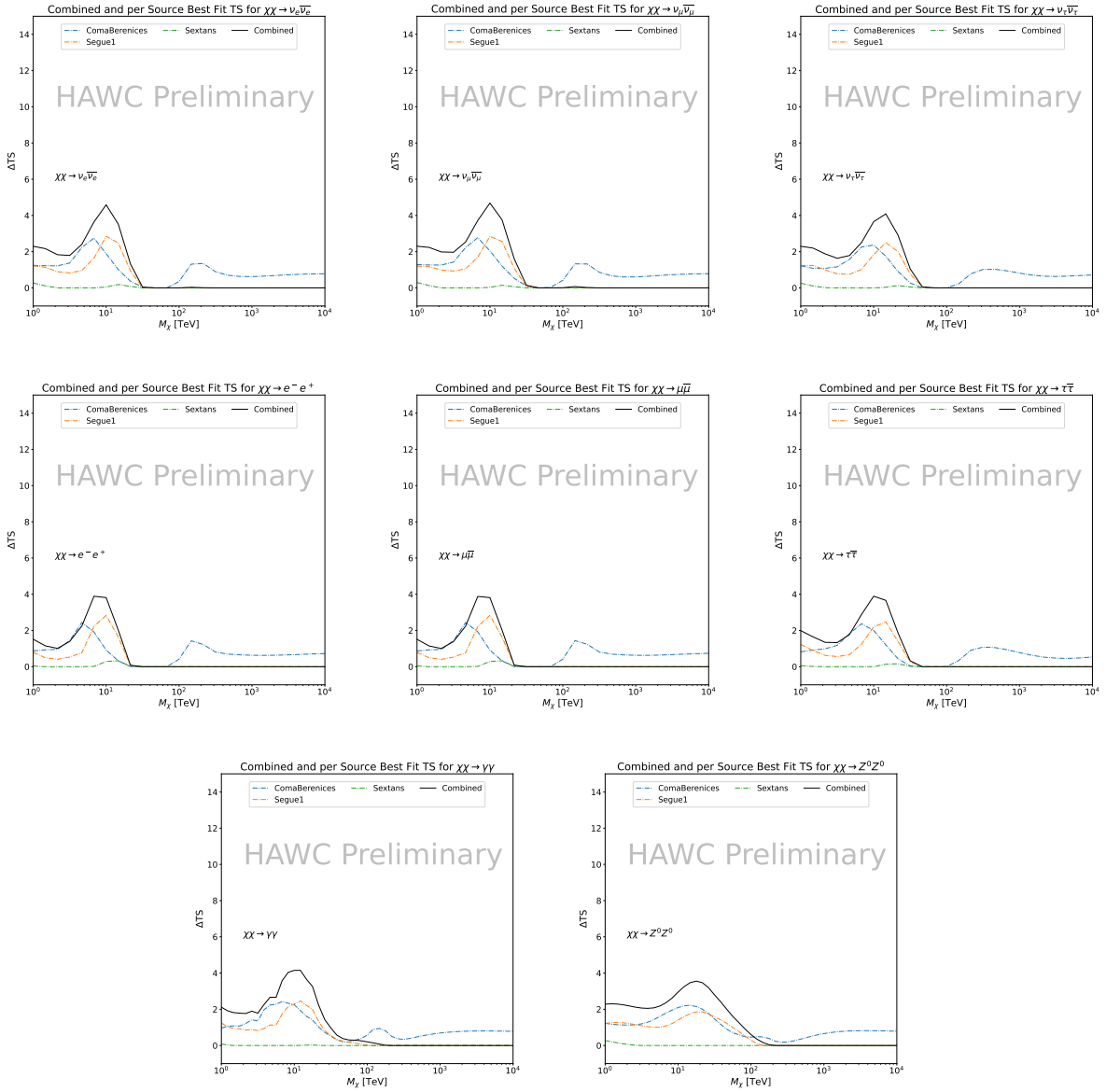


Figure 6.10 HAWC TS values for best fit  $\langle\sigma v\rangle$  versus  $m_\chi$  for SM annihilation channels:  $\chi\chi \rightarrow \nu_e \bar{\nu}_e$ ,  $\nu_\mu \bar{\nu}_\mu$ ,  $\nu_\tau \bar{\nu}_\tau$ ,  $e^- e^+$ ,  $\mu \bar{\mu}$ ,  $\tau \bar{\tau}$ ,  $\gamma\gamma$  and  $ZZ$ . Limits use  $\mathcal{L}\mathcal{S} J$  factors. The solid black line shows the combined best fit TS values. The colored, dashed lines are the TS values from each dSph.

zenith where improvements to HAWC's analysis come only from energy estimation. Differences between these two are dominantly from their differences in  $J$ -factor, half-light radii of the dSphs, and the particle physics inputs. Substantial gains in HAWC's analysis methods (pass 5.F) were made at high zenith which is important for sources like Sextans. The HDM particle physics model produces almost identical spectra to the PPPC for  $\chi\chi \rightarrow e^- e^+$ , so can be used to compare limits

1378 between dSph. Overhead sources see minimal improvement to the limits, while high zenith sources  
1379 see an order of magnitude improvement for all DM masses. Softer SM annihilation channels see  
1380 broad improvements to the limit compared to harder channels.

1381 **6.7 Systematics**

1382 These are identical to what was performed earlier in Glory Duck, Section 5.7. We are also  
1383 sensitive to the choice in spatial template, and this was explored in Section 5.7.2 and Section 5.8.2.

1384 **6.8 Conclusion and Discussion**

1385 In this multithreaded analysis, we have used observations of 3 dSphs from HAWC to perform  
1386 a collective DM search for annihilation signals. The data were combined across sources to signifi-  
1387 cantly increase the sensitivity of the search. Advanced computational techniques were deployed to  
1388 accelerate wall-time spent analyzing by an order of magnitude. We have observed no significant  
1389 deviation from the null, no DM, hypothesis, and so present our results in terms of upper limits on  
1390 the annihilation cross-section for seventeen potential DM annihilation channels across four decades  
1391 of DM mass.

1392 This analysis serves as a proof of concept for multithreaded HAWC analyses with large parameter  
1393 spaces. Larger datasets with fast techniques will be essential to tackling the DM problem. The  
1394 models we used for this study include annihilation channels with neutrinos in the final state.  
1395 Advanced studies could aim to merge our results with those from neutrino observatories with large  
1396 data sets.

1397 A full HAWC analysis will include systematic studies of the  $J$ -factor distributions. Additionally,  
1398 because of the timing reduction, the study can be doubled in size to include DM decay. We have no  
1399 yet received the remaining spatial profiles to the  $\mathcal{L}\mathcal{S}$  catalog, and limits can be quickly computed  
1400 once these are received. Finally, statistical studies with Poisson variation of HAWC’s background  
1401 are essential to a comprehensive understanding of our observed excesses.

Segue1

Coma Berenices

Sextans

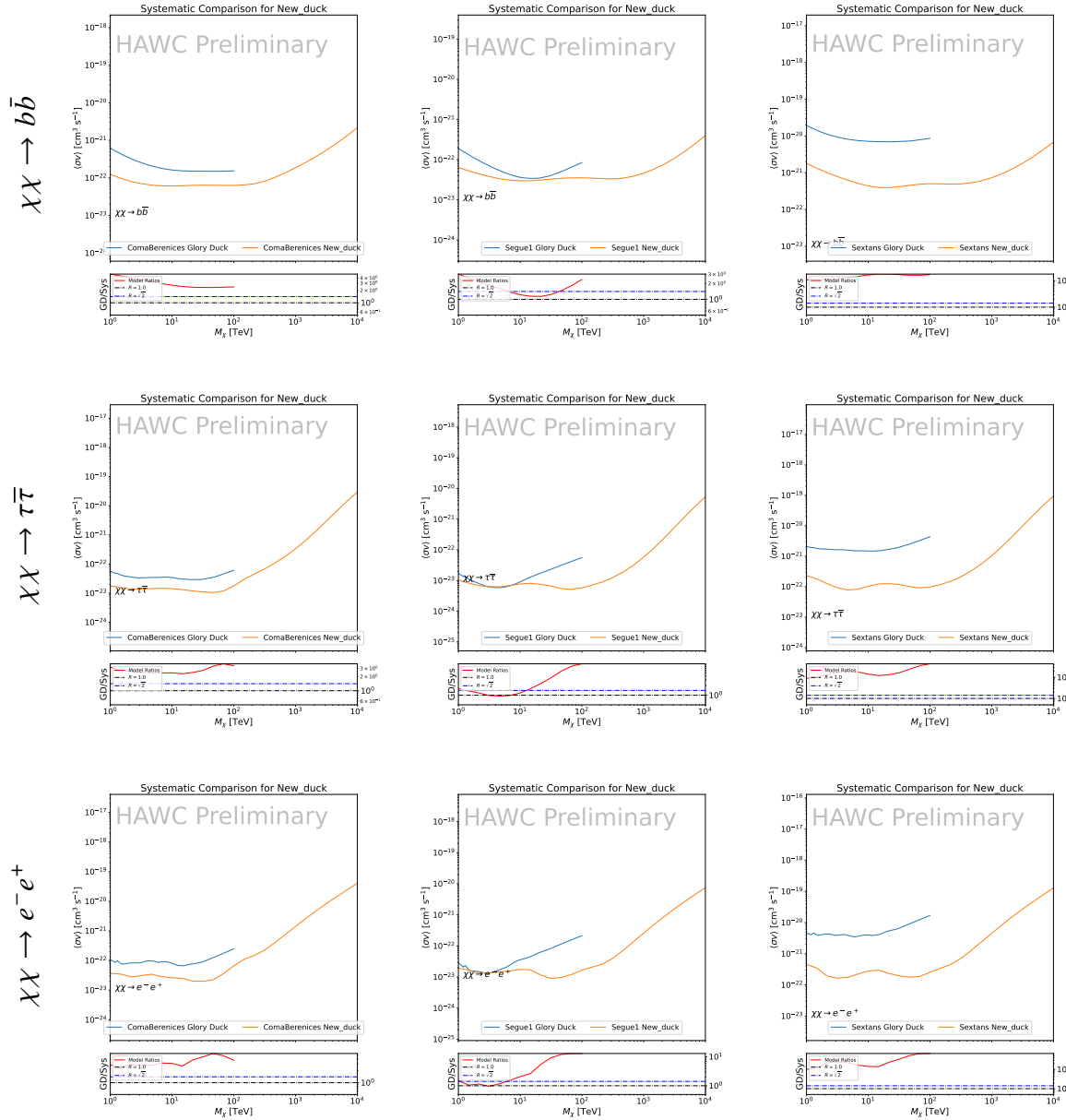


Figure 6.11 Comparison of HAWC limits from this analysis to Glory Duck (Fig. 5.5) for 3 dSphs and 3 SM annihilation channels:  $b\bar{b}$ ,  $\tau\bar{\tau}$ , and  $e\bar{e}$ . Each sector shows the 95% confidence limit from Glory Duck (blue line) and this analysis (orange line) in the top plot. The lower plot features the ratio in log scale of Glory Duck to this analysis in a red solid line. Horizontal dashed lines are for ratios of 1.0 (black) and  $\sqrt{2}$  (blue). Ratios larger than 1.0 are for limits smaller, or stricter, than Glory Duck. Ratios larger than  $\sqrt{2}$  indicates limits are stricter than a simple doubling of the Glory Duck data.

## CHAPTER 7

### 1402 HEAVY DARK MATTER ANNIHILATION SEARCH WITH ICECUBE'S NORTH SKY 1403 TRACK DATA

#### 1404 7.1 Introduction

1405 Neutrinos are another astrophysical messenger than can travel long distances without interaction.  
1406 Uniquely, they interact less readily than photons especially above PeV energies. Neutrinos thereofre  
1407 provide another window through which we can perform dark matter searches. Neutrinos come in  
1408 three flabors and so this triples the multiplicity of the particles we are searching for.

1409 Icecube has not done a DM annihilation analysis towards dwarf galaxies for a while. **TODO:**  
1410 [cite 2013 paper](#). This is in spite of the potentially crucial sensitivity afforded from neutrino spectral  
1411 lines [TODO: cite dan hooper and neutrino lines](#). A lot has changed in IC3 since that last analysis (we  
1412 have more strings, we have much more sophisticated analysis methods, and the theory modeling  
1413 has made significant leaps.) Therefore it is time to finally do a DM search toward dSphs. The hope  
1414 is that by laying down the important statistical foundation as well, that this work can be meshed  
1415 with gamma-ray data. IceCube is sensitive to annihilating DM to the DM ranges above 1 TeV  
1416 and can produce competitive results relative to gamma ray observatories in spectral models that  
1417 produce sharp neutrino features. The goal of this analysis is to perform a DM annihilation search  
1418 using the new datasets NST. The search will only be towards dwarf spheroidal galaxies (dSph).  
1419 These sources are known for their low backgrounds and high DM contents. Since the dataset is  
1420 sensitive to the north and south, as many dSph as possible will be included. Additionally, with  
1421 annihilation, these sources can be treated as point sources with little loss to sensitivity or model  
1422 dependence on how the DM is distributed. DM masses from 500 GeV to 100 PeV are considered  
1423 for this analysis. All standard model annihilation channels available from the HDMspectra are  
1424 studied in this analysis.

1425 Additional work is done to extract the Likelihood profiles for each DM, source hypothesis so  
1426 that these data can be combined with gamma-ray observatories. This work is considered a separate  
1427 project as the statistical treatment is unique from many IceCube analyses. The wiki for [ the

1428 combined analysis] **TODO: instead point to chapter**This chapter presents the analysis work for  
1429 IC3 for DM searches toward dSphs. This section describes the various steps and features of the  
1430 analysis. It is structure first introduces the data and how it is treated, then systematic studies of the  
1431 dwarves individually. Finally, the stacked analysis and results are presented.

## 1432 **7.2 Dataset and Background**

1433 This section enumerates the data and background methods used for IceCube's study of dSphs.  
1434 Section 7.2.1 and Section 7.2.2 are most useful for fellow IceCube collaborators looking to replicate  
1435 this analysis.

### 1436 **7.2.1 Itemized IceCube files**

- 1437 • Software Environment: CVMFS Py3-v4.1.1
- 1438 • Data Sample: Northern Tracks NY86v5p1
- 1439 • Analysis Software: csky ([nu\\_dark\\_matter](#))
- 1440 • Analysis wiki: [https://wiki.icecube.wisc.edu/index.php/Dark\\_Matter\\_Annihilation\\_Search\\_towards\\_dwarf\\_spheroidals\\_with\\_NST\\_and\\_DNN\\_Cascades](https://wiki.icecube.wisc.edu/index.php/Dark_Matter_Annihilation_Search_towards_dwarf_spheroidals_with_NST_and_DNN_Cascades)
- 1442 • Project repository

### 1443 **7.2.2 Software Tools and Development**

1444 This analysis was performed inside IceCube's CVMFS (3.4.1.1) software environment using  
1445 csky for likelihood calculations. Csky did not come with dark matter spectral models nor could  
1446 accomodate custom flux models. We developed these capacities for single source and stacked  
1447 source studies for this analysis. The analysis code is held in a separate repository from csky. The  
1448 [nu\\_dark\\_matter](#) branch of csky manages the input of custom dark matter spectra and accompanied  
1449 DM astrophysical source then calculates likelihoods with a selected data sample. The [IceCube Dark](#)  
1450 [Matter dSph repository](#) manages the generation of spectral models for neutrinos, physics parameter  
1451 extraction from  $n_{\text{sig}}$ ,  $J$ -factor per source inputs, and bookkeeping for the large parameter space.  
1452 The project repository required a secondary software environment for neutrino oscillations. How

1453 to launch and run those calculations are documented in the project repository and the Docker image  
1454 is additionally saved in Section C.1

1455 **7.2.3 Data Set and Background Description**

1456 For this analysis, I use the Northern Sky Tracks (NST) Sample (Version V005-P01). The sample  
1457 contains up-going track-like events, usually from  $\nu_\mu$  and  $\nu_\tau$  and has a superior angular resolution  
1458 compared to the cascade dataset. This sample covers 10.4 years of data (IC86\_2011-2021). The  
1459 accepted neutrino energy range used for the analysis is unique from most other IceCube searches  
1460 because DM spectra are very hard. The sampled energy range is  $1 < \log(E_\nu/\text{GeV}) < 9.51$  with  
1461 step size 0.125.

1462 The strength of a dwarf analysis is that there is no additional background consideration beyond  
1463 nominal, baseline background estimations. For NST, the nominal contribution comes from atmo-  
1464 spheric neutrinos and isotropic astrophysical neutrinos. We estimate the background by scrambling  
1465 NST data along Right Ascension.

1466 **7.3 Analysis**

1467 The expected differential neutrino flux from DM-DM annihilation to standard model particles,  
1468  $d\Phi_\nu/dE_\nu$ , over solid angle,  $\Omega$  is described by the familiar equation.

$$\frac{d\Phi_\nu}{dE_\nu} = \frac{\langle\sigma v\rangle}{8\pi m_\chi^2} \frac{dN_\nu}{dE_\nu} \times \int_{\text{source}} d\Omega \int_{l.o.s} \rho_\chi^2 dl(r, \theta') \quad (7.1)$$

1469 This is identical to past examples except that there are 3 neutrino flavors, so there are a corresponding  
1470 3 flux equations. Section 5.3 has a complete description of all the terms. Additionally, neutrinos  
1471 oscillate between flavors which needs to be considered for the expected neutrino flux at Earth.  
1472 Section 7.3.1 presents the particle physics model for DM annihilation. Section 7.3.2 presents the  
1473 spatial distributions built for each dSph.

1474 **7.3.1  $\frac{dN_\nu}{dE_\nu}$  - Particle Physics Component**

1475 Neutrino spectra from heavy dark matter annihilation were generated using HDMSSpectra [64]  
1476 and  $\chi$ arrov [68]. HDMSSpectra simulates the decay and annihilation of heavy dark matter, for  
1477 different dark matter masses and SM primary annihilation channels. The simulation includes

1478 electroweak radiative corrections and higher order loop corrections with quarks. This publication  
1479 also pushes the simulated DM mass to the Plank scale (1 EeV), however this study will not explore  
1480 that high.

1481 An important novel feature in the spectra is that neutrino line channels will be accompanied  
1482 with a low energy tail. Thus the earth will not fully attenuate a neutrino SM channel signal from  
1483 high declination sources where the neutrino flux must first traverse through the Earth. The SM  
1484 annihilation channels that feature lines include all leptonic channels. ( $\nu_{e,\mu,\tau}$ ,  $e$ ,  $\mu$ , and  $\tau$ ) We use  
1485 [Xarov](#) to propagate and oscillate the neutrinos from the source to Earth. Because these sources are  
1486 quite large in absolute terms, and also far (order 10 kpc or more), the resulting flavor spectra are  
1487 the averages of the transition probabilities [68]:

$$P(\nu_\alpha \rightarrow \nu_\beta) \approx \begin{bmatrix} 0.55 & 0.18 & 0.27 \\ 0.18 & 0.44 & 0.38 \\ 0.27 & 0.38 & 0.35 \end{bmatrix} \quad (7.2)$$

1488 When calculating the expected contribution to  $n_s$ , only  $\nu_\mu$ ,  $\nu_\tau$  are considered as NST's effective  
1489 area to  $\nu_e$  is essentially 0. With these consideration, the expected composite neutrino spectrum  
1490 is a average of the two flavors:  $(\nu_\mu + \nu_\tau)/2$ . The spectral tables are then converted to splines to  
1491 condense information, enable random sampling of the spectra, and enable faster computation times.  
1492 The spectral splines are finally implemented as a DM class in csky. Examples of the spectra before  
1493 and after propagation are shown in Fig. 7.1.

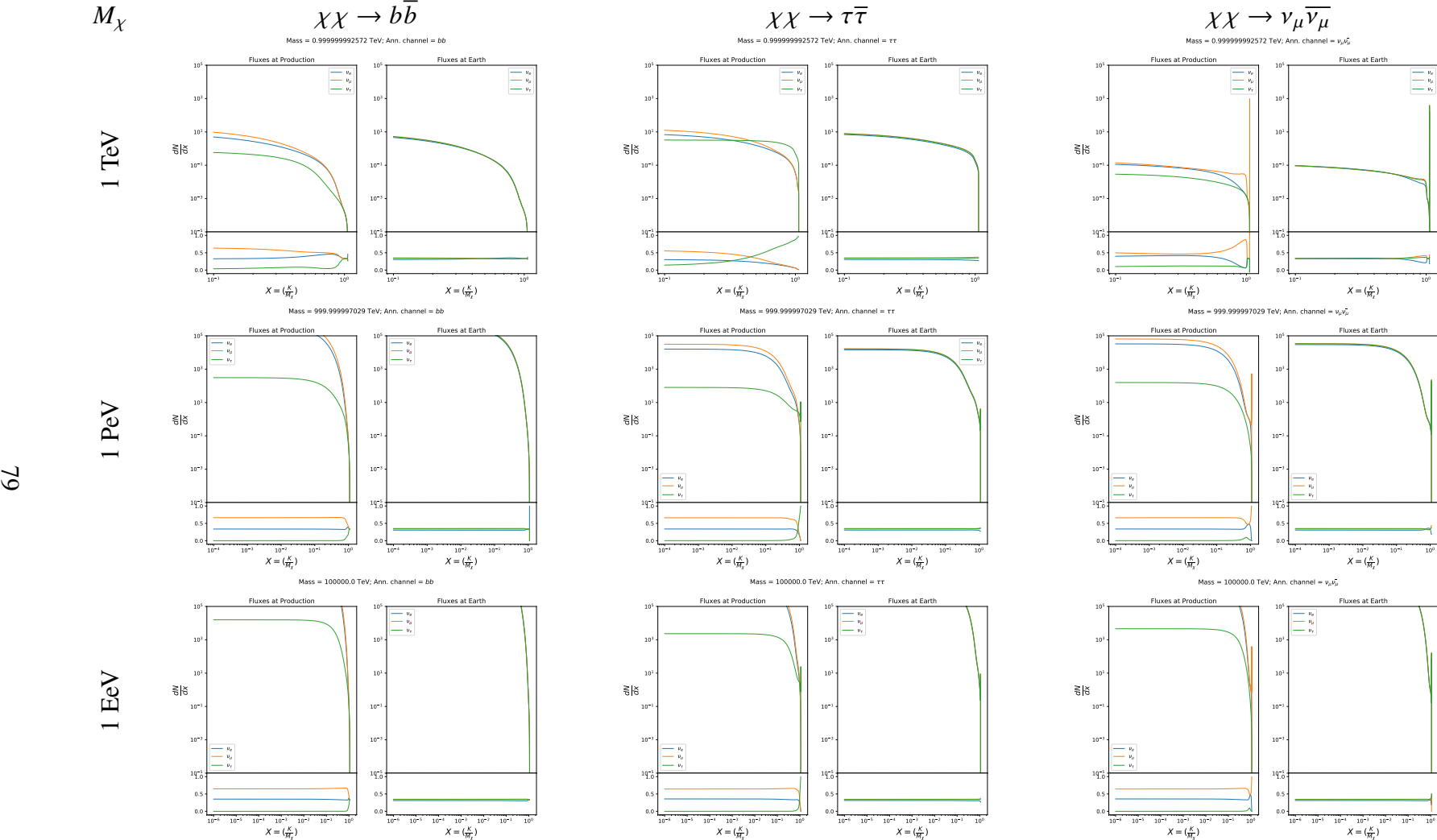


Figure 7.1 Neutrino spectra at production (left panels) and after oscillation at Earth (right panels). Blue, orange, and green lines are the  $\nu_e$ ,  $\nu_\mu$ , and  $\nu_\tau$  spectra respectively. Top panels show the spectra in  $\frac{dN}{dE}$ . Lower panels plot the flavor ratio to  $\nu_e + \nu_\mu + \nu_\tau$ . SM annihilation channels  $b\bar{b}$ ,  $\tau\bar{\tau}$ , and  $\nu_\mu \bar{\nu}_\mu$  are shown for  $M_\chi = 1$  PeV, TeV, and EeV.

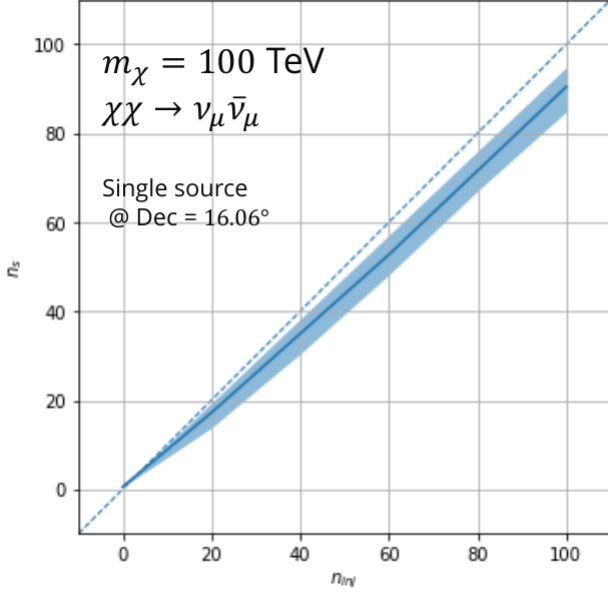


Figure 7.2 Signal recovery for 100 TeV DM annihilation into  $\nu_\mu \bar{\nu}_\mu$  for a source at Dec = 16.06°.  $n_{\text{inj}}$  is the number of injected signal events in simulation.  $n_s$  is the number of reconstructed signal events from the simulation. Although the uncertainties are small and tight, the reconstructed  $n_s$  are systematically underestimated.

#### 1494 7.3.1.1 Treatment of Neutrino Line Features

1495 All leptonic DM annihilation channels  $\chi\chi \rightarrow [\nu_{e,\mu,\tau}, e, \mu, \tau]$  develop a prominent and narrow  
 1496 spectral line feature. For all neutrino flavors, this line is visible and prominent in all mass models  
 1497 studied for this analysis. For charged leptons, the feature only really shows up at the larger DM  
 1498 mass models. Examples for lines in both neutrinos and charged leptons annihilation are provided  
 1499 in Fig. 7.1. This line feature is so narrow relative the sampled energy range that the MC rarely  
 1500 samples within the neutrino line. As a result, often the best fit to simulation of background will  
 1501 always floor to TS = 0 and the signal recovery tends to be conservative.

1502 To remedy this, a similar approach to the IceCube’s decay analysis [TODO: refer to Minjin’s](#)  
 1503 [page](#). 2 kernels were tested (Gaussian, uniform (flat)) to smooth out the line feature. The widths  
 1504 were tuned such that the signal recovery approached unity for DM mass 100 TeV to 1 PeV.  
 1505 Additionally, the tuning was performed only for a source at declination 16.06 (Segue 1). This is  
 1506 to avoid confusion loss in signal recovery from too narrow a line and from Earth’s attenuation of  
 1507 high energy neutrinos. The convolution also needed to as close as possible preserve the integrated  
 1508 counts of neutrinos. The optimized kernel window for all lines is summarized as:

- 1509 • Gaussian kernel w/ $2\sigma$  width =  $3.5E-3 \cdot m_\chi$
- 1510 • Minimum energy included in convolution =  $\text{MIN}[0.995 \cdot m_\chi, En(\nu_{line}) - 4\sigma]$
- 1511 • Maximum energy included in convolution =  $\text{MAX}[1.005 \cdot m_\chi, En(\nu_{line}) + 4\sigma]$

1512 where  $En(\nu_{line})$  is the neutrino energy where the neutrino line is at the maximum.

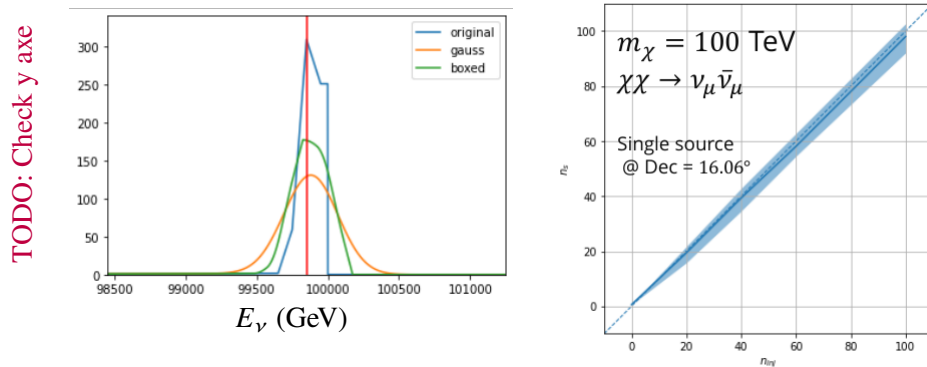


Figure 7.3 Top left panel shows the two kernels overlaid the original spectrum from Charon. delta I is the difference in the integral of the peaks with respect to the original spectrum. The vertical red line indicated where the original neutrino line is maximized. Lower right shows the signal recoveries of the DM model using the Gaussian kernel with parameters enumerated above.

1513 These parameters broadly improved the signal recovery of the line spectra. An example is  
1514 provided below. Signal recovery plots of the full analysis are provided much further down.

### 1515 7.3.1.2 Spline Fitting

1516 In an effort to reduce computational work, memory burden, and align with point source methods  
1517 used for NGC1068 and Seyfert analyses, spectral splines were created and adopted for estimating  
1518 the neutrino flux for the different annihilation. Software was written to generate, handle, and  
1519 calculate values on the splines. When using splines, one has to be careful of the goodness to fit.  
1520 There are critical caveats when testing the goodness to fit to MC generated above for all channels.

- 1521 • The splines must be Log10(\*) in Energy and dN/dE to account for the exponential nature of  
1522 the flux
- 1523 • The fidelity of the fit matters more at  $E_\nu \approx m_\chi$  where the model uncertainties are minimal  
1524 and physical considerations (like the cut-off) are most apparent.

- 1525     • The fidelity of the fit matters less at low  $E_\nu$  as the model uncertainties are large AND  
 1526       IceCube's sensitivity diminishes significantly below 500 GeV
- 1527     • Total integrated counts should be well preserved, however, the resolution of the MC is much  
 1528       higher than IceCube's energy resolution.
- 1529       – Meaning over several steps in E, the integral is preserved
- 1530       – the step size enters the cost function
- 1531       – Oscillating residuals, so long as they are very small and well centered, are not penalized
- 1532       as this gets averaged out.

1533     The resulting cost function to evaluate the goodness of fit was used to account for the above  
 1534     considerations.

$$e_i = x_i \cdot \left( \frac{dN_i}{dE_i} - 10^{\hat{e}_i} \right) \quad (7.3)$$

1535     Where  $\hat{e}_i$  is the spline estimator's value for  $x_i$ .  $x_i = E_{\nu_i}/m_\chi$ .  $\frac{dN_i}{dE_i}$  is the flux value from MC.

$$\text{err} = \sqrt{\frac{1}{x_{\max} - x_{\min}} \int_{x_{\min}}^{x_{\max}} e^2 dx} \quad (7.4)$$

1536     I then take the RMS of the error distribution and the resulting value (err) is used to evaluate  
 1537     the fidelity of the spectral spline. Each SM channel had different tolerances for 'err'. Channels  
 1538     with very hard cut-offs had looser tolerance for err because a lot of error would be generated from  
 1539     the cut-off being estimated to occur slightly early or late. Soft channels don't have this issue and  
 1540     therefore the tolerance is very strict. The table blow summarizes the tolerances for the SM channels.

1541  
 1542     The errors are then plotted in two ways. First, FAIL and OK are directly plotted with  $e_i$  as a  
 1543     function of x, and the full spline and MC. Second, a summary plot of all the splines is plotted and  
 1544     colors coded.

1545     Figure C.1 are the spline summaries and represent the current, up-to-date status of the splines.  
 1546     The goal broadly is to eliminate all red and inspect yellow.  $\nu_e$  is not considered in this analysis  
 1547     among the neutrino final states and so no work was done to converge the spline fits for this flavor.

$\chi\chi \rightarrow$	GOOD	OK	FAIL	Limits of err calc [ $X_{min}, X_{max}$ ]
$Z^0 Z^0, W^+ W^-$	1.0E-3	1.0E-3, 1.0E-2	1.0E-2	MAX[100GeV/ $m_\chi$ , 10 <sup>-6</sup> ], 1.0
$t\bar{t}, hh$	1.0E-5	1.0E-5, 1.0E-4	1.0E-4	MAX[100GeV/ $m_\chi$ , 10 <sup>-6</sup> ], 1.0
$b\bar{b}, d\bar{d}, u\bar{u}$	9.0E-7	9.0E-7, 9.0E-6	9.0E-6	MAX[100GeV/ $m_\chi$ , 10 <sup>-6</sup> ], 1.0
$\nu\bar{\nu}_{e,\mu,\tau}$	1.0E-3	1.0E-3, 1.0E-2	1.0E-2	MAX[100GeV/ $m_\chi$ , 10 <sup>-6</sup> ], MIN[0.995, ( $E_n(\nu_{line}) - 4\sigma$ ) / $M_\chi$ ]
$e\bar{e}, \mu\bar{\mu}, \tau\bar{\tau}$	1.0E-3	1.0E-3, 1.0E-2	1.0E-2	MAX[100GeV/ $m_\chi$ , 10 <sup>-6</sup> ], MIN[0.995, ( $E_n(\nu_{line}) - 4\sigma$ ) / $M_\chi$ ]

Table 7.1 TODO: fill me daddy

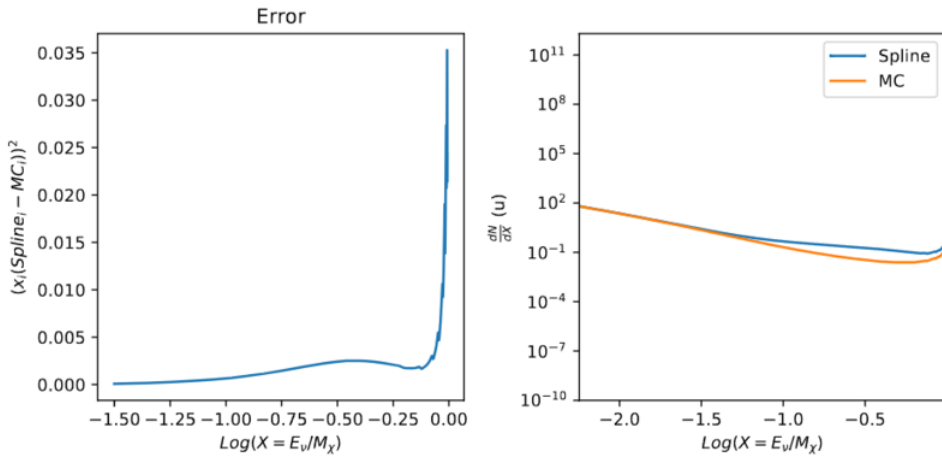


Figure 7.4 Example spline that failed the fit. Failed splined are corrected on a case by case basis unless the SM channel has a systematic problem fitting the splines. In this case, I made a bookkeeping error and loaded the incorrected neutrino flavor

1548 A Final inspection of the splines by eye was done to verify that the spline fitting did not introduce  
 1549 spurious features into the distribution that would corrupt the LLH fitting.

### 1550 7.3.1.3 Composite Neutrino Spectra

1551 With all of the previously mentioned pieces, we are ready to fully assemble a comprehensive  
 1552 description of the particle physics term  $dN/dE$  in Eq. (7.1).

$$\frac{dN_\nu}{dE_\nu} = \left( \frac{dN_{\nu_e}}{dE_{\nu_e}} + \frac{dN_{\nu_\mu}}{dE_{\nu_\mu}} + \frac{dN_{\nu_\tau}}{dE_{\nu_\tau}} \right)_{src} \cdot \mathbf{P}(\nu_\alpha \rightarrow \nu_\beta) \quad (7.5)$$

1553 Presented below are the final spectra that are used in the DM analysis. Bluer spectra are  
 1554 for lower DM mass models. The redder, the higher the DM mass. Energy (x-axis) was chosen  
 1555 to roughly represent the energy sensitivity of NST. These spectra are the composite (nu and tau  
 1556 flavors) versions. How these are combined is mentioned earlier.



Figure 7.5 TODO: Show the post processed spectra that you are sampling[NEEDS A SOURCE][FACT CHECK THIS]

### 1557 7.3.2 *J*- Astrophysical Component

1558 The expected neutrino counts from a dwarf spheroidal galaxy depends also on the the 'astro-  
 1559 physical factor'. The value for this (in our specific case) J-factor for a target depends on its dark  
 1560 matter density distribution,  $\rho_\chi$  and how far it is  $l$ . For this analysis, we adopt the  $\mathcal{GS}$  model used  
 1561 in Sec. 5 for dSph from [45]. These models are based on a modified Navarro-Frenk-White (NFW)  
 1562 profile where the indices of the NFW (traditionally 1,3,1) are allowed to float. More specifically,  
 1563 these DM distributions are described using the Zhao profile. The Zhao profile is written as:

1564 where  $\theta$  is the angular distance from the center of the source. For the case annihilation, the  
 1565 source diameter, [[https://iopscience.iop.org/article/10.1088/0004-637X/801/2/74 here](https://iopscience.iop.org/article/10.1088/0004-637X/801/2/74)] defined as  
 1566 the  $2\theta_{\max}$ , of these dwarves is typically under  $1^\circ$  with the largest in the catalog, Fornax, extending  
 1567 to  $2.61^\circ$ . Fornax is not in the northern sky and the remaining sources are notably below this angular  
 1568 size. Therefore, the sources are treated as point sources because the typical source diameter is under

1569 1 degree. The J-factor used for the point source assumption is the total J emitted from  $\theta_{\max}$ . These  
 1570 values are enumerated in Geringer-Sameth 2015 and again in the table below with their coordinates.  
 1571 Coordinates are given in J200.0 equatorial coordinates. IceCube uses identical sources to Tab. 5.1  
 1572 except we analyze source with declinations above 0.0 degrees.

### 1573 7.3.3 Source Selection and Annihilation Channels

1574 We use all of the dSphs presented in IceCube’s previous dSph DM search [69]. IceCube’s  
 1575 sources for these simulation studies include Bootes I, Canes Venatici I, Canes Venatici II, Coma  
 1576 Berenices, Draco, Hercules, Leo I, Leo II, Leo V, Leo T, Segue 1, Segue 2, Ursa Major I, Ursa Major  
 1577 II, and Ursa Minor. A full description of all sources used in Table 5.1. Sources with declinations  
 1578 less than 0.0 are excluded from this analysis.

1579 This analysis improves on the previous IceCube dSph paper [69] in the following ways. Pre-  
 1580 viously, the IceCube detector was not yet completed to the 86 string configuration. Many more  
 1581 dSphs will be observed, from 4 to 15. Previously, the particle physics model used for neutrino-ray  
 1582 spectra from DM annihilation did not have EW corrections where they are now included [64]. The  
 1583 spectral models also predict substantial differences between the neutrino flavors, so this analysis  
 1584 will be the first DM dwarf analysis to discriminate between primary neutrino flavors. The study  
 1585 performed here studies 10.4 years of data.

1586 The SM annihilation channels probed for this study include  $b\bar{b}$ ,  $t\bar{t}$ ,  $u\bar{u}$ ,  $d\bar{d}$ ,  $e\bar{e}$ ,  $\mu\bar{\mu}$ ,  $\tau\bar{\tau}$ ,  $ZZ$ ,  
 1587  $W^+W^-$ ,  $\nu_e\bar{\nu}_e$ ,  $\nu_\mu\bar{\nu}_\mu$ , and  $\nu_\tau\bar{\nu}_\tau$ .

### 1588 7.4 Likelihood Methods

1589 I use the Point-Source search likelihood which is widely used in IceCube analyses. The  
 1590 likelihood function is defined as the following:

$$L(n_s) = \prod_{i=1}^N \left[ \frac{n_s}{N} S_i + \left(1 - \frac{n_s}{N}\right) B_i \right] \quad (7.6)$$

1591 where  $i$  is an event index,  $S$  and  $B$  are the signal PDF and background PDF respectively. For a joint  
 1592 analysis where the sources are stacked the likelihood is expanded in the simplified way:

$$L(n_s) = \prod_{i=1}^{N_{\text{sources}}} L_i(n_s) \quad (7.7)$$

1593 Where  $L_i$  is the likelihood from the i-th source in the stacked analysis. The test statistic definition  
1594 remains the same as Eq. (5.6)

1595 **7.5 Background Simulation**

1596 Before we look at data, we must first analyze background and signal injection to validate our  
1597 analysis. The following sections show the results of the likelihood fitting for a suite of background  
1598 trials for the DM models we set out to study in [TODO: refer to the section](#). We study the TS  
1599 distributions first for each source, then for the stacked analysis.

1600 The TS distributions are not expected to behalve according to a chi-squared distribution with 1  
1601 degree of freedom. This is in large part due to the distinct spectral shapes demonstrated earlier.  
1602 These can vary significantly between DM mass and annihilation models. Therefor, Wilks' theorem  
1603 may not be applicable to the analysis. Instead, a critical value is defined from a large number of  
1604 background trials.

1605 I assume that TS values are physical:  $TS \geq 0$ .  $\eta$  denotes the fraction of positive TS values  
1606 above the threshold and written in the legend.  $\epsilon[x]$  indicate the fraction of events where  $TS < x$ .  
1607 For TS plots shown here, the decimal values of x are 1.0e-2 and 1.0e-3. The following plots show  
1608 the background TS distributions obtained from Segue1, a source with little Earth attenuation and  
1609 large J-factor, assuming that dark matter annihilates into  $b\bar{b}$ . I also show the 15 source stack TS  
1610 distributions with identical DM models.

1611 **7.5.1 TS per Source**

1612 Below I present the TS distributions for Segue1 and  $\chi\chi \rightarrow b\bar{b}$ . All remaining channels and  
1613 source TS panels are hosted on [TODO: Change this text, it will all be here](#).

1614 Although it was not expected, almost every distribution produced follows a chi2 distribution  
1615 with 1 degree of freedom. This is important for future assumptions made (in multi-messenger) and  
1616 may justify statistical calculations assuming Wilk's theorem is valid.

1617 [TODO: add text saying that you show: bb, numu, and tau??? specs for Seg1 and UMa2?](#)

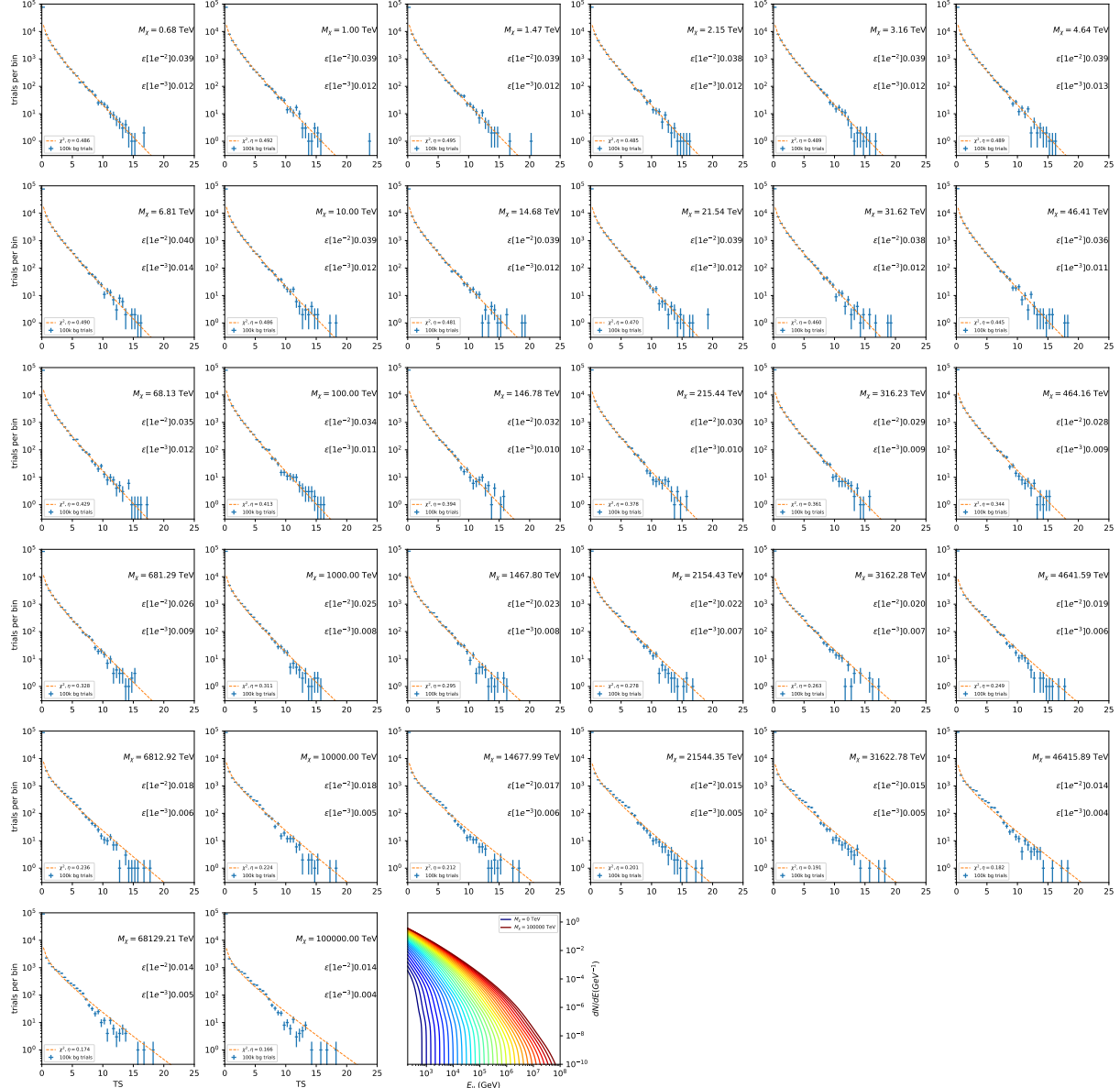


Figure 7.6 TODO: update text because there is no title. Each subplot, except the final, is the TS distribution for a specific DM mass listed in the subplot. The final subplot plots the all DM spectral models used as input for the TS distribution calculations with bluer lines indicating lower DM mass and redder indicating higher DM mass.

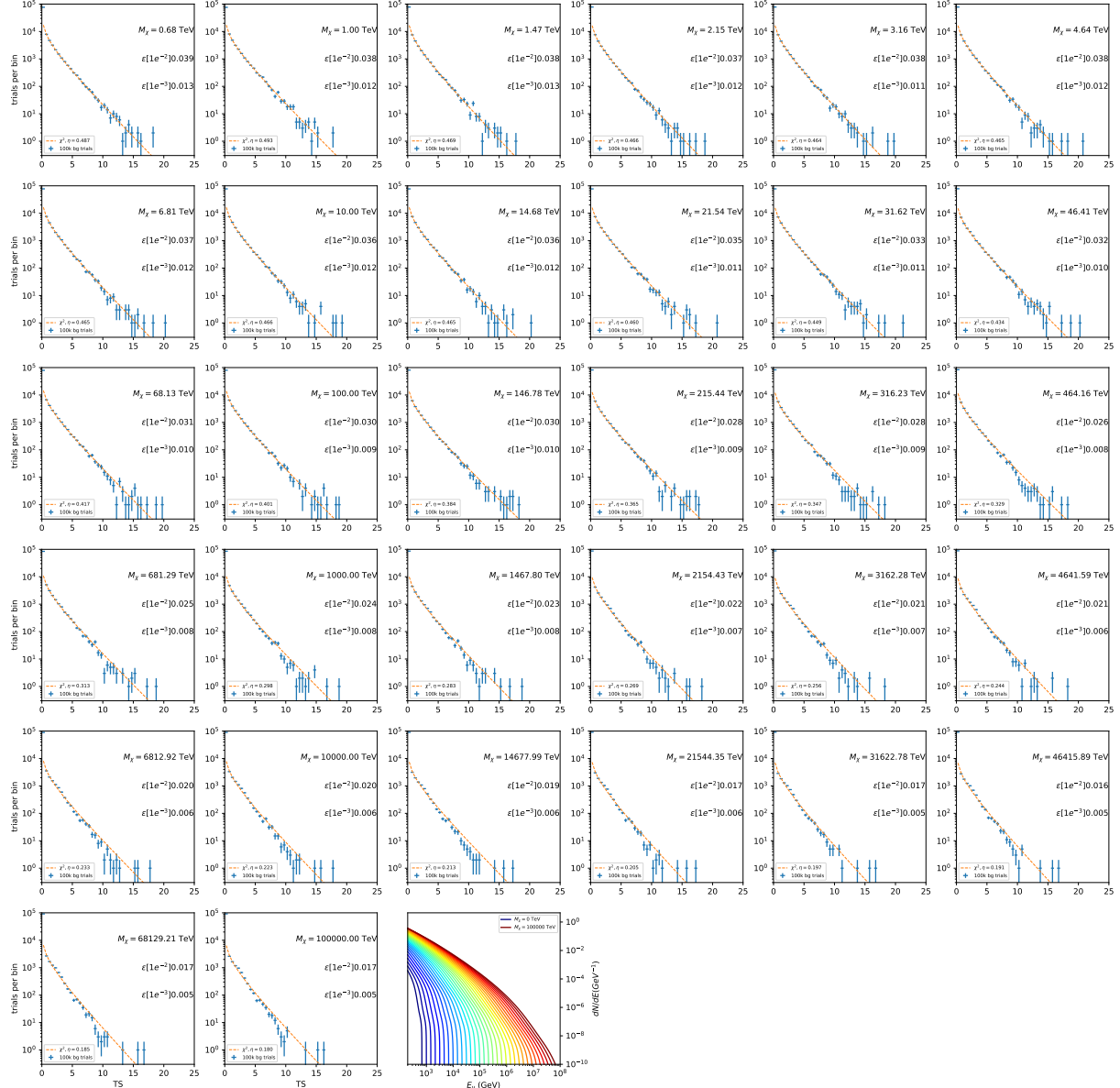


Figure 7.7 TODO: update text because there is no title. Each subplot, except the final, is the TS distribution for a specific DM mass listed in the subplot. The final subplot plots the all DM spectral models used as input for the TS distribution calculations with bluer lines indicating lower DM mass and redder indicating higher DM mass.

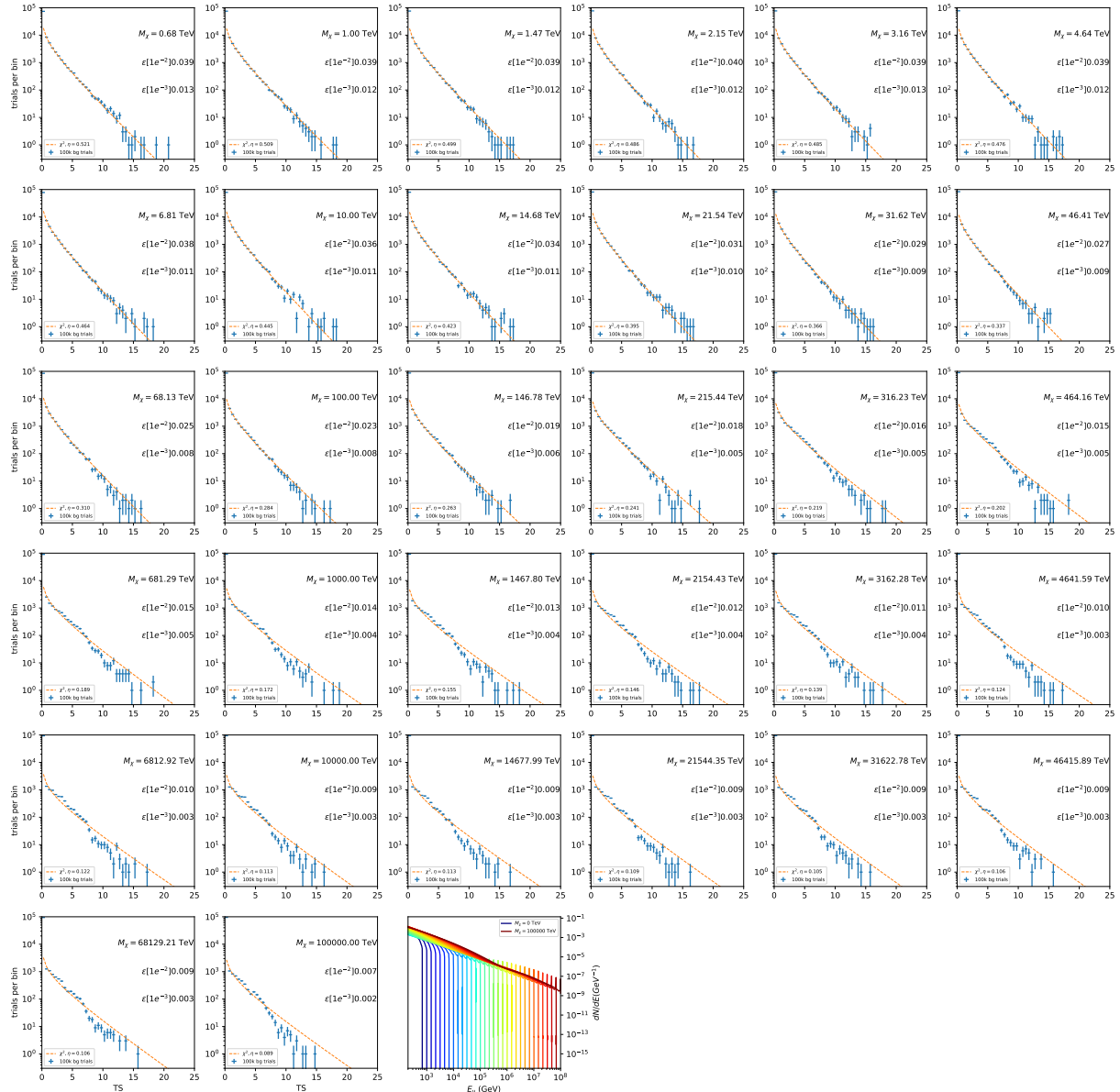


Figure 7.8 TODO: update text because there is no title. Each subplot, except the final, is the TS distribution for a specific DM mass listed in the subplot. The final subplot plots the all DM spectral models used as input for the TS distribution calculations with bluer lines indicating lower DM mass and redder indicating higher DM mass.

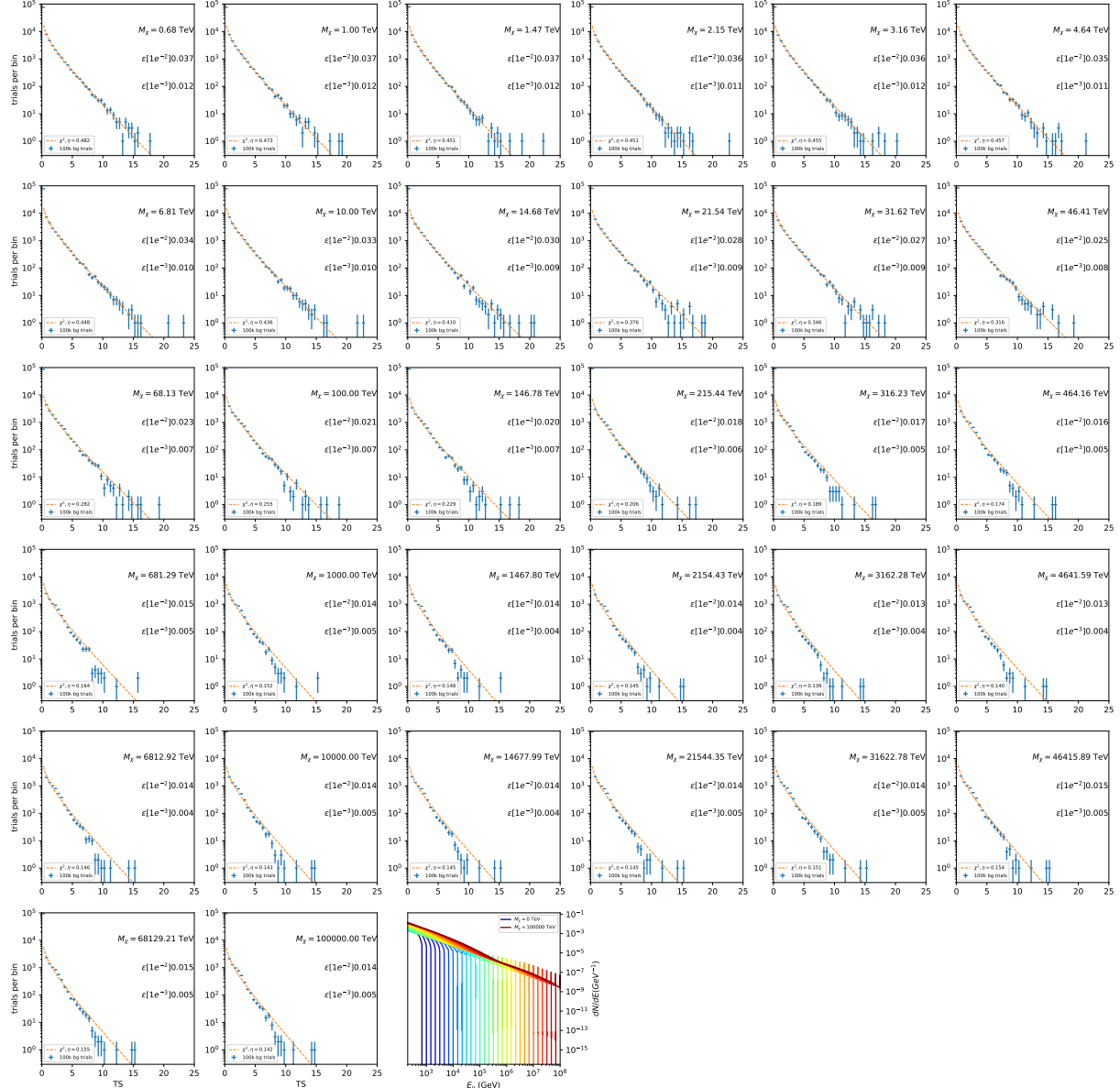


Figure 7.9 TODO: update text because there is no title. Each subplot, except the final, is the TS distribution for a specific DM mass listed in the subplot. The final subplot plots the all DM spectral models used as input for the TS distribution calculations with bluer lines indicating lower DM mass and redder indicating higher DM mass.

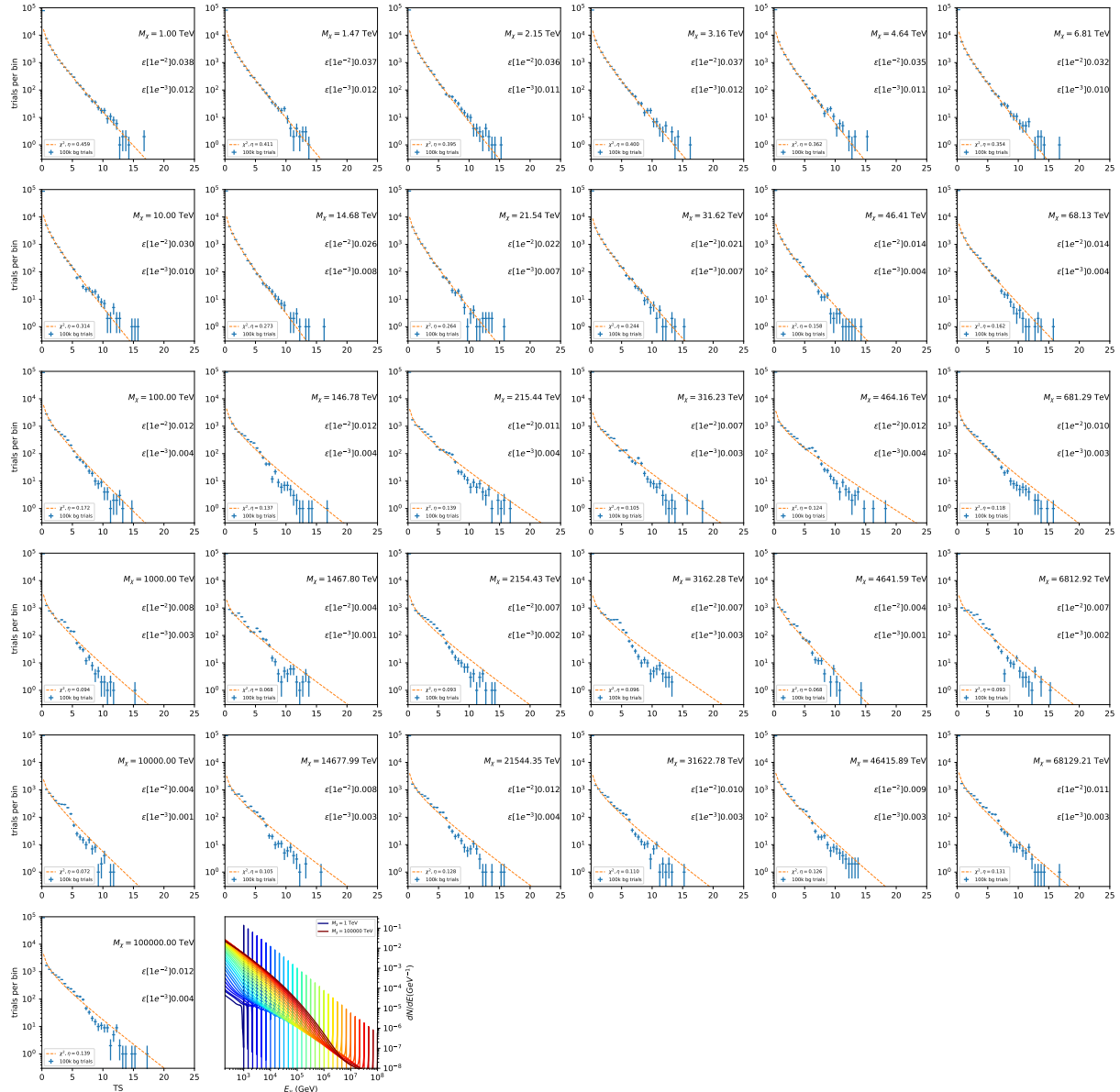


Figure 7.10 TODO: update text because there is no title. Each subplot, except the final, is the TS distribution for a specific DM mass listed in the subplot. The final subplot plots the all DM spectral models used as input for the TS distribution calculations with bluer lines indicating lower DM mass and redder indicating higher DM mass.

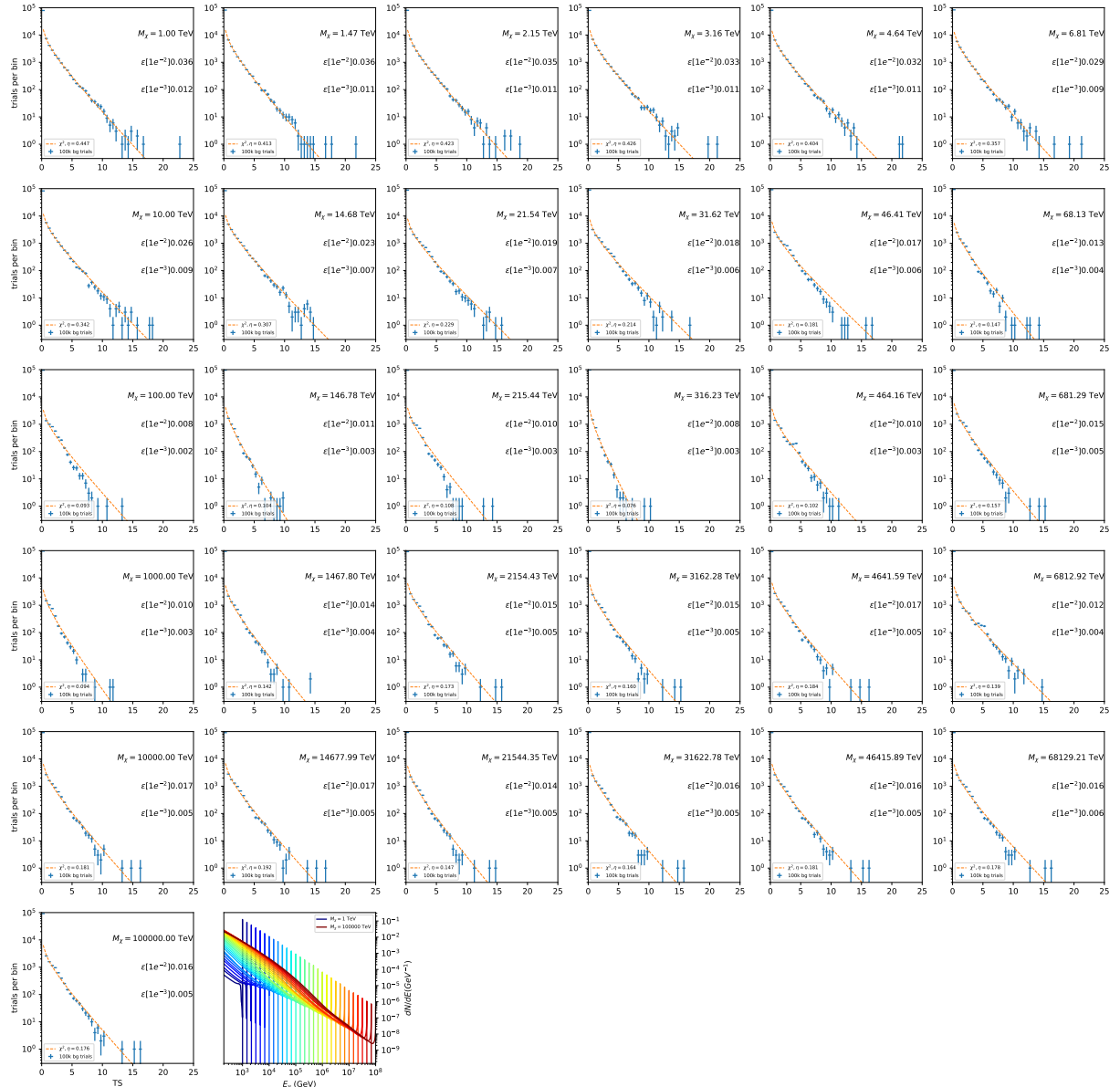


Figure 7.11 TODO: update text because there is no title. Each subplot, except the final, is the TS distribution for a specific DM mass listed in the subplot. The final subplot plots the all DM spectral models used as input for the TS distribution calculations with bluer lines indicating lower DM mass and redder indicating higher DM mass.

## **CHAPTER 8**

### **NU DUCK**

## APPENDIX A

### MULTI-EXPERIMENT SUPPLEMENTARY FIGURES

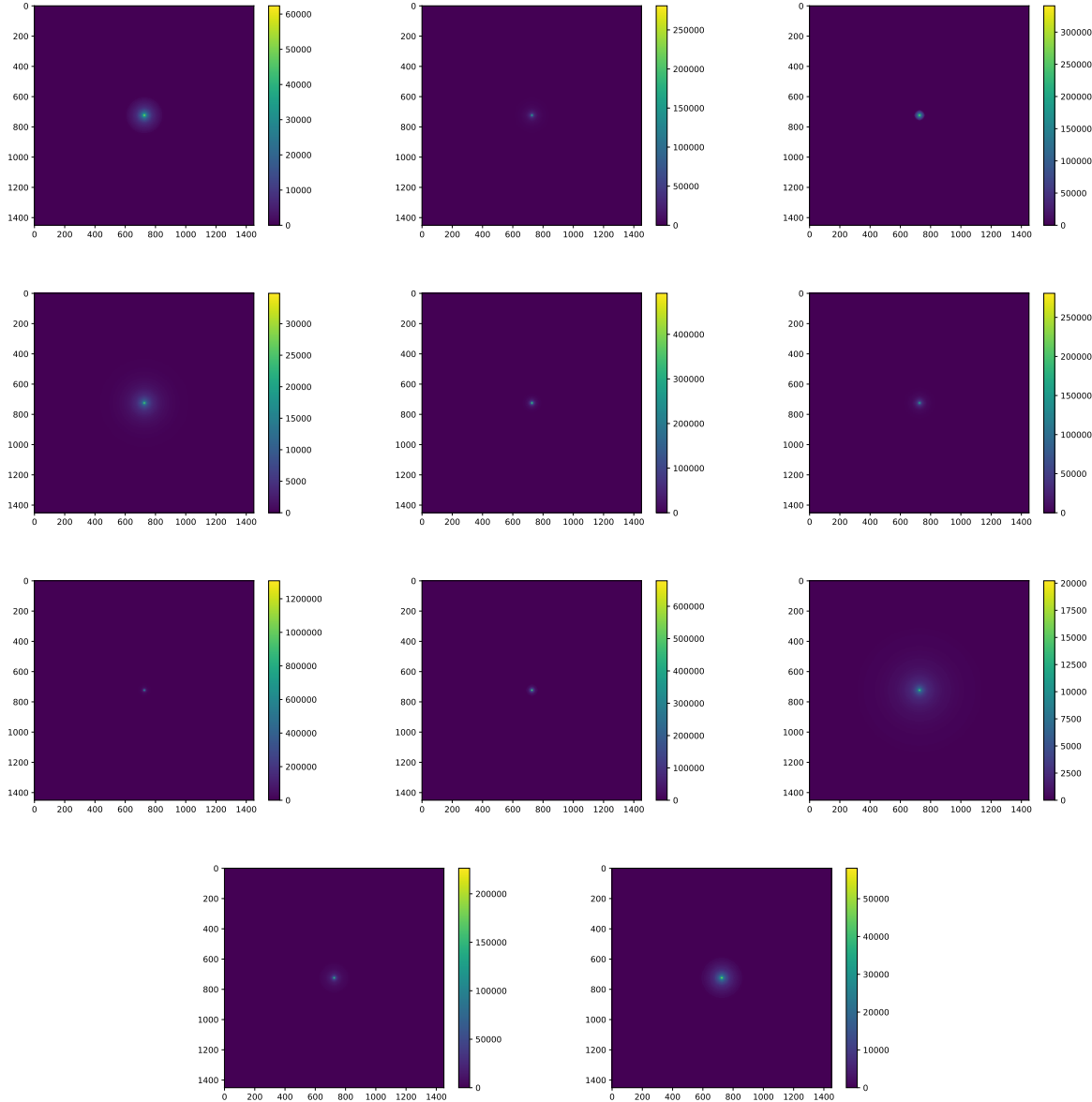


Figure A.1 Sister figure to Figure 5.3. Sources in the first row from left to right: Bootes I, Canes Venatici I, II. In second row: Draco, Hercules, Leo I. In the first row: Leo II, Leo IV, Sextans. In the final row: Ursa Major I, Ursa Major II.

## APPENDIX B

### 1620 MULTITHREADING DARK MATTER ANALYSES SUPPLEMENTARY MATERIAL

#### 1621 B.1 Remaining Spectral Models

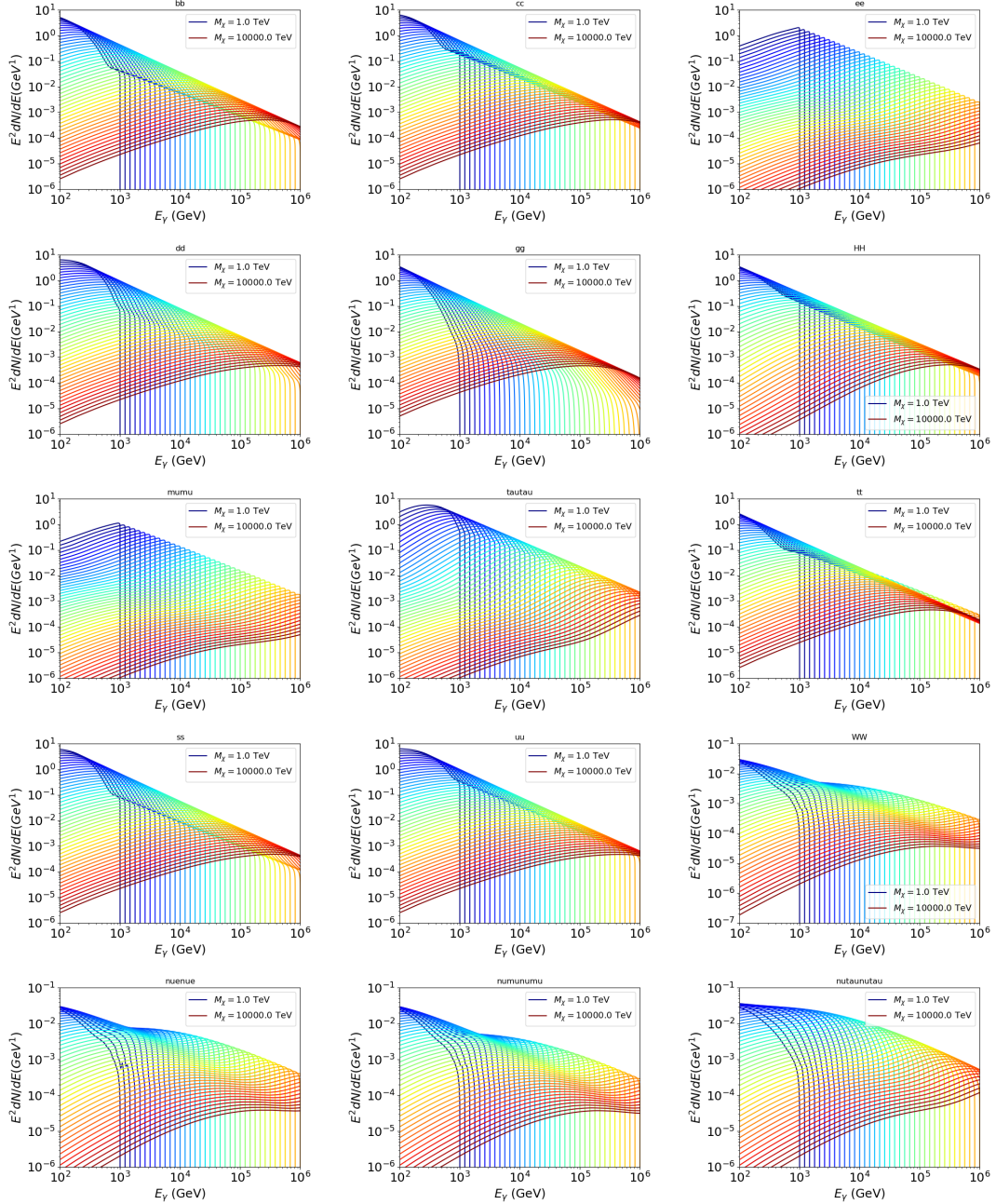


Figure B.1 Sister figure to Figure 6.2 for remaining SM primary annihilation channels studied for this thesis. These did not require any post generation smoothing and so are directly pulled from [64] with a binning scheme most helpful for a HAWC analysis.

## 1622 B.2 mpu\_analysis.py

```
16231 import warnings
16242 with warnings.catch_warnings():
16253     warnings.simplefilter("ignore")
16264 # Python base libraries
16275 import os
16286 import sys
16297 import time
16308 # Import general libraries with namespace
16319 import matplotlib
16320 # Necessary for computing on cluster
16331 matplotlib.use("agg")
16342 import numpy as np
16353 import multiprocessing as mp
16364 # Import HAWC software
16375 sys.path.insert(1, os.path.join(os.environ['HOME'], 'hawc_software', 'threeML-
1638     analysis-scripts', 'fitModel'))
16396 from analysis_modules import *
16407 from threeML import *
16418 from hawc_hal import HAL, HealpixConeROI
16429 from threeML.minimizer.minimization import FitFailed
16430 # Import Dark Matter HAWC Libraries
16441 import analysis_utils as au
16452 import spectra as spec
16463 import sources as srcs
16474
16485 #* READ ONLY PATHS This block will change eventually
16496 MASS_LIST = './plotting/studies/nd/masses.txt'
16507 CHAN_LIST = './plotting/studies/nd/chans.txt'
16518
16529 #* WRITE PATHS, default location is to scratch
16530 OUT_PATH = os.path.join(os.environ["SCRATCH"], os.environ["USER"], 'New_duck')
```

```

16541 print('Our out path is going to be {}'.format(OUT_PATH))
16552
16563 # Define parallel Function. Can also be run serially
16574 def some_mass_fit(sigVs, datalist, shape, dSph, jfactor, mass_chan,
16585                         progress=None, log_file='', queue=None, i_job=0):
16596
16607     if progress is None:
16618         progress = [0]
16629     else: # Create log files for each thread
16630         log_file = log_file.replace('.log', '_ThreadNo_')
16641         log_file = log_file + str(i_job) + ".log"
16652         sys.stdout = open(log_file, "w")
16663
16674     fits = []
16685
16696     try:
16707         for m_c in mass_chan:
16718             print(f'Mass chan tuple: {m_c}')
16729             mass = int(m_c[0])
16730             ch = m_c[1]
16741             # Build path to output files
16752             outPath = os.path.join(OUT_PATH, ch, dSph)
16763             au.ut.ensure_dir(outPath)
16774
16785             if progress[i_job] < 0:
16796                 # If the master gets a Keyboard interrupt, commit suicide.
16807                     break
16818
16829                     ### Start Model Building for DM mass and SM channel #####
16830                     spectrum = spec.DM_models.HDMSpectra()
16841                     spectrum.set_channel(ch)
16852
16863                     myDwarf = ExtendedSource(dSph, spatial_shape=shape,

```

```

16874                     spectral_shape=spectrum)

16885

16896     spectrum.J = jfactor * u.GeV**2 / u.cm**5
16907     spectrum.sigmav = 1e-24 * u.cm**3 / u.s
16918     spectrum.set_dm_mass(mass * u.GeV)

16929

16930     spectrum.sigmav.bounds = (1e-30, 1e-12)
16941     model = Model(myDwarf)
16952     ##### End model Building #####
16963
16974     jl = JointLikelihood(model, datalist, verbose=False)
16985
16996     try:
17007         result, lhdf = jl.fit(compute_covariance=False)
17018         ts = -2.* (jl.minus_log_like_profile(1e-30) - jl.
1702         _current_minimum)
17039         # Also profile the LLH vs sv
17040         ll = jl.get_contours(spectrum.sigmav, sigVs[0],
17051                         sigVs[-1], len(sigVs),
17062                         progress=False, log=['False'])
17073
17084         sigv_ll = au.ut.calc_95_from_profile(ll[0], ll[2])
17095         # Write results to file
17106         outFileLL = outPath+f"/LL_{dSph}_{ch}_mass{int(mass)}_GD.txt"
17117         np.savetxt(outFileLL, (sigVs, ll[2]),
17128                         delimiter='\t', header='sigV\tLL\n')
17139
17140         with open(outPath+f"/results_{dSph}_{ch}_mass{int(mass)}_GD.
1715         txt", "w") as results_file:
17161             results_file.write("mDM [GeV]\tsigV_95\tsigV_B.F.\n")
17172
17183             results_file.write("%i\t%.5E\t%.5E\t%.5E"%(mass, sigv_ll,
17194                                         ts, result.value[0]))

```

```

17205         # End write to file
17216     except FitFailed: # Don't kill all threads if a fit fails
17227         print("Fit failed. Go back and calculate this spectral model
1723 later")
17248         fits.append((ch, mass, -1, -1))
17259         with open(log_file+'.fail', 'w') as f_file:
17260             f_file.write(f'{ch}, {mass}\n')
17271
17282             progress[i_job] += 1
17293             matplotlib.pyplot.close() # Prevent leaky memory
17304
17315             fits.append((ch, mass, result.value[0], ts))
17326             progress[i_job] += 1
17337             matplotlib.pyplot.close()
17348     except KeyboardInterrupt:
17359         progress[i_job] = -1
17360
17371     fits = np.array(fits)
17382     if queue is None:
17393         return fits
17404     else:
17415         queue.put((i_job, fits))
17426
17437 def main(args):
17448     masses = np.loadtxt(MASS_LIST, dtype=int)
17459     chans = np.loadtxt(CHAN_LIST, delimiter=',', dtype=str)
17460     mass_chan = au.ut.permute_lists(chans, masses)
17471
17482     print(f"DM masses for this study are: {masses}")
17493     print(f"SM Channels for this study are XX -> {chans}")
17504     print(mass_chan)
17515
17526 # extract information from input argument

```

```

17537 dSph = args.dSph
17548 data_mngr = au.ut.Data_Selector('P5_NN_2D')
17559 dm_profile = srcts.Spatial_DM(args.catalog, dSph, args.sigma, args.decay)
17560
17571     ### Extract Source Information ####
17582 if dm_profile.get_dec() < -22.0 or dm_profile.get_dec() > 62.0:
17593     raise ValueError("HAWC can't see this source D: Exitting now...")
17604
17615 print(f'{dSph} information')
17626 print(f'jfac: {dm_profile.get_factor()}\tRA: {dm_profile.get_ra()}\tDec: {dm_profile.get_dec()}\n')
1763
17647
17658 shape = SpatialTemplate_2D(fits_file=dm_profile.get_src_fits())
17669     ### Finish Extract Source Information ####
17670
17681     ### LOAD HAWC DATA ####
17692 roi = HealpixConeROI(data_radius=2.0, model_radius=8.0,
17703                         ra=dm_profile.get_ra(), dec=dm_profile.get_dec())
17714 bins = choose_bins.analysis_bins(args, dec=dm_profile.get_dec())
17725
17736 hawc = HAL(dSph, data_mngr.get_datmap(), data_mngr.get_detres(), roi)
17747 hawc.set_active_measurements(bin_list=bins)
17758 datalist = DataList(hawc)
17769     ### FINISH LOAD HAWC DATA ####
17770
17781 # set up SigV sampling. This sample is somewhat standardized
17792 sigVs = np.logspace(-28,-18, 1001, endpoint=True) # NOTE This will change
1780 with HDM
17813
17824 if args.n_threads == 1:
17835     # No need to start || programming just iterate over the masses
17846 kw_arg = dict(sigVs=sigVs, datalist=datalist, shape=shape, dSph=dSph,
17857                 jfactor=dm_profile.get_factor(), mass_chan=mass_chan,

```

```

17868             log_file=args.log)
17869             some_mass_fit(**kw_arg)
17880         else:
17891             # I Really want to suppress TQMD output
17902             from tqdm import tqdm
17913             from functools import partialmethod
17924             tqdm.__init__ = partialmethod(tqdm.__init__, disable=True)
17935
17946             x = np.array_split(mass_chan, args.n_threads)
17957             n_jobs = len(x)
17968
17979             print("Thread jobs summary by mass and SM channel")
17980             for xi in x:
17991                 print(f'{xi}')
18002
18013             queue = mp.Queue()
18024             progress = mp.Array('i', np.zeros(n_jobs, dtype=int))
18035
18046             # Define task pool that will be split amongsts threads
18057             kw_args = [dict(sigVs=sigVs, datalist=datalist, shape=shape,
18068                             dSph=dSph, jfactor=dm_profile.get_factor(),
18079                             mass_chan=mass_chan, progress=progress,
18080                             queue=queue, i_job=i, log_file=args.log)
18091                 for i, mass_chan in enumerate(x)]
18102
18113             # Define each process
18124             procs = [mp.Process(target=some_mass_fit, kwargs=kw_args[i]) \
18135                 for i in range(n_jobs)]
18146
18157             ### Start MASTER Thread only code block ###
18168             # Begin running all child threads
18179             for proc in procs: proc.start()
18180

```

```

18191     try:
18202         # In this case, the master does nothing except monitor progress of
18213         # the threads
18224             # In an ideal world, the master thread also does some computation.
18235             n_complete = np.sum(progress)
18246             while_count = 0
18257
18268                 while n_complete < len(mass_chan):
18279
18280                     if np.any(np.asarray(progress) < 0):
18291                         # This was no threads are stranded when killing the script
18302                         raise KeyboardInterrupt()
18313                     if while_count%1000 == 0:
18324                         print(f"{np.sum(progress)} of {len(mass_chan)} finished")
18335
18346             n_complete = np.sum(progress)
18357             time.sleep(.25)
18368             while_count += 1
18379
18380                 except KeyboardInterrupt:
18391                     # signal to jobs that it's time to stop
18402                         for i in range(n_jobs):
18413                             progress[i] = -2
18424                             print('\nKeyboardInterrupt: terminating early.')
18435                         ### End MASTER Thread only code block ###
18446
18457             fitss = [queue.get() for proc in procs]
18468             print(fitss)
18479             print(f'Thread statuses: {progress[:]}')
18480
18491             # putting results in a file
18501
18512             print("QUACK! All Done!")

```

```

18523
18534
18545 if __name__ == '__main__':
18556     import argparse
18567
18578     p = argparse.ArgumentParser(description="Run a DM annihilation analysis on
1858         a dwarf spheroidal for a specific SM channel for DM masses [1 TeV to 10
1859         PeV]")
18609
18610     # Dwarf spatial modeling arguements
18621     p.add_argument("-ds", "--dSph", type=str,
18632             help="dwarf spheroidal galaxy to be studied", required=
1864 True)
18653     p.add_argument("-cat", "--catalog", type=str, choices=['GS15', 'LS20'],
18664             default='LS20', help="source catalog used")
18675     p.add_argument("-sig", "--sigma", type=int, choices=[-1, 0, 1], default=0,
18686             help="Spatial model uncertainty. 0 corresponds to the
1869 median. +/-1 correspond to the +/-1sigma uncertainty respectively.")
18707
18718     # Arguements for the energy estimators
18729     p.add_argument("-e", "--estimator", type=str,
18730             choices=['P5_NHIT', 'P5_NN_2D'],
18741             default="P5_NN_2D", required=False,
18752             help="The energy estimator choice. Options are: P5_NHIT,
1876 P5_NN_2D. GP not supported (yet).")
18773     p.add_argument("--use-bins", default=None, nargs="*",
18784             help="Bins to use for the analysis", dest="use_bins")
18795     p.add_argument('--select_bins_by_energy', default=None, nargs="*",
18806             help="Does nothing. May fill in later once better
1881 understood")
18827     p.add_argument('--select_bins_by_fhit', default=None, nargs="*",
18838             help="Also does nothing see above")
18849     p.add_argument( '-ex', "--exclude", default=None, nargs="*",

```

```

18850             help="Exclude Bins", dest="exclude")

18861

18872     # Computing and logging arguements.

18883     p.add_argument('-nt', '--n_threads', type=int, default=1,
18894                     help='Maximum number of threads spawned by script. Default
1890      is 4')

18915     p.add_argument('-log', '--log', type=str, required=True,
18926                     help='Name for log files. Especially needed for threads')

18937

18948     p.add_argument('--decay', action="store_true",
18959                     help='Set spectral DM hypothesis to decay')

18960

18971     args = p.parse_args()

18982     print(args.decay)

18993     if args.exclude is None: # default exclude bins 0 and 1
19004         args.exclude = ['B0C0Ea', 'B0C0Eb', 'B0C0Ec', 'B0C0Ed', 'B0C0Ee']

19015

19026     if args.decay: OUT_PATH += '_dec'
19037     else: OUT_PATH += '_ann'

19048

19059     OUT_PATH = OUT_PATH + '_' + args.catalog
19060     if args.sigma != 0: OUT_PATH += f'_{args.sigma}sig'

19071

19082     main(args)

```

1909 B.3 Comparison with Glory Duck

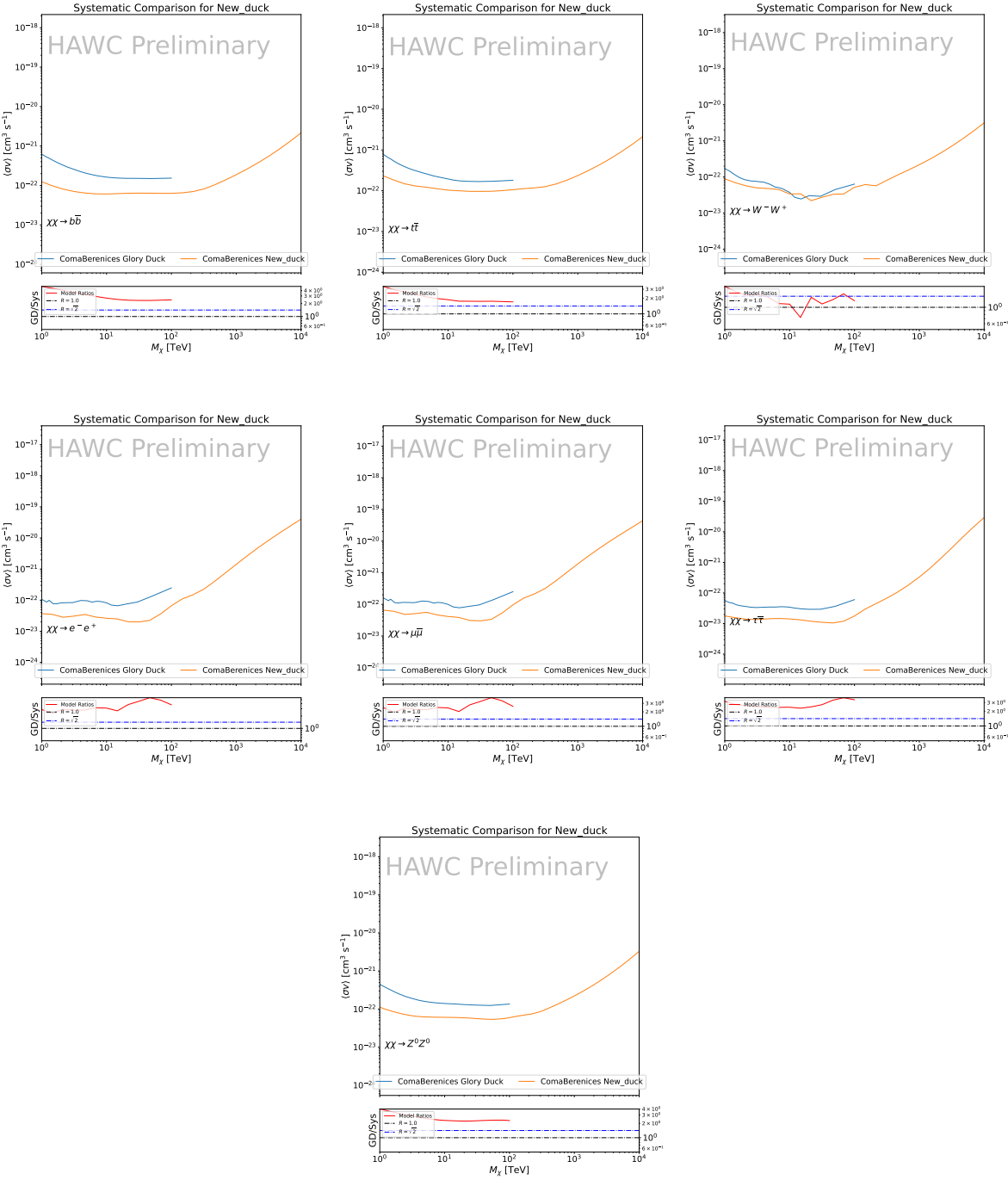


Figure B.2 TODO: fill this out

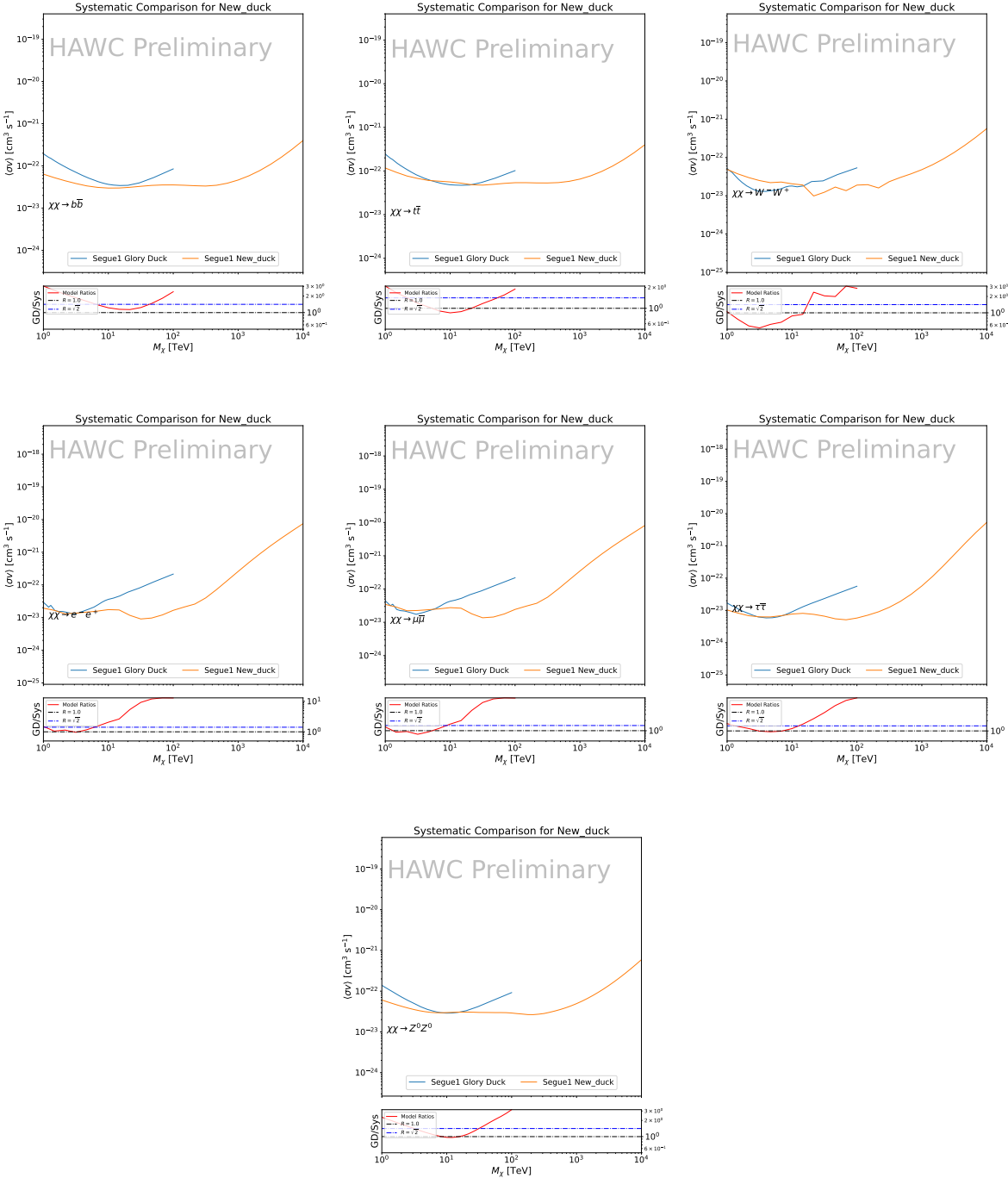


Figure B.3 TODO: fill this out

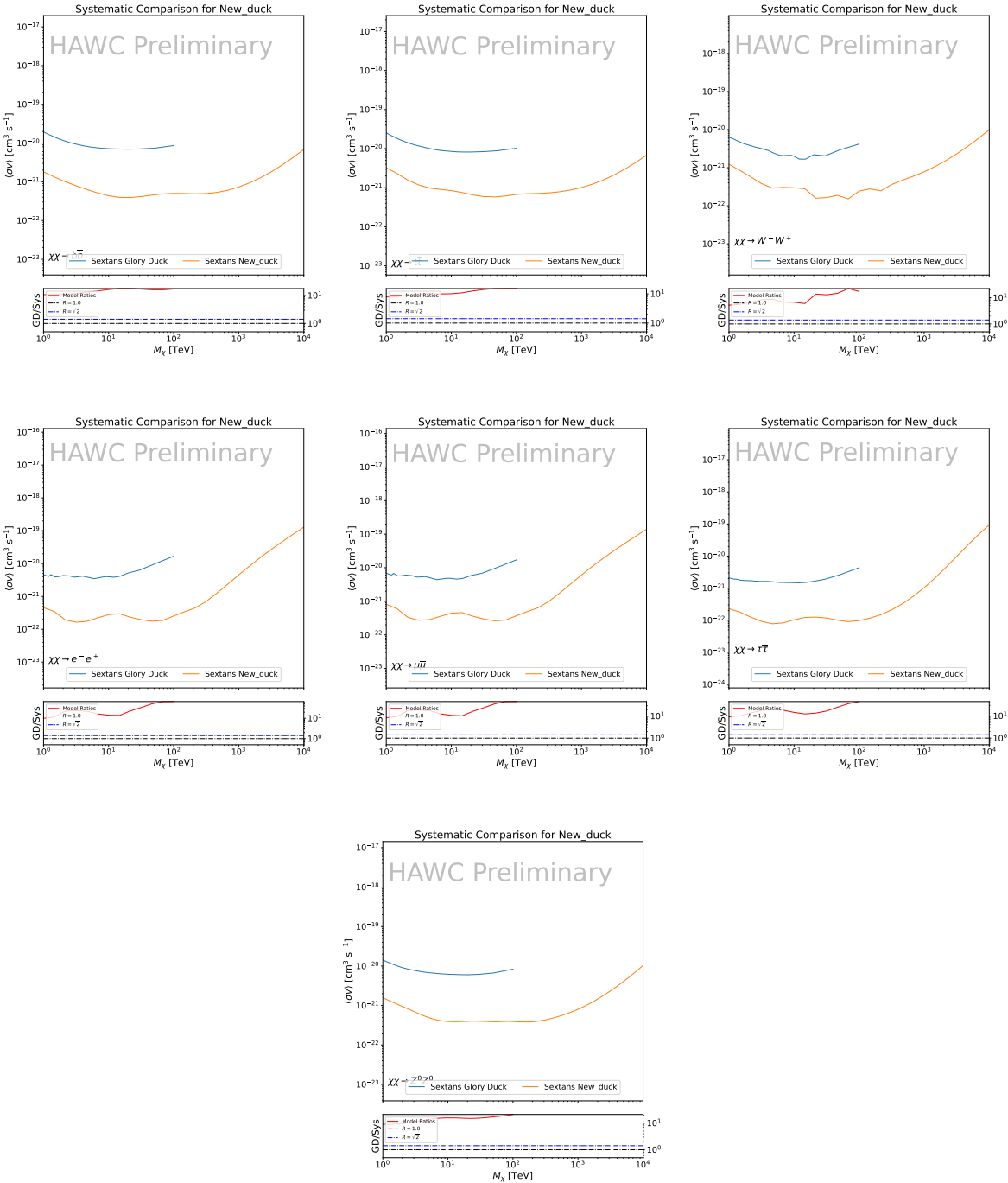


Figure B.4 TODO: fill this out

## APPENDIX C

### 1910 ICECUBE HEAVY DARK MATTER ANALYSIS SUPPLEMENTARY MATERIAL

#### 1911 C.1 Docker Image for Oscillating Neutrino Spectra

```
19121 FROM ubuntu:18.04
19132
19143 # Execute commands to install software packages
19154 RUN apt -y update
19165
19176     # Install utility programs
19187 RUN apt -y install vim wget git cmake
19198
19209 ARG DEBIAN_FRONTEND=noninteractive
19210
19221     # Install python
19232 RUN apt -y install python python-dev python-pip libjpeg-dev zlib1g-dev
19243
19254     # We need Python2 for installing Charon.
19265 RUN apt -y install python-numpy python-sympy python-matplotlib \
19276             python-sympy python-h5py python-astropy python-ipython
19287
19298     # Install dependencies of Charon : SQuIDS, NuSQuIDS
19309 RUN apt -y install libgsl-dev libgslcblas0 libgsl23 gsl-bin pkg-config
19310     # Install SQuIDS
19321 RUN mkdir /home/SQuIDS /home/SQuIDS_install
19332 WORKDIR /home/SQuIDS
19343 RUN git clone https://github.com/jsalvado/SQuIDS.git
19354 WORKDIR /home/SQuIDS/SQuIDS
19365 RUN git checkout 7ad9ba7c6ad06d1f0fa8418f937ebf1a403fef90
19376     # Before executing "make install" an environmental variable has to be set.
19387 ENV PKG_CONFIG_PATH=/home/SQuIDS/SQuIDS/lib
19398 RUN ./configure --prefix=../SQuIDS_install \
```

```

19409     && make
19410 RUN make install
19421
19432     # Set up an environmental varialbe that is required to install nuSQuIDS..
19443 ENV SQuIDS=/home/SQuIDS/SQuIDS
19454 ENV LD_LIBRARY_PATH=$SQuIDS/lib:$LD_LIBRARY_PATH
19465
19476     # Install NuSQuIDS
19487 RUN mkdir /home/nuSQuIDS
19498 WORKDIR /home/nuSQuIDS
19509 RUN git clone https://github.com/qrliu/nuSQuIDS.git
19510 WORKDIR /home/nuSQuIDS/nuSQuIDS
19521 RUN git checkout 072d8ef740e2fc7330f1fabaea94f0f4540c46f9
19532 RUN apt -y install libhdf5-dev hdf5-tools
19543 RUN apt -y install libboost1.65-all-dev
19554 RUN ./configure --with-squids=$SQuIDS --with-python-bindings --prefix=../
1956     nuSQuIDS_install \
19575     && make \
19586     && make install
19597
19608     # Set up an environmental variable for nuSQuIDS.
19619 ENV nuSQuIDS=/home/nuSQuIDS/nuSQuIDS
19620 ENV LD_LIBRARY_PATH=$nuSQuIDS/lib:$LD_LIBRARY_PATH
19631
19642     # Build the python bindings
19653 WORKDIR /home/nuSQuIDS/nuSQuIDS/resources/python/src
19664 RUN make
19675
19686     # Set up an environmental variable for the python bindings.
19697 ENV PYTHONPATH=$nuSQuIDS/resources/python/bindings/:$PYTHONPATH
19708
19719     # Install Charon in the /home/Charon/charon directory.
19720 RUN mkdir /home/Charon

```

```
19731 WORKDIR /home/Charon
19742 RUN git clone https://github.com/icecube/charon.git \
19753   && apt -y install unzip python-scipy
19764 WORKDIR charon
19775 RUN git checkout c531efe4e01dc364a60d1c83f950f04526ccd771
19786 RUN unzip ./charon/xsec/xsec.zip -d charon/xsec/ \
19797
19808 # Download neutrino spectra tables in the /home/Charon/charon/data directory
1981 .
19829 && mkdir ./charon/data
19830 WORKDIR ./charon/data
19841 RUN wget --no-check-certificate https://icecube.wisc.edu/~qliu/charon/
1985     SpectraEW.hdf5 \
19862 && wget --no-check-certificate https://icecube.wisc.edu/~qliu/charon/
1987     Spectra_PYTHIA.hdf5 \
19883 && wget --no-check-certificate https://icecube.wisc.edu/~qliu/charon/
1989     Spectra_noEW.hdf5
19904
19915 WORKDIR ../..
19926 RUN python setup.py install
19937 WORKDIR /home
```

1994 C.2 Spline Fitting Statuses

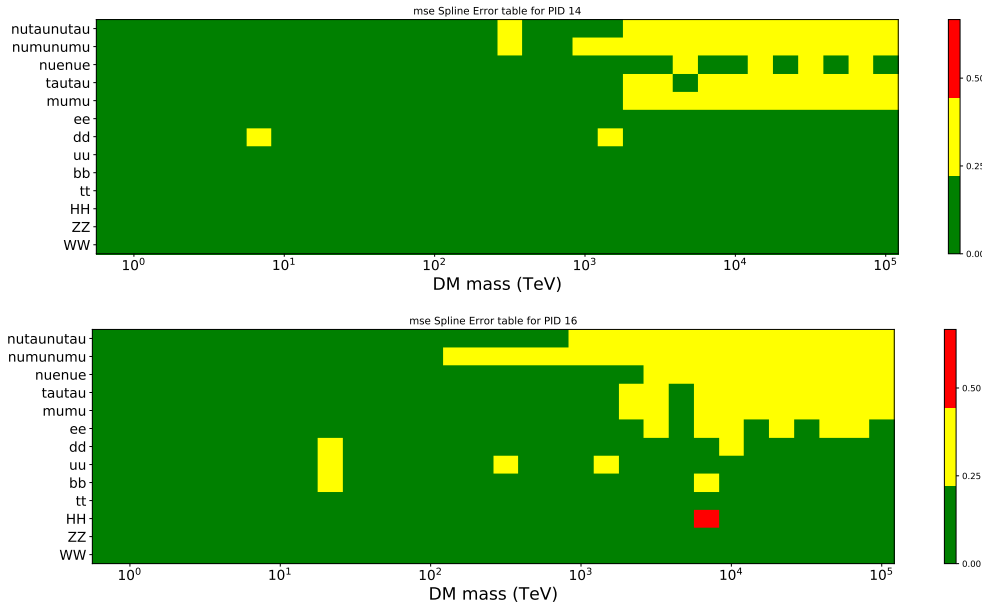


Figure C.1 TODO: fill me daddy

1995

## BIBLIOGRAPHY

- 1996 [1] Anne M. Green. “Dark matter in astrophysics/cosmology”. In: *SciPost Phys. Lect. Notes* (2022), p. 37. doi: [10.21468/SciPostPhysLectNotes.37](https://doi.org/10.21468/SciPostPhysLectNotes.37). URL: <https://scipost.org/10.21468/SciPostPhysLectNotes.37>.
- 1999 [2] Bing-Lin Young. “A survey of dark matter and related topics in cosmology”. In: *Frontiers of Physics* 12 (Oct. 2016). doi: <https://doi.org/10.1007/s11467-016-0583-4>. URL: <https://doi.org/10.1007/s11467-016-0583-4>.
- 2002 [3] Gianfranco Bertone, Dan Hooper, and Joseph Silk. “Particle dark matter: evidence, candidates and constraints”. In: *Physics Reports* 405.5 (2005), pp. 279–390. issn: 0370-1573. doi: <https://doi.org/10.1016/j.physrep.2004.08.031>. URL: <https://www.sciencedirect.com/science/article/pii/S0370157304003515>.
- 2006 [4] Gianfranco Bertone and Dan Hooper. “History of dark matter”. In: *Rev. Mod. Phys.* 90 (4 Aug. 2018), p. 045002. doi: [10.1103/RevModPhys.90.045002](https://doi.org/10.1103/RevModPhys.90.045002). URL: <https://link.aps.org/doi/10.1103/RevModPhys.90.045002>.
- 2009 [5] Fritz Zwicky. “The Redshift of Extragalactic Nebulae”. In: *Helvetica Physica Acta* 6. (1933), pp. 110–127. doi: [10.5169/seals-110267](https://doi.org/10.5169/seals-110267).
- 2011 [6] Vera C. Rubin and Jr. Ford W. Kent. “Rotation of the Andromeda Nebula from a Spectroscopic Survey of Emission Regions”. In: *ApJ* 159 (Feb. 1970), p. 379. doi: [10.1086/150317](https://doi.org/10.1086/150317).
- 2014 [7] K. G. Begeman, A. H. Broeils, and R. H. Sanders. “Extended rotation curves of spiral galaxies: dark haloes and modified dynamics”. In: *Monthly Notices of the Royal Astronomical Society* 249.3 (Apr. 1991), pp. 523–537. issn: 0035-8711. doi: [10.1093/mnras/249.3.523](https://doi.org/10.1093/mnras/249.3.523). eprint: <https://academic.oup.com/mnras/article-pdf/249/3/523/18160929/mnras249-0523.pdf>. URL: <https://doi.org/10.1093/mnras/249.3.523>.
- 2019 [8] *Different types of gravitational lenses*. website. Feb. 2004. URL: <https://esahubble.org/images/heic0404b/>.
- 2021 [9] Douglas Clowe et al. “A Direct Empirical Proof of the Existence of Dark Matter”. In: *apjl* 648.2 (Sept. 2006), pp. L109–L113. doi: [10.1086/508162](https://doi.org/10.1086/508162). arXiv: [astro-ph/0608407 \[astro-ph\]](https://arxiv.org/abs/astro-ph/0608407).
- 2024 [10] Planck Collaboration and N. et. al. Aghanim. “Planck 2018 results I. Overview and the cosmological legacy of Planck”. In: *A&A* 641 (2020). doi: [10.1051/0004-6361/201833880](https://doi.org/10.1051/0004-6361/201833880). URL: <https://doi.org/10.1051/0004-6361/201833880>.
- 2027 [11] Wayne Hu. *Matter Density Animation*. web. 2024. URL: <http://background.uchicago.edu/~whu/animbut/anim2.html>.

- 2029 [12] Wenlong Yuan et al. “A First Look at Cepheids in a Type Ia Supernova Host with JWST”. in:  
2030     *The Astrophysical Journal Letters* 940.1 (Nov. 2022). doi: [10.3847/2041-8213/ac9b27](https://doi.org/10.3847/2041-8213/ac9b27).  
2031     URL: <https://dx.doi.org/10.3847/2041-8213/ac9b27>.
- 2032 [13] Wendy L. Freedman. “Measurements of the Hubble Constant: Tensions in Perspective”. In:  
2033     *The Astrophysical Journal* 919.1 (Sept. 2021), p. 16. doi: [10.3847/1538-4357/ac0e95](https://doi.org/10.3847/1538-4357/ac0e95).  
2034     URL: <https://dx.doi.org/10.3847/1538-4357/ac0e95>.
- 2035 [14] Jodi Cooley. “Dark Matter direct detection of classical WIMPs”. In: *SciPost Phys. Lect.*  
2036     *Notes* (2022), p. 55. doi: [10.21468/SciPostPhysLectNotes.55](https://doi.org/10.21468/SciPostPhysLectNotes.55). URL: <https://scipost.org/10.21468/SciPostPhysLectNotes.55>.
- 2038 [15] “Search for new phenomena in events with an energetic jet and missing transverse momentum  
2039     in  $pp$  collisions at  $\sqrt{s} = 13$  TeV with the ATLAS detector”. In: *Phys. Rev. D* 103  
2040     (11 July 2021), p. 112006. doi: [10.1103/PhysRevD.103.112006](https://doi.org/10.1103/PhysRevD.103.112006). URL: <https://link.aps.org/doi/10.1103/PhysRevD.103.112006>.
- 2042 [16] *Jetting into the dark side: a precision search for dark matter*. website. July 2020. URL:  
2043     <https://atlas.cern/updates/briefing/precision-search-dark-matter>.
- 2044 [17] Celine Armand et. al. “Combined dark matter searches towards dwarf spheroidal galaxies  
2045     with Fermi-LAT, HAWC, H.E.S.S., MAGIC, and VERITAS”. in: *Proceedings of Science*.  
2046     Vol. 395. Mar. 2022. doi: <https://doi.org/10.22323/1.395.0528>.
- 2047 [18] Tracy R. Slatyer. “Les Houches Lectures on Indirect Detection of Dark Matter”. In: *SciPost*  
2048     *Phys. Lect. Notes* (2022), p. 53. doi: [10.21468/SciPostPhysLectNotes.53](https://doi.org/10.21468/SciPostPhysLectNotes.53). URL:  
2049     <https://scipost.org/10.21468/SciPostPhysLectNotes.53>.
- 2050 [19] Christian W Bauer, Nicholas L. Rodd, and Bryan R. Webber. “Dark matter spectra from  
2051     the electroweak to the Planck scale”. In: *Journal of High Energy Physics* 2021.1029-8479  
2052     (June 2021). doi: [https://doi.org/10.1007/JHEP06\(2021\)121](https://doi.org/10.1007/JHEP06(2021)121).
- 2053 [20] Riccardo Catena and Piero Ullio. “A novel determination of the local dark matter density”.  
2054     In: *Journal of Cosmology and Astroparticle Physics* 2010.08 (Aug. 2010), p. 004. doi:  
2055     [10.1088/1475-7516/2010/08/004](https://doi.org/10.1088/1475-7516/2010/08/004). URL: <https://dx.doi.org/10.1088/1475-7516/2010/08/004>.
- 2057 [21] B. P. Abbott et al. “Observation of Gravitational Waves from a Binary Black Hole Merger”.  
2058     In: *Phys. Rev. Lett.* 116 (6 Feb. 2016), p. 061102. doi: [10.1103/PhysRevLett.116.061102](https://doi.org/10.1103/PhysRevLett.116.061102). URL: <https://link.aps.org/doi/10.1103/PhysRevLett.116.061102>.
- 2060 [22] R. Abbasi et. al. “Observation of high-energy neutrinos from the Galactic plane”. In: *Science*  
2061     380.6652 (June 2023), pp. 1338–1343.
- 2062 [23] NASA Goddard Space Flight Center. *Fermi’s 12-year view of the gamma-ray sky*. website.

- 2063 2022. URL: <https://svs.gsfc.nasa.gov/14090>.
- 2064 [24] Marco Cirelli et al. “PPPC 4 DM ID: a poor particle physicist cookbook for dark matter  
2065 indirect detection”. In: *Journal of Cosmology and Astroparticle Physics* 2011.03 (Mar.  
2066 2011), p. 051. doi: [10.1088/1475-7516/2011/03/051](https://doi.org/10.1088/1475-7516/2011/03/051). URL: <https://dx.doi.org/10.1088/1475-7516/2011/03/051>.
- 2068 [25] Javier Rico. “Gamma-Ray Dark Matter Searches in Milky Way Satellites—A Comparative  
2069 Review of Data Analysis Methods and Current Results”. In: *Galaxies* 8.1 (Mar. 2020), p. 25.  
2070 doi: [10.3390/galaxies8010025](https://doi.org/10.3390/galaxies8010025). arXiv: [2003.13482](https://arxiv.org/abs/2003.13482) [astro-ph.HE].
- 2071 [26] W. B. Atwood et al. “The Large Area Telescope on the Fermi Gamma-Ray Space Telescope  
2072 Mission”. In: *apj* 697.2 (June 2009), pp. 1071–1102. doi: [10.1088/0004-637X/697/2/1071](https://doi.org/10.1088/0004-637X/697/2/1071). arXiv: [0902.1089](https://arxiv.org/abs/0902.1089) [astro-ph.IM].
- 2074 [27] M. Ackermann et al. “Searching for Dark Matter Annihilation from Milky Way Dwarf  
2075 Spheroidal Galaxies with Six Years of Fermi Large Area Telescope Data”. In: *prl* 115.23,  
2076 231301 (Dec. 2015), p. 231301. doi: [10.1103/PhysRevLett.115.231301](https://doi.org/10.1103/PhysRevLett.115.231301). arXiv:  
2077 [1503.02641](https://arxiv.org/abs/1503.02641) [astro-ph.HE].
- 2078 [28] Mattia Di Mauro, Martin Stref, and Francesca Calore. “Investigating the effect of Milky  
2079 Way dwarf spheroidal galaxies extension on dark matter searches with Fermi-LAT data”.  
2080 In: *Phys. Rev. D* 106 (12 Dec. 2022), p. 123032. doi: [10.1103/PhysRevD.106.123032](https://doi.org/10.1103/PhysRevD.106.123032).  
2081 URL: <https://link.aps.org/doi/10.1103/PhysRevD.106.123032>.
- 2082 [29] F. et al. Aharonian. “Observations of the Crab Nebula with H.E.S.S.”. In: *Astron. Astrophys.*  
2083 457 (2006), pp. 899–915. doi: [10.1051/0004-6361:20065351](https://doi.org/10.1051/0004-6361:20065351). arXiv: [astro-ph/0607333](https://arxiv.org/abs/astro-ph/0607333).
- 2085 [30] J. Albert et al. “VHE  $\gamma$ -Ray Observation of the Crab Nebula and its Pulsar with the MAGIC  
2086 Telescope”. In: *The Astrophysical Journal* 674.2 (Feb. 2008), p. 1037. doi: [10.1086/525270](https://doi.org/10.1086/525270). URL: <https://dx.doi.org/10.1086/525270>.
- 2088 [31] N. Park. “Performance of the VERITAS experiment”. In: *Proceedings, 34th International  
2089 Cosmic Ray Conference (ICRC2015): The Hague, The Netherlands, July, 30th July - 6th  
2090 August*. Vol. 34. 2015, p. 771. arXiv: [1508.07070](https://arxiv.org/abs/1508.07070) [astro-ph.IM].
- 2091 [32] A. Abramowski et al. “H.E.S.S. constraints on Dark Matter annihilations towards the Sculptor  
2092 and Carina Dwarf Galaxies”. In: *Astropart. Phys.* 34 (2011), pp. 608–616. doi: [10.1016/j.astropartphys.2010.12.006](https://doi.org/10.1016/j.astropartphys.2010.12.006). arXiv: [1012.5602](https://arxiv.org/abs/1012.5602) [astro-ph.HE].
- 2094 [33] A. Abramowski et al. “Search for dark matter annihilation signatures in H.E.S.S. observations  
2095 of Dwarf Spheroidal Galaxies”. In: *Phys. Rev. D* 90 (2014), p. 112012. doi: [10.1103/PhysRevD.90.112012](https://doi.org/10.1103/PhysRevD.90.112012). arXiv: [1410.2589](https://arxiv.org/abs/1410.2589) [astro-ph.HE].

- 2097 [34] H. Abdalla et al. “Searches for gamma-ray lines and ‘pure WIMP’ spectra from Dark  
2098 Matter annihilations in dwarf galaxies with H.E.S.S”. in: *JCAP* 11 (2018), p. 037. doi:  
2099 [10.1088/1475-7516/2018/11/037](https://doi.org/10.1088/1475-7516/2018/11/037). arXiv: [1810.00995 \[astro-ph.HE\]](https://arxiv.org/abs/1810.00995).
- 2100 [35] J. Aleksić et al. “Optimized dark matter searches in deep observations of Segue 1 with  
2101 MAGIC”. in: *JCAP* 1402 (2014), p. 008. doi: [10.1088/1475-7516/2014/02/008](https://doi.org/10.1088/1475-7516/2014/02/008).  
2102 arXiv: [1312.1535 \[hep-ph\]](https://arxiv.org/abs/1312.1535).
- 2103 [36] V.A. Acciari et al. “Combined searches for dark matter in dwarf spheroidal galaxies observed  
2104 with the MAGIC telescopes, including new data from Coma Berenices and Draco”. In: *Physics of the Dark Universe* (2021), p. 100912. issn: 2212-6864. doi: <https://doi.org/10.1016/j.dark.2021.100912>. URL: <https://www.sciencedirect.com/science/article/pii/S2212686421001370>.
- 2108 [37] M. L. Ahnen et al. “Indirect dark matter searches in the dwarf satellite galaxy Ursa Major II  
2109 with the MAGIC Telescopes”. In: *JCAP* 1803.03 (2018), p. 009. doi: [10.1088/1475-7516/2018/03/009](https://doi.org/10.1088/1475-7516/2018/03/009). arXiv: [1712.03095 \[astro-ph.HE\]](https://arxiv.org/abs/1712.03095).
- 2111 [38] S. et al. Archambault. “Dark matter constraints from a joint analysis of dwarf Spheroidal  
2112 galaxy observations with VERITAS”. in: *prd* 95.8 (Apr. 2017). doi: [10.1103/PhysRevD.95.082001](https://doi.org/10.1103/PhysRevD.95.082001). arXiv: [1703.04937 \[astro-ph.HE\]](https://arxiv.org/abs/1703.04937).
- 2114 [39] Louise Oakes et al. “Combined Dark Matter searches towards dwarf spheroidal galaxies with  
2115 Fermi-LAT, HAWC, HESS, MAGIC and VERITAS”. in: *Proceedings of Science*. 2019.
- 2116 [40] Celine Armand et al. on behalf of the Fermi-LAT, HAWC, HESS, MAGIC, VERITAS.  
2117 “Combined Dark Matter searches towards dwarf spheroidal galaxies with Fermi-LAT,  
2118 HAWC, HESS, MAGIC and VERITAS”. in: *Proceedings of Science*. 2021.
- 2119 [41] Daniel Kerszberg et al. on behalf of the Fermi-LAT, HAWC, HESS, MAGIC, and VER-  
2120 TIAS collaborations. “Search for dark matter annihilation with a combined analysis of  
2121 dwarf spheroidal galaxies from Fermi-LAT, HAWC, H.E.S.S., MAGIC and VERITAS”. in:  
2122 *Proceedings of Science*. 2023.
- 2123 [42] A. U. Abeysekara et al. “Observation of the Crab Nebula with the HAWC Gamma-Ray  
2124 Observatory”. In: *The Astrophysical Journal* 843.1 (June 2017), p. 39. doi: [10.3847/1538-4357/aa7555](https://doi.org/10.3847/1538-4357/aa7555). URL: <https://doi.org/10.3847/1538-4357/aa7555>.
- 2126 [43] Giacomo Vianello et al. *The Multi-Mission Maximum Likelihood framework (3ML)*. 2015.  
2127 arXiv: [1507.08343 \[astro-ph.HE\]](https://arxiv.org/abs/1507.08343).
- 2128 [44] Marco Cirelli et al. “PPPC 4 DM ID: a poor particle physicist cookbook for dark matter  
2129 indirect detection”. In: *Journal of Cosmology and Astroparticle Physics* 2011.03 (Mar.  
2130 2011). issn: 1475-7516. doi: [10.1088/1475-7516/2011/03/051](https://doi.org/10.1088/1475-7516/2011/03/051). URL: <http://dx.doi.org/10.1088/1475-7516/2011/03/051>.

- 2132 [45] Alex Geringer-Sameth, Savvas M. Koushiappas, and Matthew Walker. “DWARF GALAXY  
 2133 ANNIHILATION AND DECAY EMISSION PROFILES FOR DARK MATTER EXPERI-  
 2134 MENTS”. in: *The Astrophysical Journal* 801.2 (Mar. 2015), p. 74. ISSN: 1538-4357. doi:  
 2135 [10.1088/0004-637X/801/2/74](https://doi.org/10.1088/0004-637X/801/2/74). URL: <http://dx.doi.org/10.1088/0004-637X/801/2/74>.
- 2137 [46] A. Albert et al. “Dark Matter Limits from Dwarf Spheroidal Galaxies with the HAWC  
 2138 Gamma-Ray Observatory”. In: *The Astrophysical Journal* 853.2 (Feb. 2018), p. 154. ISSN:  
 2139 1538-4357. doi: [10.3847/1538-4357/aaa6d8](https://doi.org/10.3847/1538-4357/aaa6d8). URL: <http://dx.doi.org/10.3847/1538-4357/aaa6d8>.
- 2141 [47] V. Bonnivard et al. “Spherical Jeans analysis for dark matter indirect detection in dwarf  
 2142 spheroidal galaxies - Impact of physical parameters and triaxiality”. In: *Mon. Not. Roy.  
 2143 Astron. Soc.* 446 (2015), pp. 3002–3021. doi: [10.1093/mnras/stu2296](https://doi.org/10.1093/mnras/stu2296). arXiv:  
 2144 [1407.7822 \[astro-ph.HE\]](https://arxiv.org/abs/1407.7822).
- 2145 [48] M. Ackermann et al. “Searching for Dark Matter Annihilation from Milky Way Dwarf  
 2146 Spheroidal Galaxies with Six Years of Fermi Large Area Telescope Data”. In: *prl* 115.23,  
 2147 231301 (Dec. 2015), p. 231301. doi: [10.1103/PhysRevLett.115.231301](https://doi.org/10.1103/PhysRevLett.115.231301). arXiv:  
 2148 [1503.02641 \[astro-ph.HE\]](https://arxiv.org/abs/1503.02641).
- 2149 [49] M. L. Ahnen et al. “Limits to Dark Matter Annihilation Cross-Section from a Combined  
 2150 Analysis of MAGIC and Fermi-LAT Observations of Dwarf Satellite Galaxies”. In: *JCAP*  
 2151 1602.02 (2016), p. 039. doi: [10.1088/1475-7516/2016/02/039](https://doi.org/10.1088/1475-7516/2016/02/039). arXiv: [1601.06590](https://arxiv.org/abs/1601.06590)  
 2152 [astro-ph.HE].
- 2153 [50] Javier Rico et al. *gLike: numerical maximization of heterogeneous joint  
 2154 likelihood functions of a common free parameter plus nuisance parameters*.  
<https://doi.org/10.5281/zenodo.4601451>. Version v00.09.03. Mar. 2021. doi: [10.5281/zenodo.4601451](https://doi.org/10.5281/zenodo.4601451). URL: <https://doi.org/10.5281/zenodo.4601451>.
- 2157 [51] Tjark Miener and Daniel Nieto. *LklCom: Combining likelihoods from different experiments*.  
<https://doi.org/10.5281/zenodo.4597500>. Version v0.5.3. Mar. 2021. doi: [10.5281/zenodo.4597500](https://doi.org/10.5281/zenodo.4597500). URL: <https://doi.org/10.5281/zenodo.4597500>.
- 2160 [52] T. Miener et al. “Open-source Analysis Tools for Multi-instrument Dark Matter Searches”.  
 2161 In: *arXiv e-prints*, arXiv:2112.01818 (Dec. 2021), arXiv:2112.01818. arXiv: [2112.01818](https://arxiv.org/abs/2112.01818)  
 2162 [astro-ph.IM].
- 2163 [53] Alex Geringer-Sameth and Matthew Koushiappas Savvas M. and Walker. “Dwarf galaxy  
 2164 annihilation and decay emission profiles for dark matter experiments”. In: *Astrophys.  
 2165 J.* 801.2 (2015), p. 74. doi: [10.1088/0004-637X/801/2/74](https://doi.org/10.1088/0004-637X/801/2/74). arXiv: [1408.0002](https://arxiv.org/abs/1408.0002)  
 2166 [astro-ph.CO].
- 2167 [54] Gianfranco Bertone, Dan Hooper, and Joseph Silk. “Particle dark matter: evidence, can-

- 2168 didates and constraints”. In: *Physics Reports* 405.5-6 (Jan. 2005), pp. 279–390. ISSN:  
2169 0370-1573. doi: [10.1016/j.physrep.2004.08.031](https://doi.org/10.1016/j.physrep.2004.08.031). URL: <http://dx.doi.org/10.1016/j.physrep.2004.08.031>.
- 2170  
2171 [55] V. Bonnivard et al. “Dark matter annihilation and decay in dwarf spheroidal galaxies: The  
2172 classical and ultrafaint dSphs”. In: *Mon. Not. Roy. Astron. Soc.* 453.1 (2015), pp. 849–867.  
2173 doi: [10.1093/mnras/stv1601](https://doi.org/10.1093/mnras/stv1601). arXiv: [1504.02048 \[astro-ph.HE\]](https://arxiv.org/abs/1504.02048).
- 2174 [56] A. et al. Albert. “Searching for Dark Matter Annihilation in Recently Discovered Milky Way  
2175 Satellites with Fermi-LAT”. in: *Astrophys. J.* 834.2 (2017), p. 110. doi: [10.3847/1538-4357/834/2/110](https://doi.org/10.3847/1538-4357/834/2/110). arXiv: [1611.03184 \[astro-ph.HE\]](https://arxiv.org/abs/1611.03184).
- 2176  
2177 [57] Mattia Di Mauro and Martin Wolfgang Winkler. “Multimessenger constraints on the dark  
2178 matter interpretation of the Fermi-LAT Galactic Center excess”. In: *prd* 103.12, 123005  
2179 (June 2021), p. 123005. doi: [10.1103/PhysRevD.103.123005](https://doi.org/10.1103/PhysRevD.103.123005). arXiv: [2101.11027 \[astro-ph.HE\]](https://arxiv.org/abs/2101.11027).
- 2180  
2181 [58] HongSheng Zhao. “Analytical models for galactic nuclei”. In: *Mon. Not. Roy. Astron. Soc.*  
2182 278 (1996), pp. 488–496. doi: [10.1093/mnras/278.2.488](https://doi.org/10.1093/mnras/278.2.488). arXiv: [astro-ph/9509122 \[astro-ph\]](https://arxiv.org/abs/astro-ph/9509122).
- 2183  
2184 [59] H. C. Plummer. “On the Problem of Distribution in Globular Star Clusters: (Plate 8.)”  
2185 In: *Monthly Notices of the Royal Astronomical Society* 71.5 (Mar. 1911), pp. 460–470.  
2186 ISSN: 0035-8711. doi: [10.1093/mnras/71.5.460](https://doi.org/10.1093/mnras/71.5.460). eprint: <https://academic.oup.com/mnras/article-pdf/71/5/460/2937497/mnras71-0460.pdf>. URL:  
2187 <https://doi.org/10.1093/mnras/71.5.460>.
- 2188  
2189 [60] Daniel R. Hunter. “Derivation of the anisotropy profile, constraints on the local velocity  
2190 dispersion, and implications for direct detection”. In: *JCAP* 02 (2014), p. 023. doi:  
2191 [10.1088/1475-7516/2014/02/023](https://doi.org/10.1088/1475-7516/2014/02/023). arXiv: [1311.0256 \[astro-ph.CO\]](https://arxiv.org/abs/1311.0256).
- 2192  
2193 [61] Barun Kumar Dhar and Liliya L. R. Williams. “Surface mass density of the Einasto family  
2194 of dark matter haloes: are they Sersic-like?” In: *Mon. Not. Roy. Astron. Soc.* (2010). doi:  
[10.1111/j.1365-2966.2010.16446.x](https://doi.org/10.1111/j.1365-2966.2010.16446.x).
- 2195  
2196 [62] M. Baes and E. Van Hese. “Dynamical models with a general anisotropy profile”. In:  
2197 *Astron. Astrophys.* 471 (2007), p. 419. doi: [10.1051/0004-6361:20077672](https://doi.org/10.1051/0004-6361:20077672). arXiv:  
[0705.4109 \[astro-ph\]](https://arxiv.org/abs/0705.4109).
- 2198  
2199 [63] Matthew G. Walker, Edward W. Olszewski, and Mario Mateo. “Bayesian analysis of re-  
2200 solved stellar spectra: application to MMT/Hectochelle observations of the Draco dwarf  
2201 spheroidal”. In: *mnras* 448.3 (Apr. 2015), pp. 2717–2732. doi: [10.1093/mnras/stv099](https://doi.org/10.1093/mnras/stv099).  
arXiv: [1503.02589 \[astro-ph.GA\]](https://arxiv.org/abs/1503.02589).
- 2202 [64] Nicholas L. Rodd et al. “Dark matter spectra from the electroweak to the Planck scale”. In:

- 2203        *J. High Energy Physics* 121.10.1007 (June 2021).
- 2204 [65] Pace, Andrew B and Strigari, Louis E. “Scaling relations for dark matter annihilation and  
2205 decay profiles in dwarf spheroidal galaxies”. In: *Monthly Notices of the Royal Astronomical  
2206 Society* 482.3 (Oct. 2018), pp. 3480–3496. ISSN: 0035-8711. doi: [10.1093/mnras/sty2839](https://doi.org/10.1093/mnras/sty2839).
- 2208 [66] Albert, A. et al. “Search for gamma-ray spectral lines from dark matter annihilation in  
2209 dwarf galaxies with the High-Altitude Water Cherenkov observatory”. In: *Phys. Rev. D* 101 (10 May 2020), p. 103001. doi: [10.1103/PhysRevD.101.103001](https://doi.org/10.1103/PhysRevD.101.103001). URL:  
2211 <https://link.aps.org/doi/10.1103/PhysRevD.101.103001>.
- 2212 [67] Victor Eijkhout and Edmund Show and Robert van de Geijn. *The Science of Computing.  
2213 The Art of High Performance Computing*. Vol. 3. Open Copy published under CC-BY 4.0  
2214 license, 2023, pp. 63–66.
- 2215 [68] Qinrui Liu and Jeffrey Lazar and Carlos A. Argüelles and Ali Kheirandish. “ $\chi$ aro: a tool  
2216 for neutrino flux generation from WIMPs”. In: *Journal of Cosmology and Astroparticle  
2217 Physics* 2020.10 (Oct. 2020), p. 043. doi: [10.1088/1475-7516/2020/10/043](https://doi.org/10.1088/1475-7516/2020/10/043). URL:  
2218 <https://dx.doi.org/10.1088/1475-7516/2020/10/043>.
- 2219 [69] Aartsen, M. et al. “IceCube search for dark matter annihilation in nearby galaxies and galaxy  
2220 clusters”. In: *Phys. Rev. D* 88 (12 Dec. 2013), p. 122001. doi: [10.1103/PhysRevD.88.122001](https://doi.org/10.1103/PhysRevD.88.122001). URL: <https://link.aps.org/doi/10.1103/PhysRevD.88.122001>.